Head-Disk System Characterization with Head Itself as Transducer

ZHOU YIPIN

NATIONAL UNIVERSITY OF SINGAPORE

2006

Head-Disk System Characterization with Head Itself as Transducer

ZHOU YIPIN

A THESIS SUBMITTED

FOR THE DEGREE OF MASTER OF ENGINEERING

DEPARTMENT OF ELECTRICAL AND COMPUTER ENGINEERING

NATIONAL UNIVERSITY OF SINGAPORE

2006

Acknowledgments

There are many people who have made the completion of this dissertation and my graduate studies possible. Firstly, I would like to express my most sincere appreciation to all those who have helped me through this Master thesis. Many thank to my supervisor Dr. Liu Bo for his offering me the opportunity to do research work in magnetic recording, such an interesting and diverse field. His broad knowledge and enthusiasm in this field inspires me in the research work; his keen observation and strict research attitude contributed a great deal to the research work. I feel very fortunate to have him as a research advisor. I also wish to thank my supervisor, Prof. Li Lewei, for his kind support on my research course and allowing me to work under him for the past two years.

I thank all the members of my research group and the faculty and students at Data Storage Institute, Spinstronics, Media and Interface Division for useful technical discussions over the years. Special thanks to Mr. Li Hui, Dr. Yuan Zhimin, Dr. Wan Lei, Ms Zhang Wei, Mr. Ng Ka Wei, Dr. Zhang Mingsheng, Mr. Xian Rui, Miss Xiao Peiying and Miss Zhu Jin for their warm assistance.

At last, I would like to thank my parents and family for their love, encouragement, support and for their always being there to listen to me and offer advises. Without their understanding, I would not have completed this Master thesis. Also thank people who love me and people I love, thanks for those happy time in National University of Singapore.

Table of Contents

ACKNOWLEDGMENTS ..... **I**

TABLE OF CONTENTS ..... **II**

SUMMARY ..... **V**

NOMENCLATURE ..... **VII**

LIST OF FIGURES ..... **IX**

LIST OF TABLES ..... **XII**

CHAPTER 1 ..... **1**

INTRODUCTION **1**

1.1 Magnetic Recording and Magnetic Hard Disk Drive **1**
1.1.1 Magnetic Hard Disk Drives 1
1.1.2 Evolution of Magnetic Hard Disk Drive 2
1.1.3 Technology Trends and Challenges 3
1.2 Magnetic Head Disk Integration **5**
1.2.1 Magnetic Reading Head 5
1.2.2 Magnetic Writing Head 7
1.2.3 Magnetic Integration of Head-Disk Systems 7
1.3 Problem Statement and Motivations **9**
1.3.1 Head-Disk System Characterization 9
1.3.2 Simulation Platform Development for Head-Disk System 10
1.3.3 Evaluation of Harmonic Based Fly-Height Measurement Method 11
1.3.4 Gap Length Variation Estimation Method 12
1.3.5 High Density Recording and High Data Rate Recording 12
1.4 Contributions and Organization of the Thesis **14**

CHAPTER 2 ..... **16**

FLY-HEIGHT MEASUREMENT **16**

2.1 Optical Fly-Height Testing Methods **17**
2.1.1 Three-Wavelength Intensity Interferometry Technique 18
2.1.2 Limitations of the State-of-the-Art Optical Fly-Height Test Method 20
2.2 In-Situ Fly-Height Testing Methods **22**
2.2.1 Reading Process Based Methods 23
2.2.1.1 PW50 Method 23
2.2.1.2 Harmonic Method 25
2.2.1.3 Triple Harmonic Method 27
2.2.2 Writing Process Based Methods 29
2.2.2.1 Carrier Erasure Current Method 29
2.2.2.2 Scanning Carrier Current Method 31
2.2.3 Capacitance Method 32
2.3 Summary **34**

CHAPTER 3 SIMULATION PLATFORM DEVELOPMENT **35**

3.1 Platform Development **35**
3.1.1 Motivation and Functions Developed 35
3.1.2 User Interface 37
3.2 Transition Modeling and Playback Signal Modeling **39**
3.2.1 Medium Transition Model of the Write Process 39
3.2.2 Reading Process Modeling and MR Head Reciprocity 41

3.2.2.1 Reciprocity Algorithm 41
3.2.2.2 Surface Potential Model Comparison 44
3.2.3 Playback Pulses 49
3.3 Playback with Multiple Transitions 52
3.4 Spectral Analysis 56
3.4.1 Isolated Pulse Frequency Response 56
3.4.2 Harmonic Ratio Methods and Spectrum Comparison 58
3.4.2.1 Square Wave Recording 59
3.4.2.2 Triple Harmonic Pattern Recording 61
3.4.2.3 Energy Distribution of Harmonics 63
3.5 Summary 65

CHAPTER 4 IN-DEPTH ANALYSIS OF HARMONIC RATIO BASED FLY-HEIGHT MEASUREMENT METHODS 66

4.1 Measurement Sensitivity 66
4.2 Measurement Precision 68
4.2.1 Repeatability Function 69
4.2.2 Effect of Variation of System Parameters on Fly-Height Measurement 69
4.2.2.1 Media Thickness Effect 70
4.2.2.2 Gap Length Effect 72
4.2.3 Effect of Noise on Fly-Height Measurement 73
4.2.3.1 Peak Detection and Testing Accuracy 75
4.2.3.2 Envelope Detection and Testing Accuracy 77
4.3 Experiment Investigations 78
4.3.1 Experiments 78
4.3.2 Heads and Media Characterization 81
4.3.3 Comparison of Theoretical and Experiment Waveforms 84
4.3.4 Testing Repeatability 86
4.3.4.1 Triple Harmonic Method 86
4.3.4.2 Square Wave Method 90
4.4 Summary 92

CHAPTER 5 HARMONIC ANALYSIS METHOD, GAP LENGTH EFFECT AND ESTIMATION OF GAP LENGTH DEVIATION 93

5.1 Gap Length Effect on Fly-Height Measurement 93
5.1.1 Experiment Design 93
5.1.2 Experimental Conditions and Nominal Head-Media Parameters 94
5.1.3 Experimental Results and Discussion 95
5.1.4 Further Experimental Analysis and Phenomenon Confirmation 98
5.1.5 Root Cause Identification 101
5.1.6 Further Discussion on Gap Length Effect at Different Sensitivity Variation with Density 103
5.2 Gap Length Variation Estimation 107
5.2.1 Motivation for Exploring New Methodology 108
5.2.2 Theory of the Methodology 109
5.2.2.1 G Function and Gap Length Difference between Reference Head and Sample Head 110
5.2.2.2 Gap Length Variation Function and Gap Length Estimation 113
5.2.3 Experiment Results 115
5.3 Summary 119

CHAPTER 6 HIGH DENSITY RECORDING AND NONLINEARITY EFFECT 120

6.1. Performance Analysis at High Recording Density 120
6.2 Nonlinearity at High Bit Density and Its Effects on Accuracy of In-Situ Flying Height Analysis 124
6.2.1 Nonlinearity at High Linear Density Recording 124
6.2.2 Interactions between NLTS and HTS 125

6.2.2.1 Transition Shift over AC Erased Track 125
6.2.2.2 Transition Shift over DC Erased Track 126
6.2.3 Effect on Triple Harmonic Pattern 128
6.2.3.1 Transition Shift and All "1" Pattern 128
6.2.3.2 Transition Shift and Triple Harmonic Pattern 128
6.2.4 Enforced Nonlinearity Effect at High Data Rate Recording 129
6.3 Fly-Height Testing in High Linear Density and High Data Rate Recording 132
6.4 Summary 136

CHAPTER 7 138

NONLINEARITY IN TRACK DIRECTION AND ITS EFFECTS ON FLY-HEIGHT ANALYSIS 138

7.1 Experiments in Track Direction 138
7.1.1 Cross-track Profile 138
7.1.2 Track-edge Effect at High Density 141
7.2 Theory and Simulation 143
7.2.1 Recording Physics Underlying the Phenomena 143
7.2.2 Simulation Model 145
7.3 Summary 148

CHAPTER 8 149

SUMMARY AND FUTURE WORK 149

REFERENCES 152

Summary

Areal density, or storage capacity, is the most critical parameters for a magnetic hard disk drive (HDD). In order to achieve high density data recording, all parameters in the head-disk systems of a magnetic disk drives have been scaled downwards progressively to write/read smaller and smaller data bits. Therefore, how to accurately and reliably characterize the critical parameters of head disk systems becomes challenging and crucial for sustaining the growth of areal density of HDD.

Low fly-height head-disk interface technology, high sensitivity head technology and small grain size media technology are 3 technologies determining the achievable area density of a magnetic hard disk drive. To further increase the recording density, we have to further reduce the fly-height (FH), which is the spacing between slider and recording disk. Currently technology allows for 8-10 nm fly-height in high-end commercial disk drives. The intermolecular force effect, slider-lube and slider-lube-disk interactions become the main concerns of head disk interface at such a small spacing. However, the current industry standard fly-height measurement technology, namely, the optical fly-height testing technology, can not be used to evaluate the instability caused by such interaction, and in-situ characterization is the only acceptable solution. Among various in-situ techniques, the technology that uses head itself as transducer for the fly-height characterization is believed to be the best choice, as it can well reflect the actual scenario in the disk drives and head-disk interface.

This dissertation focuses on characterization technology with data reading head as transducer. A simulation platform is developed for modeling and simulation of the magnetic interaction and inter-dependence of magnetic head and magnetic disk-media

-- the magnetic head-disk systems. The platform provides the flexibility of theoretical model selection and parameters setup. It provides the convenience for the analysis of the effects of read / writes parameters on the overall performance of readback signal. The platform proved to be a powerful tool for the exploration and confirmation of characterization methods

Thorough experimental and theoretical evaluations of harmonic ratio based fly-height measurement methods are done based on testing sensitivity and accuracy. Sensitivity function, error model and repeatability function are proposed in this thesis. Furthermore, the methods and parameter selections to achieve high testing sensitivity and accuracy are proposed and experimentally confirmed.

Gap length is the most important geometric parameter of the reading head. It defines the resolution of the reading head. A novel method is proposed for the quantitative evaluation of the gap length variation among a batch of magnetoresistive/giant magnetoresistive (MR/GMR) heads with same structure and similar design. According to literature review, no one has reported a method for the evaluation of gap length difference among heads of same nominal gap length value yet. Experimental work confirms that the proposed method is easy for implementation and the results suggest that variation of gap length is considerable and may have obvious effect on recording performance in high density recording systems.

Nonlinearity is another challenge when technology moves to high density. This thesis, for the first time, reports the experimental investigation and theoretical explanation of the possible in-situ testing error caused by nonlinearity effects at high recording density.

Nomenclature

Unless otherwise stated, the following abbreviations and symbols are used throughout this dissertation.

ABS	Air Bearing Surface
AGC	Automatic Gain Controller
DFHT	Dynamic Fly Height Tester
DLC	Diamond Like Carbon
FFT	Fast Fourier Transform
FH	Fly Height
FIR	Finite Impulse Response
GMR	Giant Magnetoresistive
GPIB	General Purpose Interface Bus (IEEE 488)
HAMR	Heat Assisted Magnetic Recording
HDD	Hard Disk Drive
HF	High Frequency
HMS	Head Medium Spacing
HRF	Harmonic Ratio Fly-Height
HTS	Hard Transition Shift
IF	Intermediate Frequency
IIR	Infinite Impulse Response
LF	Low Frequency
MCU	Micro Controller Unit
MFM	Magnetic Force Microscope

MR	Magnetoresistive
NLTS	Nonlinear Transition Shift
PLL	Phase-Locked Loop
PRML	Partial Response Maximum Likelihood
RPM	Revolution Per Minute
RWA	Read/Write Analyzer
SNR	Signal-to-Noise Ratio
SUL	Soft Under Layer
TAA	Track Average Amplitude
THM	Triple Harmonic Method
UP	Universal Preamplifier
WITE	Windows™ Integrated Test Environment (Guzik Enterprise)

List of Figures

Chapter 1

Fig. 1.1 Hard disk drive structures....2
Fig. 1.2 Scaling law of parameters with the increase in areal density....4
Fig. 1.3 Merged read/write head flying over the medium: (a) perpendicular, (b) longitudinal....6
Fig. 1.4 Illustration of fly-height and magnetic spacing....8

Chapter 2

Fig. 2.1 Schematic of three-wavelength fly-height tester....18
Fig. 2.2 Multi- reflections and transmissions for two interfaces....19
Fig. 2.3 Sensitivity of the optical fly-height test method....21
Fig. 2.4 The formation of the “111100” code pattern....28

Chapter 3

Fig. 3.1 User interface of simulation platform....37
Fig. 3.2 Data flow diagram....38
Fig. 3.3 Transition shapes of mostly used functions and micro magnetic model....40
Fig. 3.4 Geometrical configuration of modeling of reading process....44
Fig. 3.5 Surface potential $\Phi_s(x)$ with different approaches....45
Fig. 3.6 (a) Surface head field with *t/g*=1/10 (b) Surface head field with *t/g*=1/5 45
Fig. 3.7 Comparison between Potter and Fourier surface field spectra....48
Fig. 3.8 Voltage pulse with different transition models, showing that tanh and error function models give similar amplitude....50
Fig. 3.9 Voltage pulse with different surface potential models....50
Fig. 3.10 Voltage Pulse with different magnetic spacing d....51
Fig. 3.11 Square wave recording playback signal with B=400nm....53
Fig. 3.12 Square wave recording playback signal with B=120nm....53
Fig. 3.13 Roll off curves of different magnetic spacing....54
Fig. 3.14 Roll off curves of different gap length....55
Fig. 3.15 111100-code playback signals....56
Fig. 3.16 Square wave spectrum of the fundamental component....60
Fig. 3.17 Square Wave voltage spectrums....61
Fig. 3.18 spectrum of readback signal of “111100” pattern....63
Fig. 3.19 Normalized Harmonic Power of the conventional square wave recording....64
Fig. 3.20 Power Spectrum of the triple harmonic method....64

Chapter 4

Fig. 4.1 Harmonic intensity at different channel density....67
Fig. 4.2 Media thickness effect on fly-height measurement....71
Fig. 4.3 Gap length variation effect on fly-height measurement....73
Fig. 4.4 Harmonic Power and fly-height error caused by transition noise and channel noise....76

Fig. 4.5 Fly-height error caused by transition noise and channel noise....76
Fig. 4.6 Block diagram of the programmable filters for the in-situ fly-height test....77
Fig. 4.7 Block diagram of the experimental configuration....79
Fig. 4.8 Experimental setup for harmonic based in-situ fly-height and gap width measurement....81
Fig. 4.9 ABS design (a) 2-D image and (b) 3-D image of the slider used in the experiment....82
Fig. 4.10 Track average voltages; overwrite ratio and PW50 as a function of write current....83
Fig. 4.11 MR saturation curves....84
Fig. 4.12 Roll-off curve....84
Fig. 4.13 (a) Experiment waveform at density 1.32 (b) Simulation waveform at density1.32....85
Fig. 4.14 Comparison between A/B of experiment and simulation waveforms at multiple densities....86
Fig. 4.15 Maximum fly-height variation (nm) with different harmonic ratios and densities....88
Fig. 4.16 Average fly-height variation (nm) with different harmonic ratios and densities....89
Fig. 4.17 Simulated fly-height variation with different harmonic ratios and densities 90
Fig. 4.18 Average and maximum fly-height variation (nm) of all one pattern at different densities....91
Fig. 4.19 Simulated fly-height variation of all one pattern at different density....92

Chapter 5

Fig. 5.1 Fly-height variation ΔFH of 130 heads calculated at different testing densities 97
Fig. 5.2 $\Delta(FH + \ln C)$ of 43 heads calculated at different densities....99
Fig. 5.3 $\Delta(FH + \ln C)$ (nm) variation at different channel densities of different media thickness (nominal gap length $\delta_0 = 20nm$)....102
Fig. 5.4 $\Delta FH + \ln C$ (nm) variation at different channel densities and different gap lengths (nominal gap length $g_0 = 36nm$)....103
Fig. 5.5 (a) $\Delta \ln C$ variation $\Delta\Delta \ln C$ of 43 heads calculated at densities 0.354 and 0.708 104
Fig. 5.6 (a) $\Delta \ln C$ variation $\Delta\Delta \ln C$ of 43 heads calculated at densities 0.354 and 0.566 106
Fig. 5.7 (a) Structure and (b) geometrical scheme for the evaluation of gap length variation of typical spin valve reading head....108
Fig. 5.8 Dependence of the function G on channel density and gap length variation 112
Fig. 5.9 Dependence of the function G on gap length variation at three densities....112
Fig. 5.10 *GL* function and its dependence on channel density....113
Fig. 5.11 Experimental gap length variation function for Densities 0.708 and 1.415 116
Fig. 5.12 Estimated gap length for densities 0.708 and 1.415....117
Fig. 5.13 Experimental gap length variation function for Densities 0.566 and 1.415 117
Fig. 5.14 Estimated gap length for densities 0.566 and 1.415....117
Fig. 5.15 Comparison of cumulative curves of estimated gap length at different density combinations (densityies 0.566 and 1.415, densities 0.708 and 1.415)....119

Chapter 6

Fig. 6.1 Frequency response of the readback channel 121
Fig. 6.2 Effective magnetic spacing change (nm) without compensation of channel response 123
Fig. 6.3 Effective spacing change (nm) with compensation of channel response 123
Fig. 6.4 Measured transition shift for MR head with different initial medium magnetization 127
Fig. 6.5 Waveform with different erasing methods and linear superposition 129
Fig. 6.6 NLTS as a function of linear recording density at various medium velocities 130
Fig. 6.7 Harmonic Power (dB) of V_3 and V_1 tested at 6000 RPM with different erasing methods 134
Fig. 6.8 Harmonic ratios with different DC erase methods at 8000RPM 134
Fig. 6.9 Harmonic ratios with different DC erase methods at 6000RPM 135
Fig. 6.10 Differences in the harmonic ratio between the two erase methods at two disk speeds 136

Chapter 7

Fig. 7.1 ABS design (a) optical microscope image and (b) ZYGO microscope image 139
Fig. 7.2 Harmonic ratio cross-track profile and the signal amplitude cross-track profile. 140
Fig. 7.3 Cross-track profile of the different harmonic densities 140
Fig. 7.4 Waveforms of triple harmonic method at 90Mhz (left) and 120Mhz (right) 141
Fig. 7.5 Change in effective magnetic spacing(nm) compared to track center as a function of cross-track position 142
Fig. 7.6 Isolated pulse waveforms at track center and off-track positions 143
Fig. 7.7 Constant write field magnitude contours and in-plane vector field 144
Fig. 7.8 MFM measurements of transitions and transition contour curve 144
Fig. 7.9. Magnetization simulated with micro-magnetic model 146
Fig. 7.10. Assumed transition contour and transition parameter variation in the 148

List of Tables

Chapter 3

Table 3.1 Transition models used in the modeling platform.....40

Chapter 4

Table 4.1 Effect of media thickness variation on fly-height measurement.....72
Table 4.2 Head, media, and testing system parameters 85
Table 4.3 Transition Parameter for Fitting.....86
Table 4.4 Fly-height variation calculated with V_{21} of triple harmonic method.....87
Table 4.5 Fly-height variation calculated with V_{31} of triple harmonic method.....88
Table 4.6 Fly-height variation calculated with V_{32} of triple harmonic method.....88
Table 4.7 Fly-height variation calculated with V_{31} of all one pattern at different densities 91

Chapter 5

Table 5.1 The value and rank of $FH + \ln C$ of 43 heads at different densities.....101
Table 5.2 Theoretical gap length variation function for densities 0.708 and 1.415....116
Table 5.3 Theoretical gap length variation function for densities 0.566 and 1.415....118

Chapter 6

Table 6.1 The writing frequency (MHz) at different RPM for certain linear density.122
Table 6.2 Illustration of nonlinearity effect on pattern 111100 with different erasing methods.....129

Chapter 1

Introduction

Information technology plays an important role in our daily life. Information technology includes information sensing technology, information transferring technology (communication and network), and information storage technology. Magnetic data storage technology continues to be the primary storage technology in modern society.

The success of HDDs originates from an ever-increasing storage areal density, high data rate and fast access time coupled with a consistent reduction in price per megabyte enabled by continuous technological advances in recording physics, new materials, mechanics, tribology, signal processing, and so on.

This thesis summarizes author's efforts in investigating new testing methodologies and their engineering solutions for high density magnetic data recording.

1.1 Magnetic Recording and Magnetic Hard Disk Drive

1.1.1 Magnetic Hard Disk Drives

A magnetic HDD consists of a disk pack, a set of read/write heads, sliders and suspensions, actuation mechanisms and electronics as shown in Fig. 1.1. The information is written onto co-rotating disks by a read/write head that is carried by a

slider located at the end of a suspension which is mounted on a rotary actuator. These slider-suspension systems are stacked in an assembly called head stack. The combination of the spinning disks and the rotary voice coil motor allows the read/write transducers to rapidly scan the entire disk surface. The air pressure generated by the spinning disk makes slider fly. The head is held off the disk surface by an air cushion, or air bearing. The characteristics of the air bearing have a direct relationship with the aerodynamic design of the slider. As the head is "floated" over the surface of high speed moving disk, the concept of "fly-height" is introduced which refers to the mechanical spacing between the read/write head and the disk surface.

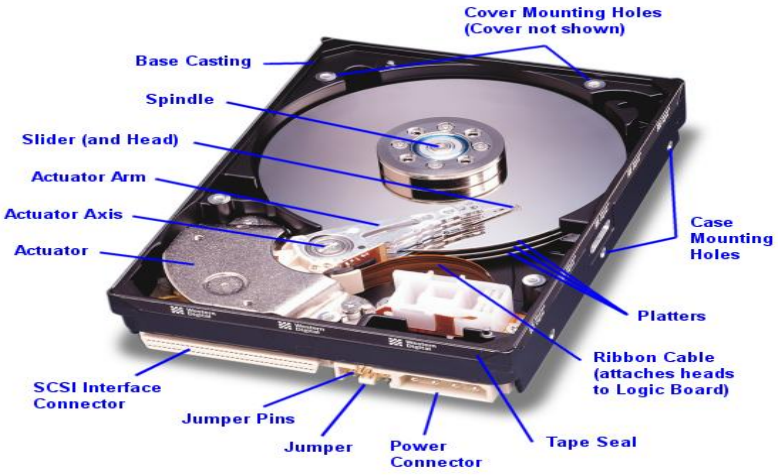

Fig. 1.1 Hard disk drive structures

1.1.2 Evolution of Magnetic Hard Disk Drive

To meet the tremendous demand of data storage, the recording density of the HDDs has to be increased continuously. Areal density of HDDs, measured in data bits per square inch, is the primary indicator of technological progress in the HDD industry. Areal density is the product of the number of tracks per inch (the track density) and the number of bit per inch (the bit density). From the first hard disk drive introduced by IBM in 1956 with an areal density of 2 kilo-bit (kb)/in^2 and a storage capability of 5

mega-byte (MB) which had 50 disks and each disk being 24 inches in diameter of, to the modern disk drives of areal density of more than 100 Gb/in^2 and in various disk diameters (called form-factor) from 5.25 inch to 1 inch, the areal density of HDDs has been increasing tremendously in the last three decades. With the introduction of magnetoresistive (MR) head, giant magnetoresistive (GMR) head and granular media technology, the annual growth rate reaches to an amazing rate of 100% per year in the recent past years (2001-2004). The magnetic properties, such as signal to noise ratio (SNR), media coercivity and head structure, are also improved to keep in pace with the increase of areal density.

The next goal of magnetic data storage technology is to increase the areal density to 1 TB/in^2 in 3~5 years [1].

1.1.3 Technology Trends and Challenges

The general trend of magnetic recording and HDD technology is to further increase areal density, further reduce the cost of each mega-byte of information stored in HDD and retain high reliability. To achieve these objectives, all the parameters of the magnetic recording system must be scaled downwards progressively. This is called the scaling law. Fig. 1.2 illustrates the scaling down of head disk interface parameters with increase in areal density.

Bit area, which is defined as the product of bit length and track pitch, needs to be reduced in order to store more magnetic transitions in a unit area of disk surface. Reading and writing heads are made in smaller size and the slider is designed to fly

closer to disk to maintain high read/write resolution while sensing a weaker magnetic flux from the smaller bit area. Ideally, zero spacing is preferred. However, zero spacing is impossible as it is impossible to achieve zero surface roughness on slider or disk surface. Also, contact recording would lead to higher friction and wear at the head-disk interface, hence causing reliability concerns and contact induced off-track and vibration. At the same time, media thickness is required to be scaled down to improve the read/write performance of the head-disk systems for high density data storage. The ability to accurately and reliably characterize the critical parameters of the head-disk systems, including fly-height, head parameters, and disk parameters, becomes challenging and important for sustaining the growth of areal density in HDD.

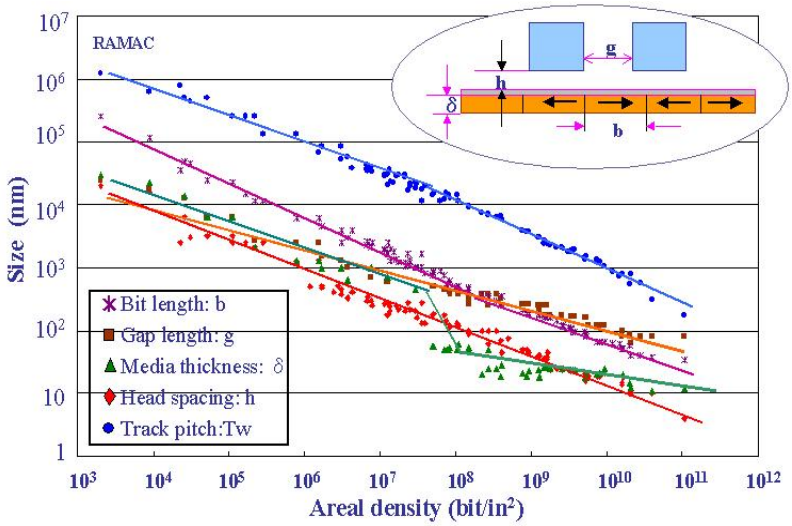

Fig. 1.2 Scaling law of parameters with the increase in areal density

High sensitivity head transducer technology, highly stable data storage media with further reduced grain size and grain size distribution, and further reduced but stable head-disk spacing or fly-height are the major challenges for future magnetic data storage industry.

As bit area decreases to some extend, the thermal energy in each data bit starts to compete with the media anisotropy energy which maintains the stability of the bit, causing magnetic instability problem. This behavior is called superparamagnetism and can limit the future extendibility of magnetic storage. Although proper selection of disk materials and structures can significantly delay the superparamagnetic effect, the conventional longitudinal magnetic recording in continuous magnetic films may not be able to push areal density beyond 200 Giga-bit (Gb)/in^2 where limits of thermal stability of magnetic bits exist. Perpendicular recording technology, with magnetization of each bit orientated perpendicular to disk surface, will be used to push recording density beyond 200 Gb/in^2. However, writing capability will become a limitation factor when areal density is further increase to a level beyond 1 Tera-bit (Tb)/in^2. It is expected that assisted writing scheme will be needed and one of the promising assisted writing scheme is so called Heat Assisted Magnetic Recording (HAMR) [1]. It is believed that pattern media, self-organized magnetic array and assisted writing technology will make 50 Tb/in^2 possible from magnetic view point.

However, it is widely believed that the engineering limitation of future high density data storage comes from head-disk interface – how to achieve stable head-disk spacing over nanometer spaced head-disk systems.

1.2 Magnetic Head Disk Integration

1.2.1 Magnetic Reading Head

Fig. 1.3 depicts a merged read/write head flying over a rotating disk where the structure on the right illustrates the case for the longitudinal recording scheme and that

on the left illustrates the perpendicular recording. The head design consists of a thin film inductive write element and a read element, which consists of a MR or GMR sensor between two magnetic shields.

The magnetic shields are made of soft, highly permeable magnetic material. Thus, the MR or GMR sensor essentially "sees" only the magnetic field from the recorded data bit to be read. In a merged read/write head structure, the second magnetic shield also functions as one pole of the inductive write head.

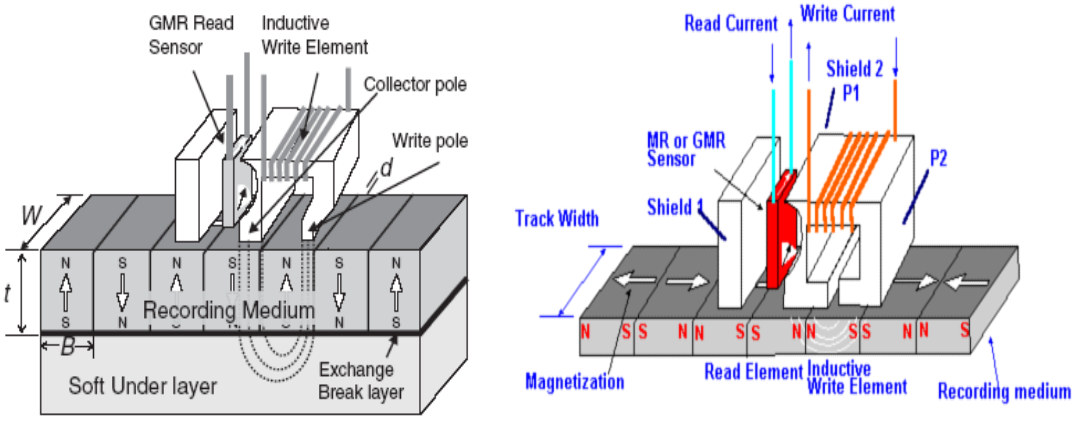

(a) (b)

Fig. 1.3 Merged read/write head flying over the medium: (a) perpendicular, (b) longitudinal

During reading, the presence of a magnetic transition or flux reversal between bits causes the magnetic orientation in the MR or GMR sensor to change and this causes the resistance of this sensor to change. The sensor's output voltage or signal is the product of this resistance change and the read bias current. The resistance change signal is amplified by low-noise electronics and sent to the HDD's data detection electronics. In general, MR devices are complex structures that incorporate many magnetic layers to achieve linearity with respect to the external field.

1.2.2 Magnetic Writing Head

The inductive write head records bits of information by magnetizing tiny regions along concentric tracks. To record information on the surface of the magnetic disk, an alternating current is passed through the coils wrapped around a specially shaped ferrous core in the write head, thus producing a fringing magnetic field in two orientations. The magnetic fringing field in turn creates two permanently magnetized states of remanent magnetization in the ferromagnetic data recording layer.

In the case of perpendicular magnetic recording scheme, the write field also creates two states of remanent magnetization in the ferromagnetic layer: permanently magnetized in either up or down direction perpendicular to the disk surface. There is a special layer in the perpendicular magnetic recording media: the soft magnetic under layer (SUL). The SUL is located under the data recording layer and it guides the magnetic flux from the write pole to the collector pole and functions as part of the write head. In simple models, it is often assumed that the SUL generates a mirror image of the write pole, therefore effectively placing the recording media in the 'gap' of the 'write head'.

1.2.3 Magnetic Integration of Head-Disk Systems

Maintaining a controlled separation between the magnetic recording head and the magnetic medium is critically important for keeping reliable operation of HDDs. Increase of areal density requires decreasing magnetic spacing between the head and disk, which involves the head flying closer to the disk, as well as using a thinner protective overcoat while maintaining a highly durable interface. The interaction

between slider, lubricant and disk surface is becoming the most crucial robustness concern in advanced data storage systems. In general, Fig. 1.4 defines magnetic spacing and fly-height, which are discussed in the thesis.

1. Fly-height: It is the distance from the air-bearing surface (ABS) to the mean disk surface.
2. Head-Media Spacing (HMS): It is defined as the spacing between top of the magnetic layer and bottom of the read/write element. It is the physical spacing between magnetic head element and magnetic data recording layer. HMS includes such factors as fly-height of the head over the disk, recession of the head pole tip, and thickness of the diamond like carbon (DLC) film on the head surface and the thickness of the carbon and lubricant overcoats on the disk surface.
3. Effective magnetic spacing: It is the effective spacing from data read/write viewpoint. For longitudinal magnetic recording, it is the spacing between head surface and half of the thickness of magnetic layer of the data recording disk.

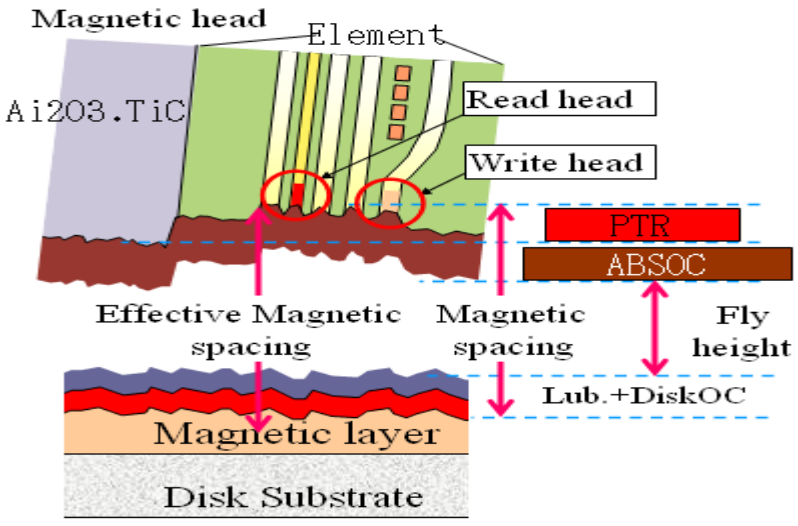

Fig. 1.4 Illustration of fly-height and magnetic spacing

Current technology allows 7-10 nm fly-height in the high-end commercial disk drives. It is estimated that the fly-height should be reduced to a value around 3.5-2.5 nm so as

to achieve areal densities around 1 Tb/in^2. Since the head-disk spacing becomes so small, intermittent contacts occur during disk drive operation. Such contacts lead to fly-height variations.

Therefore, it becomes more and more important and necessary to make high accuracy head-disk spacing measurement. Challenges arise in the effective and precise characterization of head-disk system as the various system parameters are scaled down to meet the requirements of growing areal density in disk drives.

1.3 Problem Statement and Motivations

1.3.1 Head-Disk System Characterization

All the parameters in head-disk systems have been scaled downwards progressively to write/read smaller and smaller data bits. The smaller system dimension inevitably introduces tribological and magnetic instabilities and makes the manufacturing process more difficult to maintain the high standard of reliability and performance for the head disk system. Furthermore, the ability to accurately and reliably characterize the critical parameters of head-disk systems also becomes challenging and important for sustaining the growth of areal density in HDD.

As in Fig. 1.2, head-disk spacing becomes very small. Since frequent intermittent or continuous contacts occur during normal steady state operation in disk drives, the slider-lube and slider-lube-disk interactions become the main concerns of head-disk interface at such small spacing. Unfortunately, those commercial optical fly-height

testers, for instance, the Phase Matrices testers, use the special glass disks without the carbon overcoat and lubricant layer to test fly-height, which clearly cannot identify the problems related to lubricant. Furthermore, the normal optical apparatuses have no means to access the operating conditions inside the actual disk drives and cannot detect the gradual avalanche effect of head-disk crash and could not reflect the real time fly-height modulation. In addition, the tester delivers poor repeatability for small fly-heights of 5-6 nm in practice.

The in-situ characterization of head-disk spacing provides an alternative approach to solve the shortcomings of the conventional optical methods. In magnetic recording, 'in-situ' refers to the method that the readback signals that are directly from the preamplifier output and preceding the equalization channel are directly utilized to obtain the useful information about the head-disk system. In-situ characterizations of the head-disk system can reflect the actual scenario in the disk drives since no other medium is introduced to carry the wanted information except the magnetic flux. Among the various in-situ fly-height measurement methods, the most promising one is the triple harmonic method based on the variation of the IBM's harmonic ratio fly-height method (HRF)[2].

1.3.2 Simulation Platform Development for Head-Disk System

The motivation of simulation platform development is to provide a virtual design and evaluation environment to promote the understanding of the complicated head-disk systems and to explore new methodologies. The platform could be a powerful tool to study the readback signal based head-disk system characterization methods with flexibility of theory model selection and parameters setup.

The triple harmonic method is based on harmonic ratio of readback signal of MR sensor in the present technology. In-depth analysis of the accuracy and resolution of this method requires accurate mathematical modeling of the readback signal with MR head as a transducer. But unfortunately, so far this method has only been studied based on simple equations and its unique characteristics in engineering applications have not been given enough theoretical support. Direct calculation of the flux is very complicated, but with the reciprocity principle which utilizes the fact that the playback process involves the mutual induction between the magnetic media and playback head, we could study the readback signal characteristics with the information obtained from the medium transition and the head potential function. There exist several mathematical models for describing the medium transition and the head potential characteristics with different levels of calculation complexity; both the accuracy and calculation complexity should be considered and compromised in the modeling work. Since readback signal with MR transducer has some unique characteristics compared with that of inductive head, discussion should be focused on the reason and consequences induced by these unique characteristics. The information gotten in time domain signal and in frequency domain could help us in characterizing head medium interface and should be analyzed. But special attention should be on characteristics in frequency domain since the harmonic ratio of the read back signal is of our interest in this method.

1.3.3 Evaluation of Harmonic Based Fly-Height Measurement Method

The measurement errors of harmonic ratio fly-height methods in experiment deserve exploration. Both testing sensitivity and accuracy should be considered as the criteria

of evaluating of harmonic based fly-height measurement method. The factors leading to measurement error are investigated with the experimental work to verify the feasibility of the method in Chapter 4.

1.3.4 Gap Length Variation Estimation Method

Investigations suggest that the variation of gap length can limit the achievable recording density of the head, as increased gap width will degrade the data retrieval resolution of the reading head at high bit density. Therefore, it is important to develop suitable methodology for the testing and evaluation of gap length fluctuation not only during head fabrication process (wafer level) but also at magnetic integration level (read/write testing level). However, there is as yet only limited literature in public domain reporting on gap length characterization method at magnetic integration level, and the existing methods require knowledge of many system parameters in the first hand and require complex data analysis technology. It is of great value to explore a new method with high sensitivity and easy to implement even under the circumstances that only limited system parameters are known. In Chapter 5 we propose a novel method to evaluate the gap length variation among a batch of heads. The proposed method is simple and easy to be implemented in any read/write test of recording heads.

1.3.5 High Density Recording and High Data Rate Recording

To meet the tremendous demand of data storage, the recording density of the HDDs has to be increased continuously. Areal density improvement has been achieved by increasing both the linear and the track densities. In high density and high data rate recording, there are some factors that affect the characterization of head medium

interface with triple harmonic method and are hence worthy of in-depth investigation.

Firstly, since high write frequency is required to achieve high density and high velocity is required to achieve data rate, the channel response effect and finite flux rise effect are also observed in the experiment and discussed. All these factors should be considered and compromise may be needed to achieve high testing accuracy in high density and high data rate recording. Secondly, there exists demagnetizing fields generated from the upstream and downstream transitions which affect the formation of new transitions and thus cause position shifts of the newly formed transitions. Such interferences, known as nonlinear transition shift (NLTS) or hard transition shift (HTS), disobey the linear superposition of the isolated pulses and degrade the detection capability of the Partial-Response Maximum Likelihood (PRML) channel. The nonlinear effects on triple harmonic method in high density and high data rate recording are studied theoretically and experimentally in Chapter 6.

Thirdly, with the decrease of track width, the slider can easily go off-track due to the head disk interface vibration, since the servo required to position the head accurately on the track center becomes more difficult with decreasing track width. Furthermore, track-edge recording phenomena become very important with small track widths. Thus, the behaviors of the read/write heads with off-track displacement and the playback voltage response in the cross-track are also of interest. These phenomena are observed in experiment and studied with simulation modeling and theoretical analysis in Chapter 7.

1.4 Contributions and Organization of the Thesis

Given the importance of in-situ characterization of the head disk systems in the development of disk drives, this thesis focuses on in-depth theoretical and experimental study on readback signal based in-situ characterization of head medium system. At first, the various fly-height measurement methods are reviewed and the appropriate method for the areal density beyond 100 GB/in^2 is identified to be the triple harmonic method (THM). Then theoretical models are implemented to analyze the triple harmonic method and to understand how the head-disk system parameters affect the readback harmonic ratio. In-depth analysis of harmonic ratio based fly-height testing methods is done based on sensitivity and repeatability. And methods of estimating gap length on harmonic analysis are proposed and verified experimentally. To improve the accuracy and resolution of the triple harmonic method, some problems such as nonlinear transition shift, channel response effect, finite flux rise time effect, and off-track effect that may be faced in high density and high data rate recording, are studied theoretically and experimentally.

The rest of the dissertation is organized as follows:

Chapter 2 gives a brief review and analysis of fly-height testing technologies. Then the most promising approach of readback signal based triple harmonic method of in-situ fly-height measurement method and its advantages that make it suitable for high recording density are discussed.

Chapter 3 describes a platform developed for the characterization of head-disk system. The software interface and functions are described first, and then typical simulation results and their theoretical models are described.

Chapter 4 analyzes harmonic ratio based fly-height testing methods based on sensitivity and repeatability.

Chapter 5 proposes a method for estimating the gap length based on harmonic analysis. The experimental hardware setup is introduced, and the theory and experimental results are described.

Chapter 6 analyzes the challenges and problems like NLTS, HTS, finite flux time, and channel response effect faced in high linear density and high data rate recording, and their effects on readback signal and triple harmonic method are studied experimentally and theoretically.

Chapter 7 analyzes off-track effect and track-edge effect on fly-height testing in high track density recording.

Chapter 8 provides a summary of the work done in the dissertation and proposes the directions of future work.

Chapter 2

Fly-Height Measurement

As mentioned in the previous chapter, both fly-height and stability of fly-height are important for ultra-high density magnetic HDDs. Therefore, the following two factors are of great importance for the characterization of sub-10 nm spaced head-disk systems. The first is testing accuracy or the achievable resolution, and the second is the feasibility for in-situ characterization of slider-lubricant and slider-disk interactions.

Traditional optical measurement can give absolute value of head-disk spacing by replacing actual disk media with a transparent glass disk. However, its resolution is limited by the wavelength of the light used for the testing and testing electronics. In other words, the resolution can not be automatically increased as technology moves to higher density. Furthermore, it is difficult for the optical fly-height testers to evaluate the real scenario of slider-lube and slider-disk interaction in the operating disk drives or operating slider-disk systems. On the contrary, the in-situ methods use the available magnetoresistive (MR) read sensor as a transducer to measure the magnetic spacing. Its resolution increases as bit size reduces or head sensitivity increases. Also, it can be used for all kinds of in-situ analysis of slider-disk and slider-lube-disk interactions.

Aiming at identifying the most promising technology for future fly-height measurement, various possible fly-height testing technologies, including both interferometry based fly-height testing technology and various in-situ fly-height testing methodologies, are reviewed and discussed in terms of working principle,

benefits and drawbacks.

2.1 Optical Fly-Height Testing Methods

The optical interferometry based fly-height measurement method has been widely used in industry in the past 30 years to determine the absolute fly-height. With the decrease of fly-height, numerous efforts have been made to improve the measurement sensitivity and accuracy, and various technologies were proposed. There has been monochromatic fringe counting technology and white light interfeometry technology [3]. Currently the three-wavelength method [4] is the most widely used in industry. It has higher fly-height repeatability, reproducibility and accuracy compared to other methods, but it still does not have enough sensitivity when technology moves to 5~6 nm fly-height or below. And the variation of complex index of refraction for the slider is a key source of error in fly-height measurement as slider is made of two types of grains, Al_2O_3 and TiC, and these grains are of different refractive indices. Other optical methods investigated up to now include polarization interferometry [5], which utilizes the two polarization states of light with an oblique incident angle below the critical angle, and it can compute the complex index of refraction of the slider in addition to fly-height. This method is more complicated and suffers from birefringence of glass disk due to stress induced by high speed rotation of the glass disk. As a result, the ultimate performance of this method is not better than that of the three-wavelength method.

2.1.1 Three-Wavelength Intensity Interferometry Technique

The three-wavelength method is the method used in the state-of-the-art fly-height tester. Fig. 2.1 shows the schematic illustrating the working principle of the three-wavelength interferometer. A mercury arc lamp light source is used to provide three distinct wavelengths of light so that three separate interference fringes are generated. Light source is directed through a beamsplitter. A portion of the incident light split by the beamsplitter is directed through the glass disk and is internally reflected off the lower surface of the glass disk. Another portion of the light is reflected by slider and the reflected light is redirected to the detector assembly. The light reflected from the slider and from the surface of the disk closest to the slider are combined and spectrally analyzed. The spectral analysis is accomplished by a detector assembly which includes wavelength discriminating beam splitters, optical filters in front of the photodetecter, and a high-speed photo detector for each wavelength. The photodetecotor converts the fringes' intensity into electrical signals which are then converted to digital data.

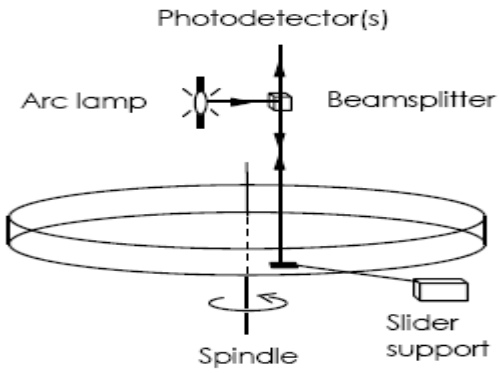

Fig. 2.1 Schematic of three-wavelength fly-height tester

It is important to learn the principle of the interferometry to understand the method. Fig. 2.2 shows the light reflections considering two interfaces and multiple reflection effect. As shown in the Fig. 2.2, the reflected wave returning to glass disk will consist

of light initially reflected from the first interface as well as the light which is transmitted by the first interface after reflection from the second interface. The total outgoing wave is a sum of infinite series of reflected waves.

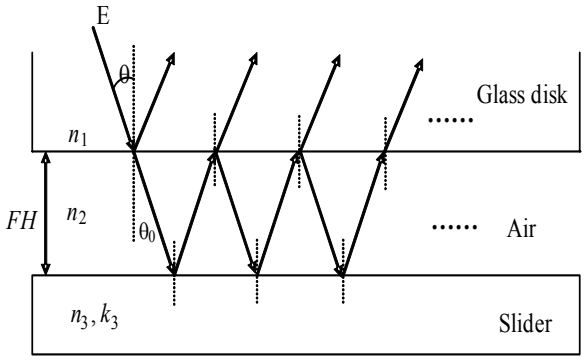

Fig. 2.2 Multi- reflections and transmissions for two interfaces

We define the total reflection coefficient R as the ratio of the amplitude of the outgoing wave to the amplitude of the incoming wave. Considering a single film including two interfaces, the reflection coefficient R can be described as

$$R = \frac{r_{12}^{\ 2} + |r_{23}|^2 + 2r_{12}|r_{23}|\cos(\frac{4\pi n_2 FH}{\lambda} - \Phi_{23})}{1 + r_{12}^{\ 2}|r_{23}|^2 + 2r_{12}|r_{23}|\cos(\frac{4\pi n_2 FH}{\lambda} - \Phi_{23})} \tag{2.1}$$

where $r_{12} = \frac{n_1 - n_2}{n_1 + n_2}$, $r_{23} = \frac{n_2 - n_3 + jk_3}{n_2 + n_3 - jk_3}$ and $\Phi_{23} = \pi\text{-}\tan^{-1}(\frac{2n_2 k_3}{n_3^{\ 2} - n_2^{\ 2} + k_3^{\ 2}})$ .Here, λ is the wavelength, and n_2, n_1 and $n_3 - jk_3$ are the refractive indices of air, glass disk and slider, respectively. Change in fly-height will result in a change of R. The optical constants (n, k) for air, slider and glass disk can be determined by an ellipsometer. So if the total reflection coefficient R is known, the fly-height corresponding to it can be calculated as

$$FH = \left[\Phi_{23} - \frac{r_{12}^{\ 2} + |r_{23}|^2 - (1 + r_{12}^{\ 2}|r_{23}|^2) \cdot R}{2r_{12}|r_{23}| \cdot (1 - R)} \right] \cdot \frac{\lambda}{4\pi}. \tag{2.2}$$

To measure the accurate fly-height, one must get R through a calibration procedure

first. In the calibration process, the slider is first moved to the desired location over the disk surface and light is projected onto the slider. Then the slider is moved away from disk surface to a wide enough slider-disk separation to obtain the maximum and minimum interference intensity. The measurement trace obtained later will be normalized with the maximum and minimum intensities of calibration trace as below:

$$
\begin{aligned}
R &= \frac{I_{out}}{I_{in}} = \frac{I_{meas} - I_{cal\min}}{I_{cal\max} - I_{cal\min}}\left(R_{\max} - R_{\min}\right) + R_{\min} \\
R_{\min} &= \frac{r^2 + s^2 - 2rs}{1 + r^2 s^2 - 2rs} \\
R_{\max} &= \frac{r^2 + s^2 + 2rs}{1 + r^2 s^2 + 2rs}
\end{aligned}
\tag{2.3}
$$

Where r is the reflection coefficient of the glass disk, s is the reflection coefficient of the slider, and $I_{cal\max}$ $I_{cal\min}$ and I_{meas} are the maximum intensity of calibration curve, minimum intensity of calibration curve and the measured intensity, respectively. The purpose of normalization is to consider the effects of photoelectric conversion efficiency and the gain of photodetector. Then the measurement of fly-height is accomplished by comparing the normalized intensity with the normalized theoretical intensity versus fly-height relationship given in (2.1).

2.1.2 Limitations of the State-of-the-Art Optical Fly-Height Test Method

The fundamental limitation of the optical interferometric fly-height testing technique is that the fly-height testing sensitivity reduces as fly-height approaches zero. The sensitivity of the technique is given by the intensity of three wavelengths vs. fly-height plot shown in Fig. 2.3. The point of maximum slope takes place halfway between minimum and maximum intensity. When fly-height approaches zero, the slopes of all

the three curves with different wavelengths are approaching to zero. The slope would be zero at contact if sliders were made of a dielectric material such as glass. Since sliders are made of a composite of alumina and titanium carbide, the light gets phase shifted upon reflection off the slider. The interference fringes move towards lower fly-heights and thus the point of zero sensitivity moves out to "negative" (i.e. non-physical) fly-heights.

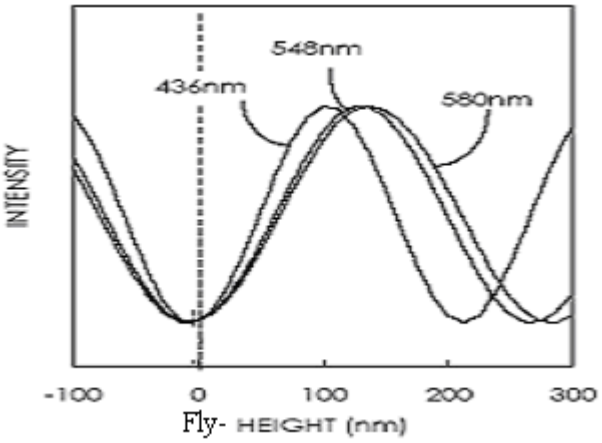

Fig. 2.3 Sensitivity of the optical fly-height test method

As Fig. 2.3 shows, the intensity modulation for all wavelengths has a vanishing derivative at low fly-heights. The trend in slider manufacture is towards ultra-low fly-heights, where this fundamental difficulty is becoming a concern. It has become evident to many researchers that simply measuring the reflected intensity from the slider-glass interface will not be enough to meet fly-height testing accuracy of the next generation head-sliders.

Another factor that may affect measurement accuracy comes from the optical constants. The slider substrate is formed of composite materials (Al_2O_3 and TiC). The two materials are of different optical properties, including refractive index. As a result, the index of refraction varies from spot to spot over slider surface. Since the index of

refraction of the slider plays an important role in the determination of fly-height, inaccurate determination of the index of refraction becomes source of error of this method. Furthermore, the calibration point for fly-height testing can be different from the measurement point. Thus, error caused by refractive index difference between the calibration point and testing point can lead to further increased error in fly-height measurement.

As in other optical methods, this technology uses special glass disks to test fly-height. These glass disks are different from the actual disks used in disk drives. Therefore, they are not directly linked to the problems related to actual slider-disk and slider-lubricant interactions. Since the head-disk spacing is becoming very small today, frequent intermittent or continuous contacts occur during normal steady state operation in disk drives, and hence the slider-lube and slider-lube-disk interactions become one of the main concerns of head-disk interface at such a small spacing. With optical fly-height method, it is difficult to access the operating conditions inside the actual disk drives, and so we cannot detect the gradual avalanche effect of head-disk crash and could not reflect the real time fly-height modulation.

Taking into consideration all the limitations of the state of art optical fly-height technology, people look into in-situ fly-height test method for better solution to the problems we are facing today as well as the problems we will be facing in the future.

2.2 In-Situ Fly-Height Testing Methods

In this section, the various in-situ fly-height testing methods are categorized into the reading process based methods and the writing process based methods, and are

reviewed and discussed in terms of working principles, benefits and drawbacks. A small stream of in-situ methods, known as capacitance method, is also reviewed.

2.2.1 Reading Process Based Methods

The reading process based approach is established based on the Wallace equation and Karlqvist head model [6]. It is assumed that the writing process is far less sensitive to the variation of head-disk spacing. Such an assumption is acceptable when the maximum head field acting on disk media is 2-3 times as high as medium coercivity. The reading process based methods can be classified as two categories: waveform based methods and harmonic analysis methods [7].

2.2.1.1 PW50 Method

Waveform method detects the variation of head-disk spacing by the relationship between head-disk spacing and the shape of the isolated readback pulses [7]. The most representative waveform method is the PW_{50} method reported by Klaassen and van Pepen [8]. Here, PW_{50} refers to the width of isolated pulse at 50% of its amplitude and it is a key parameter that reflects the shape of the readback pulses.

In view of the complication of hardware implementation for this method, a simplified PW_{50} method based on the isolated readback pulse shape is proposed by Liu *et al.* [7] to derive the head-disk spacing. In this approach, the ratio of the integration of isolated readback pulse v_i to the peak value of each readback pulse v_{peak} is proportional to the PW_{50} if the isolated readback pulse can be approximated by the Lorentzian equation,

as shown in Eq. (2.4).

$$v(x) = \frac{c}{1 + (\frac{2x}{PW_{50}})^2} \tag{2.4}$$

where c is a factor that is proportional to the track width, media's remanent-moment-thickness product ($Mr\delta$) and the sensitivity of the reading head used. The peak value of each readback pulse (v_{peak}) and the integration (v_i) of the isolated pulse can be expressed by the following equations:

$$\begin{cases} v_{peak} = c \\ v_i = \int_{-\infty}^{+\infty} V d_x = \frac{\pi}{2} c \cdot PW_{50} \end{cases}. \tag{2.5}$$

The ratio of the integration to the peak value becomes proportional to the PW_{50} only:

$$\frac{v_i}{v_{peak}} = \frac{\pi}{2} PW_{50}. \tag{2.6}$$

If a thin medium and a small gap Karlqvist head are considered, PW_{50} of the readback voltage pulse can be expressed as [6]

$$PW_{50} = \sqrt{g^2 + 4(a+d)^2} \tag{2.7}$$

where g is the Karlqvist equivalent gap length of the MR head, d is the effective magnetic spacing and a is the transition parameter. The assumption behind Eq. (2.7) is valid for the current areal density of 60 Gb/in^2 in the longitudinal recording products. But it is not true for the perpendicular recording system, as the isolated readback pulse cannot be approximated by Lorentzian equation.

The head-disk spacing can be estimated by the following equation [7] assuming media thickness $\delta << d$:

$$d = \frac{\sqrt{(\frac{2v_i}{\pi v_{peak}})^2 - 2g^2}}{2} - a \,. \tag{2.8}$$

The PW_{50} method is easy to implement and the noise in the integration waveform is small. Such a method has significantly reduced sensitivity to track mis-registration, compared with the method based on analysis of the amplitude of readback signal. Furthermore, the effect of micro-fluctuation of media's remanent-moment-thickness product ($Mr\delta$) to the testing result can be small, compared with the amplitude based method. Nevertheless, the sensitivity of this method is not high enough and the method has not been accepted as an established method for absolute fly-height testing technology yet.

2.2.1.2 Harmonic Method

The harmonic methods rely on Wallace's spacing loss equation [6] to extract fly-height information. The first harmonic ratio method (HRF) is patented by Brown *et al*. [2]. Triple harmonic method with special code proposed by Liu *et al* [7] has higher sensitivity in comparison with the conventional HRF method. The basic principles will be introduced here and the in-depth analysis will be given in Chapter 3.

The Wallace's description on spacing induced signal loss is part of the Fourier transform of the read back voltage pulse given by

$$V(k) = C(k) \cdot e^{-ky_0} \tag{2.9}$$

$$k = \frac{2\pi}{\lambda} = \frac{2\pi f}{ve} \tag{2.10}$$

where C (k) represents the factors independent of the magnetic head spacing, λ is the

recording wavelength, *f* is the recording frequency, y_0 is the magnetic head spacing, and *ve* is the spindle speed or the relative speed between head and disk medium.

Suppose a periodic signal at a predetermined frequency *f* is recorded and we detect the ratio of two different harmonic amplitude of the readback signal $V(k)$ at the frequencies f_1 and f_n. This harmonic ratio is processed as a voltage proportional to the logarithm of a harmonic signal amplitude ratio. The output of the HRF detector in its most general form, is given by

$$V_{HRF} = K \ln \frac{aV(k_1)}{bV(k_n)} = K \ln \frac{V(k_1)}{V(k_n)} + K' \tag{2.11}$$

where K is an electronic gain factor and K' is an arbitrary electronic offset caused by the different gains at the two measured frequencies due to the frequency response of system.

To achieve high SNR and thus measurement accuracy in the test, the HRF method uses the ratio of the fundamental and third harmonics of a square wave readback signal to derive the change of head-disk spacing as they can provide greater signal power than other kind of possible harmonic signal combinations.

By subtracting the HRF output for the same pre-written track but read out at different height, the change in magnetic spacing (Δd) between any two measurements can be computed from the corresponding change in output voltage (ΔV_{HRF}), depicted as follows:

$$\Delta d = \frac{\lambda}{4\pi K} \Delta V_{HRF} . \tag{2.12}$$

By subtracting the HRF output for a normally flying head from the output when the head has landed, one can find the absolute magnetic spacing; otherwise its variation could be observed. The problem with the HRF method is that the intensity of higher order harmonics from the periodic signal decreases too fast at high densities compared with that of the fundamental component, and hence it is not able to sustain sufficient SNR for achieving high accuracy of fly-height variation at high user density.

2.2.1.3 Triple Harmonic Method

The triple harmonic method is a quite successful HRF method. The unique characteristic of the triple harmonic method is that it uses a special "111100" code pattern instead of the conventional all-one pattern of the HRF method. From Eq. (2.9), the harmonic amplitude ratio can be simplified as

$$\frac{V_3}{V_1} = A_{31}k(g,\delta)\exp\left[\left(-\frac{2\pi d}{\lambda_3}\right)-\left(-\frac{2\pi d}{\lambda_1}\right)\right] = A_{31}k(g,\delta)\exp\left(-\frac{4\pi d}{3\lambda_3}\right) \qquad (2.13)$$

where A_{31} is the harmonic amplitude ratio factor, $k(g, \delta)$ is a factor determined by the gap length g of the read head and the medium thickness δ, λ_1 and λ_3 are the recording wavelength of the first and third harmonic, respectively, and d is the effective magnetic spacing.

From Eq. (2.13), the effective magnetic spacing can be expressed as follows:

$$d = -\frac{3\lambda}{4\pi}\cdot\ln\left(\frac{V_3}{V_1}\right)+C_d \qquad (2.14)$$

where C_d is a constant dependent on the various system parameters, such as the track width, $Mr\delta$ value of the media, the gap length g of the read head, *etc*. With a

reference measurement, the relative fly-height variation (ΔFH) can be obtained using

$$\Delta FH = -\frac{3\lambda}{4\pi}\left[\ln\left(\frac{V_3}{V_1}\right) - \ln\left(\frac{V_{30}}{V_{10}}\right)\right], \tag{2.15}$$

where V_{10} and V_{30} are the amplitude of the first and third harmonic of the reference position, respectively.

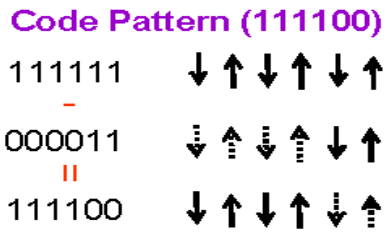

Fig. 2.4 The formation of the "111100" code pattern

From Fig. 2.4, it can be seen that the "111100" code pattern is effectively a combination of the all-one pattern and the "000011" code pattern. With this special combination, the energy distribution of the harmonics is different from the conventional HRF method. The special "111100" code pattern provides three major harmonic components. Compared with HRF, the lower harmonic intensity is suppressed at low density but at high density the intensities of the three harmonic components are comparably high within a large range, which enables it to sustain sufficient SNR for achieving high accuracy of fly-height variation at high user density.

Furthermore, the experimental results show that the triple harmonic method has many good aspects [9], such as high harmonic signal intensity at high channel density, which is defined as the ratio of PW_{50} to the physical bit length, high fly-height testing sensitivity due to its high harmonic intensity at high channel density and so on. It has been reported that the relative testing accuracy of the triple harmonic method can achieve up to ± 2% of the magnetic spacing [9]. Hence, it is a good solution to

characterize the flying condition and test the slider-lube-disk interaction for sub-10 nm fly-height systems.

2.2.2 Writing Process Based Methods

The writing process based methods include carrier erasure current method and scanning carrier current method. They use "writing" or "erasure" operations to record the variation of magnetic spacing during transient process and are designed to analyze the variation of the head-disk spacing during dynamic transient process, such as track seeking process and loading/unloading process.

2.2.2.1 Carrier Erasure Current Method

Carrier erasure current method [10] is proposed by Liu and Chen to record the variation of the head-disk spacing caused by dynamic operations such as seeking, dynamic loading/unloading, head's take-off process, and so on. The process includes three steps: Firstly, record with a saturating writing current, secondly, record with a predetermined erasure current to modulate the magnetization difference, and finally, readback to obtain the magnetic spacing variation by comparing the original signal amplitude and the amplitude drop caused by the erasure operation.

Assume that the head field varies with the magnetization near the remanence coercivity H_{cr} linearly, from H_1 to H_2, the magnetization difference after carrier current erasure is given by

$$M_r - M = M_r - \frac{2M_r}{H_2 - H_1}(H_e - H_{cr}) \tag{2.16}$$

where M_r is the remanent magnetization, and H_e is the head field in the erasure process.

The readback amplitude before carrier current erasure (V_0) and after carrier current erasure (V) can be expressed as:

$$V_0 = 2M_r \cdot f(\beta_{head}, g, a, d_r, \delta) \tag{2.17}$$

$$V = f(\beta_{head}, g, a, d, \delta)[M_r - \frac{2M_r}{H_2 - H_1}(H_e - H_{cr})] \tag{2.18}$$

where $f(\beta_{head}, g, a, d_r, \delta)$ is a factor describing the dependence of readback amplitude on head's magnetic coefficient β_{head}, gap length g, transition region length a, head-disk spacing during the readback process d_r and the medium thickness δ. Factor $f(\beta_{head}, g, a, d_r, \delta)$ will be of the same value whether we are reading the original signal (V_0) or the residual signal (V) after carrier current erasure. Then the spacing variation Δd can be retrieved from the residual to original ratio of the readback signal given by

$$\frac{V}{V_0} = \frac{1}{2} + \frac{2g \cdot \Delta d}{\eta\left[g^2 + 4(d_0 + \delta)^2\right]\tan^{-1}\frac{g}{2(d_0 + \delta)}} = \frac{1}{2} + S_{V/V_0} \cdot \Delta d \tag{2.19}$$

where $S_{V/V0}$ represents the sensitivity and the slope of the relationship.

The advantage of carrier current erasure method is that it has a higher sensitivity than the PW_{50} method. Furthermore, it is easy to implement as it is based on the amplitude measurement in the reading process. Its sensitivity and test range are also selectable. But the spacing testing range of this carrier erasure current method is still small and can't meet the requirement for head disk interaction analysis in loading/unloading

process.

2.2.2.2 Scanning Carrier Current Method

The scanning carrier method, proposed by Liu and Yuan [7], uses “writing” or “erasure” operations to record the variation of the head-disk spacing during such transient processes. The recorded spacing variation is retrieved by reading operation and the effects caused by possible head-disk spacing variation in retrieval process must be small.

The pre-recorded magnetic transitions will not be affected at the time/position when the scanning current is zero. The readback signal from this position serves as a reference signal in the fly-height retrieval process. The phase variation of the scanning current is recovered by detecting the envelope of the readback signal. As the amplitude of the scanning current is known, the current value applied in scanning current erasure process can be derived based on the retrieved phase information. Therefore, the variation of coercive current in each cycle of carrier current scanning can be derived. Here, the coercive current is the value of carrier current which makes the readback signal reduce to half of its original value. In other words, the coercive current is the current value which generates a head field equal to its coercivity over the disk media. The media coercivity is assumed to be constant and the head field can be described by Karlquist equation. The variation of head-disk spacing can be obtained from the following equation:

$$\frac{I_{c0}}{I_c} = \frac{\tan^{-1}(\frac{g/2}{d_0 + \Delta d + \delta})}{\tan^{-1}(\frac{g/2}{d_0 + \delta})} \tag{2.20}$$

$$d = \frac{g}{a\tan[\frac{I_{c0}}{I_c}\tan^{-1}\frac{g}{2(d_0 + \delta)}]} \tag{2.21}$$

where I_{c0} and I_c are the coercive currents in track following status and in the transient process, respectively, and d_0 and d are the head-disk spacing in track following status and in the transient process under investigation ($d=d_0+\Delta d$), respectively. The scanning carrier current method is flexible in applications since the scanning current can vary from zero to the maximum allowed writing current to test the wide range of head-disk spacing in the load/unload process.

Although the scanning carrier method is better than the carrier erasure method in terms of the testing range and noise resistance, however, as far as the higher areal density is concerned, the required in-situ techniques should be able to measure a smaller head medium spacing with better resolution. Both writing process based methods cannot fulfill such a need and are not suitable for drive-level measurements.

2.2.3 Capacitance Method

Capacitance measurements have been used in hard-disk industry since its inception. The basic principle of this method is that fly-height is inversely proportional to the capacitance of electrically conductive slider and electrically conductive disk. This method is useful as its sensitivity increases inversely with distance. It has many applications for precise capacitance measurements between sliders and disks:

• Head-disk capacitance can be readily correlated with stiction forces.

• Fly-height, pitch and crown of actual sliders can be measured by introducing a specially prepared capacitance-stripe disk.

• Capacitance microscope was designed and developed for magnetic hard-disk studies.

Flying a special slider on an electrically conductive disk provides a means by which capacitance can be used to characterize head-disk interface [11]. The special slider can have special conducting probes at 3 separate points. The capacitance between each probe and the disk is measured, and the fly-height at each point can thus be computed. By using three probes, the fly-height, pitch and roll can be calculated.

For each probe, the capacitance is given by

$$C = \varepsilon_0 \int_0^W \int_0^L \frac{d_x d_y}{h + x\tan\theta - y\tan\phi} \tag{2.22}$$

where W is width of capacitance probe, L is length of capacitance probe, h is slider fly-height above conduction surface, and ϕ is slider roll angle. This equation has three unknowns and can be solved numerically if the capacitance is known for three probes, each at different points of the slider. At each probe, the fly-height variation, Δh, causing an observed capacitance fluctuation, ΔC, is given by

$$\Delta C = \frac{\varepsilon_0 WL}{h(h + \theta L + \phi W)} \Delta h \tag{2.23}$$

where ε_0 is the dielectric constant.

Furthermore, the capacitance variation due to the fly-height change can be observed in-situ with some electrical circuits producing an electrical measurement signal

representing the capacitance value as a function of time. Since this technique requires embedding some electrical component into the slider, delicate fabrication process is required to avoid physical disturbances on the slider, and it requires precise calibration. Due to this reason, the use of capacitance method has been very limited.

2.3 Summary

Comparing the merits and demerits of the optical and electrical in-situ measurement techniques, one can conclude that the best way to characterize actual head-disk systems is to use head itself as transducer. Therefore, the triple harmonic method, which uses harmonic ratio of readback signal from MR sensor to estimate the fly-height, is the most proper candidate for the fly-height testing at same conditions as the actual head-disk systems. Hence, in this thesis, we will concentrate on studying the triple harmonic method and its application in characterizing the recording system performance with head itself as transducer.

Chapter 3
Simulation Platform Development

This chapter describes author's effort in modeling and simulation of the magnetic interaction and inter-dependence of magnetic head and magnetic disk-media -- the magnetic head-disk systems.

The modeling and simulation work leads to the establishment of a software platform for the evaluation of head-disk systems. The platform provides the convenience for the analysis of the effects of read/write parameters on the overall quality of readback signal. The platform proved to be a useful tool to study and explore head-disk system characterization methods based on the readback signal. The platform provides the flexibility of theoretical model selection and parameters setup.

This chapter has four sections, with section 3.1 on introduction of the overall function and user interface, and section 3.2 on the modeling of magnetic transitions and MR reading head based readback process. In section 3.3 the multi-transition waveform and roll-off curve are simulated. Section 3.4 includes spectral analysis of the readback signal, which is the foundation of the triple harmonic method.

3.1 Platform Development

3.1.1 Motivation and Functions Developed

The motivation of simulation platform development is to provide a virtual design and

evaluation environment to promote the understanding of the complicated head-disk systems and to explore new methodologies.

The analysis is focused on readback signal. The readback signal is obtained from the magnetization transition on magnetic disk media and the head potential function. There exist several mathematical models for describing the medium magnetization transition and the head potential characteristics with different levels of computational complexity. The results from different models could be obtained and compared.

.

Here are a few key system parameters that will have big effect on system performance and deserve exploration. The key parameters to be included in the modelling are the following: the fly-height (FH) of read/write head, MR head gap length, magnetic transition parameter, and recording medium thickness.

The exploration of new methods is based on in-depth understanding of the parameter effects on the time and frequency domain results. With the input of different values of fly-height, gap length, transition parameter, medium thickness etc, we could easily evaluate system performance with various functions such as waveform, roll off curve and spectrum power.

With the platform, different patterns could be generated and their frequency and harmonic response could be compared and analyzed.

With the help of platform, we could study the major engineering issues faced in high density recording and explain it with theoretical models. One important phenomenon

at high bit density is the non-linear transition shift (NLTS), which appears when channel density reaches certain level and increases as channel density is further increased. The NLTS effect faced in high linear recording could be studied and evaluated by the platform developed, and track-edge effect faced in high track density recording could be simulated with this platform taking into consideration the transition bending and transition parameter non-uniformity, and the micro-magnetic result could be used for comparison. Details will be discussed in chapter 6.

3.1.2 User Interface

The user interface of this platform is developed with Visual C++ and the main dialog window is illustrated in Fig 3.1. The values set by the user are saved in *.txt file and the respective script of the functions programmed with MATLAB are called.

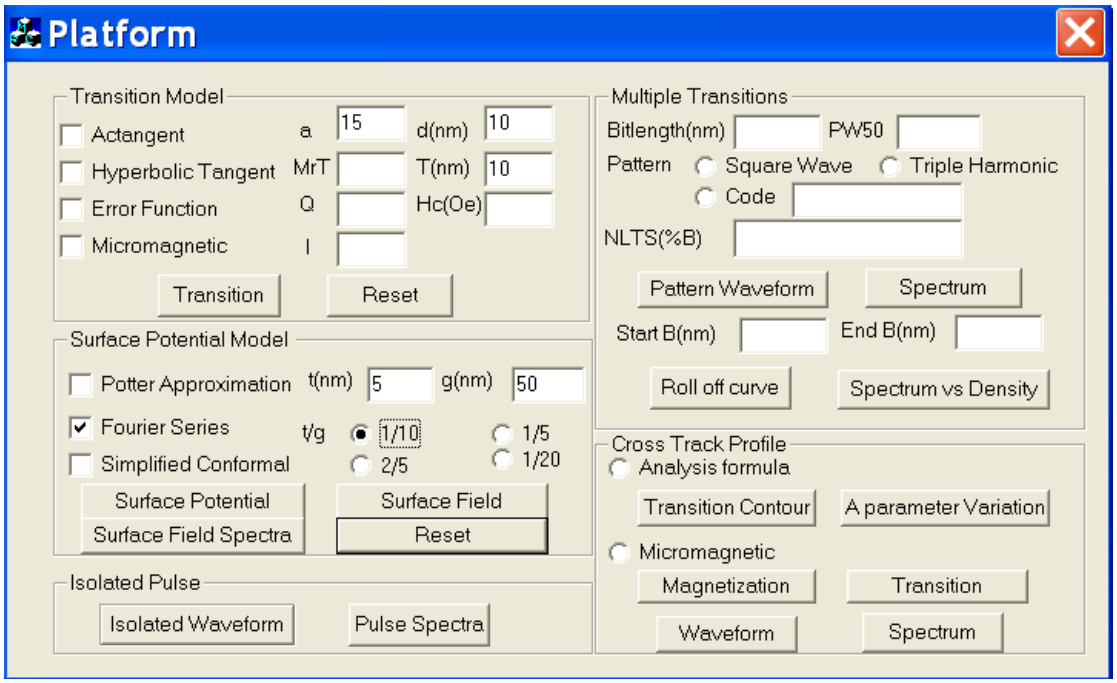

Fig. 3.1 User interface of simulation platform

The relationship and interdependency of the functions included in the platform are illustrated in Fig 3.2. As seen, some of the functions are based on the result of the

other functions and the user's input determines the data flow of the platform. Taking into consideration the cross-track transition bending effect and transition parameter non-uniformity, the waveform and spectrum of cross-track direction could be simulated. In this chapter, the readback signal at track center is considered and track averaged transition profile is used for calculation. The principles of calculation results of the functions are detailed in the following sections.

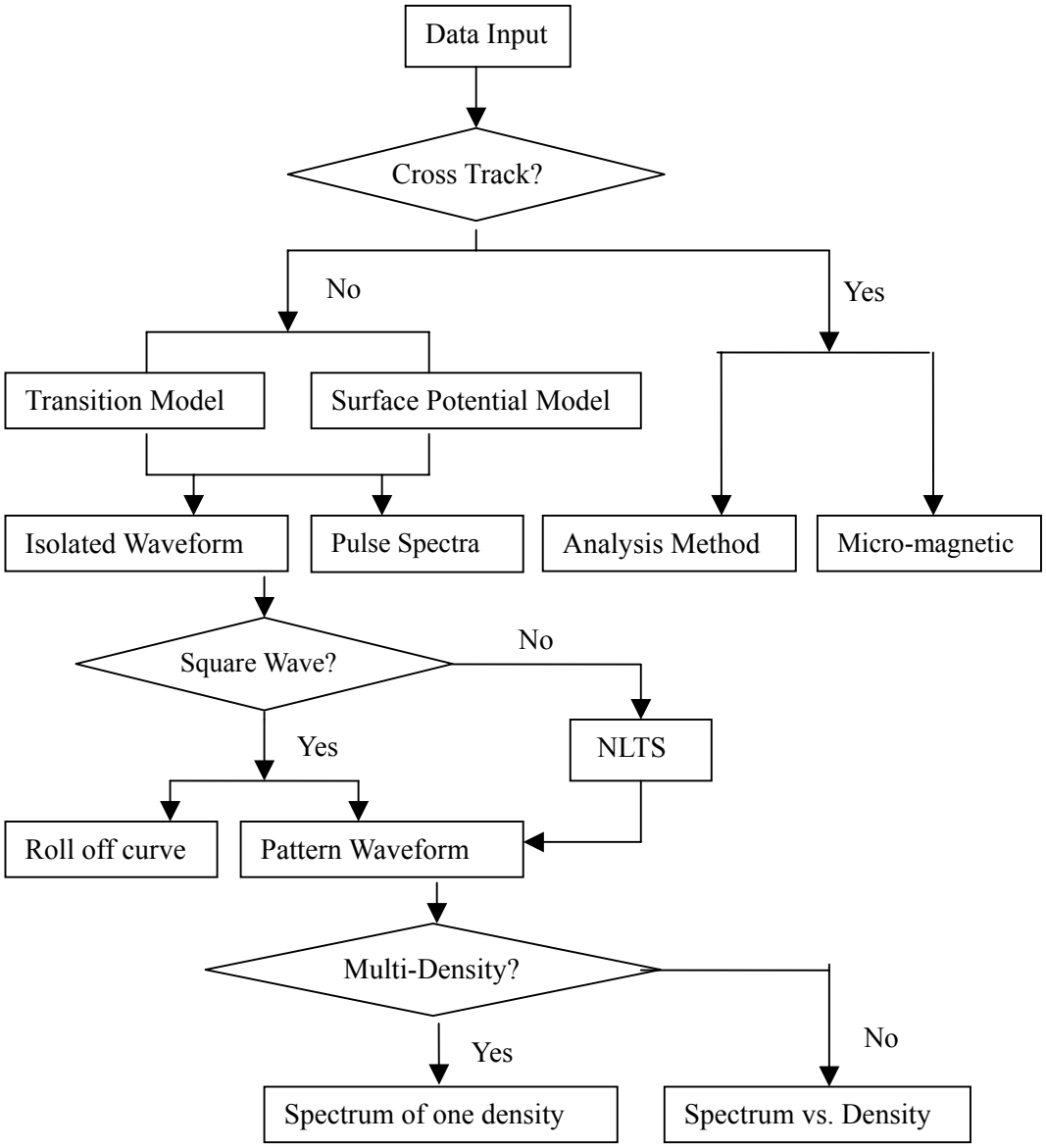

Fig. 3.2 Data flow diagram

Modeling of the track-edge effect and transition bending effect will be presented in chapter 6 and the work is based on the same platform presented in this chapter.

3.2 Transition Modeling and Playback Signal Modeling

3.2.1 Medium Transition Model of the Write Process

The calculation of playback signal of reading head requires a model for the form of the medium magnetization transition. For a one-dimensional geometry with variations in the down-track direction, the magnetization and its differential form can be written as

$$M_x(x) = F_{loop}(\bar{H}_h(x) + \bar{H}_d(x)) \tag{3.1}$$

$$\frac{dM_x(x)}{dx} = \frac{dF}{dH_{tot}}\left(\frac{d\bar{H}_h(x)}{dx} + \frac{d\bar{H}_d(x)}{dx}\right) \tag{3.2}$$

where $H_h(x)$ and $H_d(x)$ are the write field and the demagnetizing field generated by the transition being written, respectively, F_{loop} is a generalized hysteresis function for the medium, and H_{tot} is the sum of the write field and demagnetization field. The bars refer to an average done over the medium thickness.

A general solution for the transition shape requires a complicated iterative procedure. The simplification used by Williams and Comstock [12] is to assume an asymmetric transition shape which varies from $+M_r$ to $-M_r$. The three mostly used transition shape models and their Fourier transforms are listed in Table 3.1 and are illustrated in Fig. 3.3.

More accurate modeling of the magnetization transition formed by writing operation can be obtained by micro-magnetic modeling. The transition shape simulated with micro magnetic model is also plotted in Fig. 3.3 for comparison.

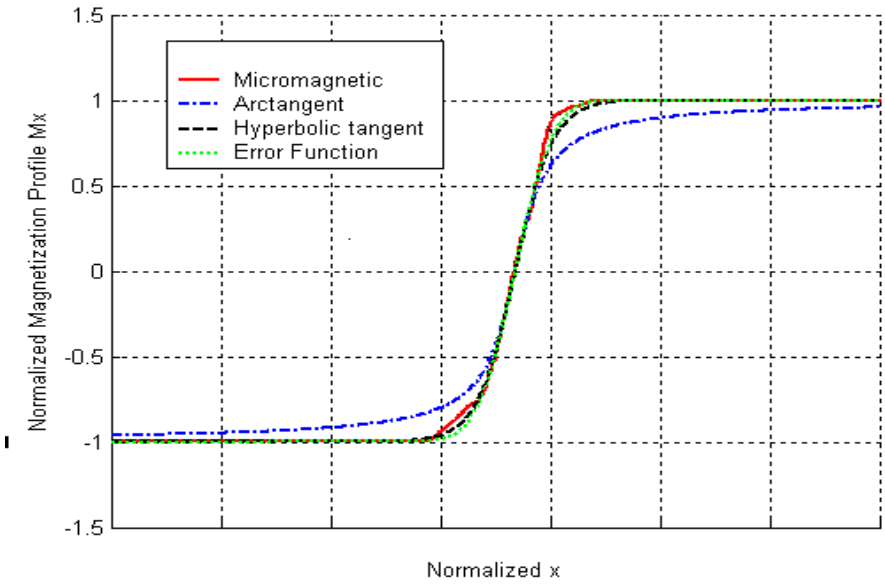

Fig. 3.3 Transition shapes of mostly used functions and micro magnetic model

Transition	$m_x(x)$	dm_x/dx	$M_x(k)$
Arctangent	$\frac{2M_r}{\pi}\tan^{-1}\left(\frac{x}{a}\right)$	$\frac{2M_r}{\pi}\frac{a}{(x^2+a^2)}$	$j\frac{2M_r}{k}e^{-ka}$
Hyperbolic Tangent	$M_r\tanh\left(\frac{2x}{\pi a}\right)$	$\frac{2M_r}{\pi a}\sec h^2\{\frac{2x}{\pi a}\}$	$j\frac{\pi^2 aM_r}{2}\csc h\left(\frac{\pi^2 ka}{4}\right)$
Error Function	$M_r\frac{2}{\sqrt{\pi}}\int_0^{\frac{x}{a\sqrt{\pi}}}e^{-t^2}dt$	$\frac{2M_r}{\pi a}e^{\frac{-x^2}{\pi a^2}}$	$j\frac{2M_r}{k}e^{\frac{-\pi k^2 a^2}{4}}$

Table 3.1 Transition models used in the modeling platform

The hyperbolic tangent and error function transitions have sharper corners between the transition region and the remnant moment M_r compared to arctangent shape. The actual shape of transitions is found to be closer to the hyperbolic tangent and error function models by fittings to signal roll-off curves and noise spectra [13][14]. And our micro magnetic simulation result also verifies this finding. But arctangent transition shape has a particularly simple convolution property that makes it theoretically convenient for analysis in playback signal calculation.

The transition parameter a could be estimated as

$$a = \frac{(1-s^*)y}{\pi Q} + \sqrt{\left[\frac{(1-s^*)y}{\pi Q}\right]^2 + \frac{M_r \delta y I}{\pi Q H_c}} \tag{3.3}$$

where s^* is the coervice squareness, δ is the medium thickness, H_c is the medium coercivity, and $y = d + \delta/2$ is the total magnetic spacing between the center of the medium and the surface of the write head. The value of I is a parameter which is determined by the writing field and media magnetic hysteresis loop. Its value ranges from 0.64 to 1.0. The value of Q is typically around 0.8 when deep gap field is around 3-4 times the media H_c which is the normal case for most recording systems. As a good approximation, the transition parameter for high moment media is given by

$$a \approx \sqrt{\frac{M_r \delta (d + \delta/2) I}{\pi Q H_c}} \ . \tag{3.4}$$

The width of the transition has a direct effect on the width of the playback signal pulse. For higher densities the transition widths must be made smaller to pack more information on the disk.

3.2.2 Reading Process Modeling and MR Head Reciprocity

3.2.2.1 Reciprocity Algorithm

Though inductive reading heads were used many years ago, the magneto-resistive (MR) reading head is the dominant head structure in current magnetic data storage systems. Therefore, the work of this thesis is focused on MR reading head only.

The basic concept of playback with MR head is that when magnetic flux comes into

the playback sensor as the sensor passes through the recorded magnetization transitions in the medium, then a rotation of the magnetization in the MR layers occurs. The change in resistance of the MR element which, in turn, results in a change in the voltage across the sensor. Thus, the recorded information is translated into measurable voltages.

The reciprocity principle utilizes the fact that the playback process involves the mutual induction between the magnetic media and playback head [15]. For MR heads, it is only applicable to the case in which the signal field from recorded media is sufficiently small so that the device works in the linear regime [16]. The general form of the readback signal for 3D structures is given by

$$v_{MR}(x) = \frac{2J\Delta\rho}{htM_s^2} \int_{vol} \bar{H}(r' + x)\, m^{rec}(r')\, d^3r' \tag{3.5}$$

where J is the current density in the MR stripe, $\Delta\rho$ is the magneto resistive change, h is the stripe height, t is the element thickness, M_s is the saturation magnetization of the MR element, $\bar{H}(r)$ is the field due to the fictitious current density and $m^{rec}(r)$ is the recorded medium magnetization pattern. The integration is over the entire volume of the recorded medium.

Shielded GMR heads are of practical interest because of their higher spatial resolution. The geometry of a shield structure is shown in Fig. 3.4. For shielded heads, (3.5) becomes

$$v_{MR}(x) = \frac{2J\Delta\rho E_{MR}\langle \sin\theta_0 \rangle}{M_s t_{MR}} \int_{vol} \Phi_{MR}(r' + x)\rho^{rec}(r')\, d^3r', \rho^{rec} = -\nabla \bullet m^{rec} \tag{3.6}$$

where Φ_{MR} is the magnetic scalar potential of the equivalent MR field in the medium normalized to a unit potential drop from the element to either shield. The $\rho^{rec}(r)$ is the differential of recorded medium magnetization pattern. The E_{MR} is the MR efficiency and $\langle \sin\theta_0 \rangle$ is the averaged magnetization component along the vertical direction in the element at the bias state normalized by M_s.

For longitudinal recording and wide track situation, (3.6) could be further simplified to a 2D formulation:

$$v_{MR}(x,y) = V_0 \int_{-\infty}^{+\infty} dx' \int_{d}^{d+\delta} dy' \Phi(x+x', y') \frac{dm_x(x')}{dx} \quad . \tag{3.7}$$

For a thin media and if it is assumed that the magnetization pattern does not vary with depth into the medium, we could simply evaluate it at the magnetic center of the medium $y = d + \delta/2$, resulting in

$$v_{MR}(x,y) = V_0 \int_{-\infty}^{+\infty} dx' \Phi(x+x', y) \frac{dm_x(x')}{dx} \tag{3.8}$$

$$V_0 = 4JW\Delta\rho E_{MR} \langle \sin\theta_0 \rangle \left[\frac{M_r \delta}{M_s \ t} \right] \tag{3.9}$$

$$F(x) = \frac{1}{2M_r} \frac{\partial m_x}{\partial x} \tag{3.10}$$

where, W is the MR read track width, and $M_r\delta$ is the remnant moment-thickness product for the thin film medium. For a spin valve MR head,

$$V_0 = 4JW\Delta\rho \ E_{SV} \left[\frac{M_r \delta}{M_s \ t} \right]. \tag{3.11}$$

Furthermore, $\Phi(x,y)$ is the potential at a distance y above the surface of the ABS and could be calculated with

$$\Phi(x,y) = \frac{y}{\pi}\int_{-\infty}^{+\infty} \frac{dx'\Phi_s(x')}{[(x-x')^2 + y^2]} \tag{3.12}$$

where $\Phi_s(x)$ is the surface potential. Now, the problem is to get the boundary value solution of Laplace's equation in two dimensions for the potential at the ABS. For the reciprocity potential calculation, the most important feature is how much the potential decays within a gap length of the ABS. If both the shields and the element are assumed to be infinitely permeable, then the element carries a magneto static scalar potential of unity and the shields are fixed at zero potential. The element height is extended to be semi-infinite in the *y* direction. The approximation is made to obtain analytical expression for the surface potential. The geometrical configuration of our calculation is illustrated in Fig 3.4, where the head gap length *g* is the spacing between the shield layer and the sensing layer of the spin-valve head and *t* is the thickness of sensing layer.

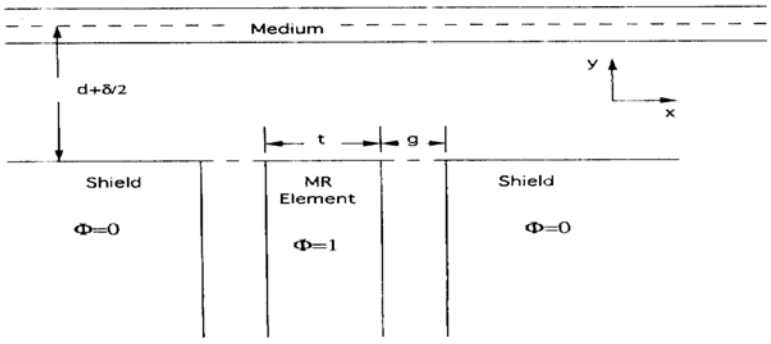

Fig. 3.4 Geometrical configuration of modeling of reading process

3.2.2.2 Surface Potential Model Comparison

Obtaining surface potential involves solving Laplace's equation for complicated boundary geometry, and there have been a few approaches to solve this problem. In our platform, we implemented three models including linear Potter approximation [17] [18], and two nonlinear models, namely, Fourier series method [19] and simplified

conformal mapping method [20] [21], which give more accurate description of the surface potential function. Although some other method like finite element method [17] could give accurate results, it is not easy to implement because of its complexity in numerical calculation. For comparison, the surface potential $\Phi_s(x)$ obtained with the above three methods are illustrated in Fig. 3.5 using the formulas from (3.13) to (3.19), where the value of *t/g* is assumed to be 1/10 in the calculation. The longitudinal component of the surface field calculated with simplified conformal mapping method is illustrated in Figs. 3.6 (a) and (b) with *t/g* assumed as 1/10 and 1/5, respectively.

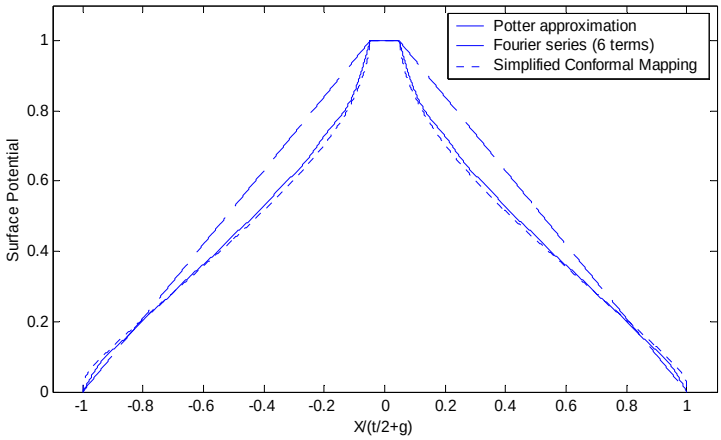

Fig. 3.5 Surface potential $\Phi_s(x)$ with different approaches

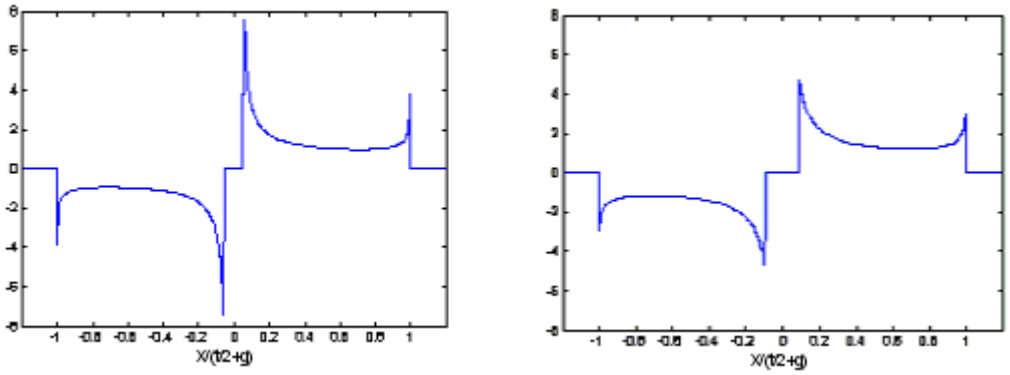

Fig. 3.6 (a) Surface head field with *t/g*=1/10 (b) Surface head field with *t/g*=1/5

Potter approximation assumes that the potential varies linearly across the element-shield gap at the surface. An analytical expression for potential $\Phi(x, y)$ could be obtained from the potter approximation:

$$\Phi(x,y)=\frac{1}{\pi}$$
$$\left\{\begin{array}{l}\tan^{-1}\dfrac{t/2-x}{y}+\tan^{-1}\dfrac{t/2+x}{y}+\dfrac{g+t/2+x}{g}(\tan^{-1}\dfrac{g+t/2+x}{y}-\tan^{-1}\dfrac{t/2+x}{y})\\ +\dfrac{g+t/2-x}{g}(\tan^{-1}\dfrac{g+t/2-x}{y}-\tan^{-1}\dfrac{t/2-x}{y})\\ -\dfrac{y}{2g}\left[\ln\dfrac{(g+t/2-x)^2+y^2}{(t/2-x)^2+y^2}+\ln\dfrac{(g+t/2+x)^2+y^2}{(t/2+x)^2+y^2}\right]\end{array}\right\}. \qquad (3.13)$$

The longitudinal head field can be obtained by

$$h_x(x,y)=-\frac{\partial}{\partial x}\Phi(x,y)\ =\frac{1}{\pi g}\left[\begin{array}{l}\tan^{-1}(\dfrac{g+t/2+x}{y})-\tan^{-1}\dfrac{g+t/2-x}{y})+\\ \tan^{-1}\dfrac{t/2-x}{y}+\tan^{-1}\dfrac{t/2+x}{y}\end{array}\right]. \qquad (3.14)$$

The exact variation of potential across the gap surface could not be obtained in a simple analytical form and is inherently nonlinear. In the simplified conformal mapping analysis, the surface field is approximated by an equally weighted sum of the constant surface field of the Potter approximation and the exact analytical solution obtained using the Schwarz-Christoffel transformation for an infinitesimally thin MR head with finite gaps and MR element thickness and infinite shields. The surface potential of the infinitesimally thin MR head $\Phi^{\inf}{}_s(x)$ is given by

$$\Phi^{\inf}{}_s(x)=1-c\int_a^x\frac{1}{\sqrt{(1-x^2)(x^2-a^2)}}dx,\ a<x<1, \qquad (3.15)$$

$$c=\frac{1}{\int_a^1\frac{1}{\sqrt{(1-x^2)(x^2-a^2)}}dx},\ a=1/(1+2*g/t). \qquad (3.16)$$

The surface potential of the shielded MR head is obtained by superposition:

$$\Phi_s(x)=\frac{\Phi_s^{\inf}(x)}{2}+\frac{(1-x)}{2*(1-a)},a<x<1. \qquad (3.17)$$

Thus, the longitudinal component of the surface field in the gap is

$$h_x^s(x) = -\frac{d\Phi_s(x)}{dx} = \pm\frac{1}{2}\left(\frac{1}{1-a} + \frac{c}{\sqrt{(1-x^2)(x^2-a^2)}}\right) \tag{3.18}$$

‘ + ’ for $a < x < 1$, ‘-‘ for $-1 < x < -a$.

Fourier series method broke the interested geometry into two regions including the gap region and the area above the ABS surface. Then we solve Laplace’s equation with stated boundary conditions at the interface between the two regions to get the coefficients. The surface potential $\Phi_s(x)$ could be expressed accurately with limited numbers of coefficients as

$$\Phi_s(x) = 1 + \frac{t/2 - x}{g} + \sum_{n=1}^{\infty} A_n \sin\left[\frac{2n\pi}{g}\left(x - \frac{t+g}{2}\right)\right] + \sum_{n=1}^{\infty} B_n \cos\left[\frac{2(n-\frac{1}{2})\pi}{g}.\left(x - \frac{t+g}{2}\right)\right] \tag{3.19}$$

where A_n and B_n are coefficients. From Fig. 3.5 it could be seen that the linear Potter potential variation overestimates the magnitude of the potential in the shield-element gaps and is not sufficient to describe some important features of the MR head response. While the potential modeled by the other two methods are almost identical and show the non-linear curvature behavior that leads to the non-linear shape of the corresponding surface longitudinal surface field. The field near the element corners approaches infinity more rapidly than that at the shield corners. Furthermore, as the ratio *t/g* increases, the asymmetry in the head field peaks decreases. This is because as *t/g* increases, the structure becomes more similar to two well separated inductive heads, which have symmetric head field peaks in their respective gaps.

Many of the important features of the MR head response could be understood by

examining the Fourier transform of the magnetic scalar potential and the related surface head field. For comparison, the Fourier transform of the surface head field in potter approximation and Fourier series method are calculated with formulas from (3.20) to (3.22) and are plotted in Fig. 3.8.

$$\left|H_s^{MR}(k)\right| = k\Phi_s^{MR}(k) = \frac{4}{kg}\sin(k(t+g)/2)\sin(kg/2) \tag{3.20}$$

$$\Phi^{MR}{}_s(k) = \frac{\pi g}{2}C\left(\frac{kg}{2}\right), \text{ where } k = \frac{2\pi}{\lambda} \tag{3.21}$$

$$C(\omega) = \frac{2}{\pi}\frac{\sin(\omega)}{\omega^2}\sin\left[\omega\left(\frac{t}{g}+1\right)\right] + \sum_{n=1}^{\infty}A_n\frac{4n(-1)^{n+1}\sin(\omega)\sin\left[\omega\left(\frac{t}{g}+1\right)\right]}{\omega^2-(n\pi)^2} + \sum_{n=1}^{\infty}B_n\frac{4(n-1/2)(-1)^2\cos(\omega)\cos\left[\omega\left(\frac{t}{g}+1\right)\right]}{\omega^2-\left[(n-1/2)\pi\right]^2} \tag{3.22}$$

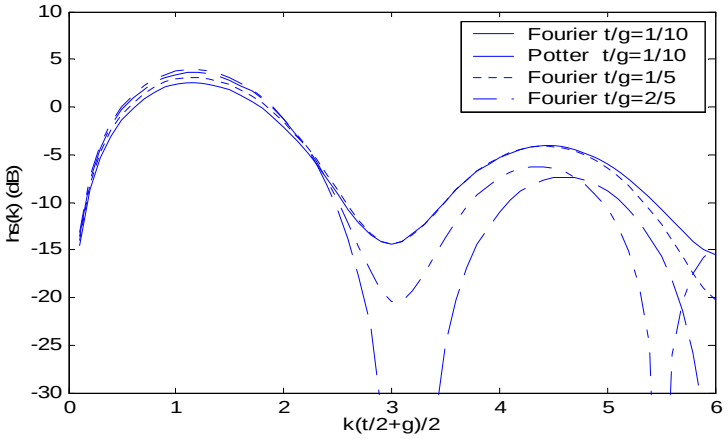

Fig. 3.7 Comparison between Potter and Fourier surface field spectra

As seen in Fig 3.7, with Potter approximation, the surface field is constant in each gap and zero elsewhere. The symmetry of the surface field in the shield-element gaps gives rise to gap nulls in the frequency response at $k(t+g)/2 = n\pi$ and $kg/2 = n\pi$ where n is an integer. But in real systems, these spectral nulls do not occur because the potential variation across the gap is nonlinear and the field is asymmetric. Shape of the

field spectra predicted by Fourier analysis is a strong function of *t/g*. As the *t/g* is as small as 1/10, it is quite different from the Potter approximation solution. With the increase of *t/g*, the depth of the gap minima increases dramatically and finally the minima become nulls. This is because, the head field peaks become more symmetric as the *t/g* increases.

3.2.3 Playback Pulses

The calculation of playback signal and voltage spectra requires only the surface reciprocity potential and the magnetic transition shape. We could evaluate the playback waveform with formula (3.7). From (3.9) we could see that the signal voltage is directly proportional to the current density, read track width, magneto-resistance change and is also scaled by the ratio of the $M_r\delta$ of the medium to the $M_s t$ of the MR layer. Here we are more interested in normalized voltage without consider the V_0 since the harmonic ratio will be used for the characterization and this ratio will not be affected by V_0. With selection of surface potential model and transition shape model, and input related parameters include d, δ, g t and a, the reciprocity signal voltage could be calculated.

Playback signal pulse calculated with different transition functions and surface potential models described before are compared. Fig. 3.8 plots the isolated playback pulses for the three transition distributions in Table 3.1; the Fourier series model is used for surface potential. In Fig. 3.9, playback pulses with three surface potential models and tanh transition model are plotted. The parameters in the calculation include $g = 50\,\text{nm}$, $t/g = 1/10$, $d = 10\,\text{nm}$, $\delta = 10\,\text{nm}$ and transition parameter $a = 12\,\text{nm}$.

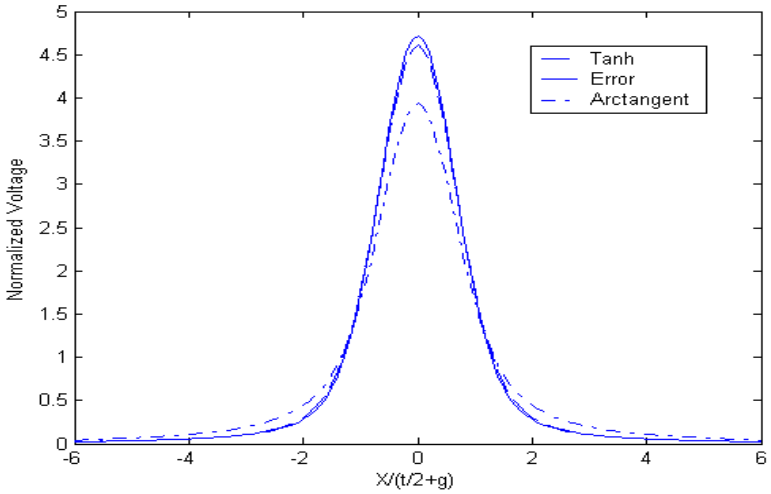

Fig. 3.8 Voltage pulse with different transition models, showing that tanh and error function models give similar amplitude.

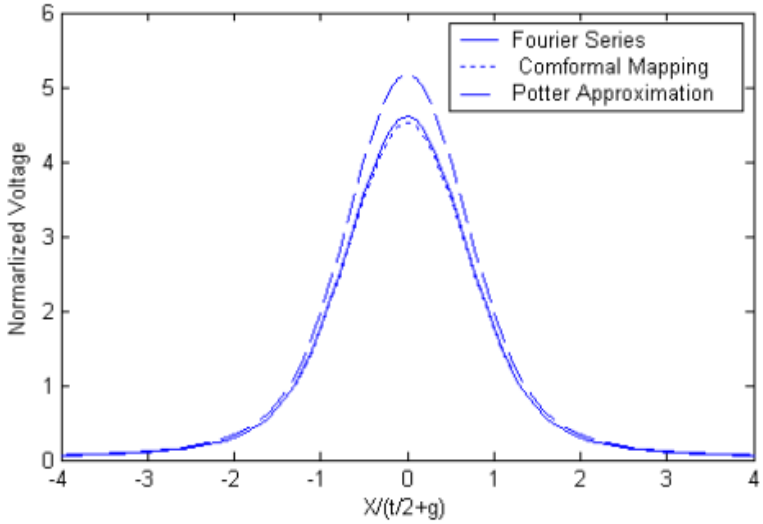

Fig. 3.9 Voltage pulse with different surface potential models

It could be seen that the playback pulses from the hyperbolic tangent model and error function transition model exhibit higher amplitude at the center of the transition. Moreover, they have sharper gradients at the pulse tails than for the arctangent transition. As expected, the Fourier series model and the simplified conformal mapping method produce nearly same pulse shape and the Potter peak voltage is higher than the ones with the other two models. The reason for this is the difference in the surface potentials shown in Fig. 3.5, the surface potential obtained with Potter

approximation has a bigger magnitude than the other models.

We are interested in the effect of head-disk interface parameters on the shape of the playback waveform. In reality, the transition parameter a varies with the fly-height. A good description for the variation of the transition parameter with flying height is the one given in the Williams-Comstock write model [12] and for high moment media in (3.4). In (3.4), Q is related to the head field gradient and I is related to the transition shape. They are dimensionless numbers and are typically given by $Q = 0.82$ and $I = 0.69$ for a tanh transition model. Medium parameters given by $H_c = 4150$ Oe and $M_r\delta =$ 0.37 memu/cm^2 in CGS units must be converted to MKS before using in (3.4). Voltage pulses were generated for different magnetic spacing d with corresponding transition parameters and are plotted in Fig. 3.10. Gap length g is 50 and t/g is fixed at 1/10 in the calculation with simplified conformal mapping potential and the tanh transition model selected.

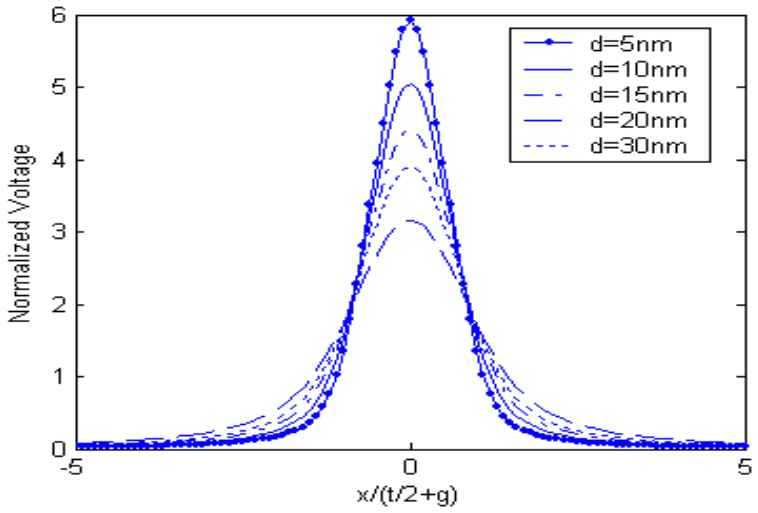

Fig. 3.10 Voltage Pulse with different magnetic spacing d

From Fig. 3.10, we could see that as the magnetic spacing increases, the amplitude of the pulse drops and the pulse broadens. The peaks are more triangular at lower

magnetic spacing because the triangular surface potential plays a more dominant role in the voltage shape in this regime. As the media is far from the ABS, the features of the surface potential become less important and the peaks are more rounded. The role of the shields in determining the linear density is quite clear that the pulse is confined in a range not much larger than the shield-to-shield spacing. The linear resolution for the playback process could be well tuned by adjusting the shield gap. As it is assumed that the magnetization pattern does not vary with depth into the medium, the pulse shapes generated with (3.7) and (3.8) are almost identical, we could simply evaluate it at the magnetic center of the medium $y = d + \delta/2$. Study shows that the increase of media thickness leads to the same effect such as pulse broadening as increase of magnetic spacing since the media is far from the ABS.

3.3 Playback with Multiple Transitions

Based on the assumption that the playback process of isolated magnetic transitions is linear, it is valid to predict that the playback signal from a sequence of transitions is given by the sum of individual output responses. This is known as the principle of linear superposition:

$$v(x) = \sum_n (-1)^n v_{sp}(x - x_n) \tag{3.23}$$

where v_{sp} is the playback isolated transition response discussed in Section 3.2 and x_n is the location of the n th transition written in the sequence. Linear superposition is valid as long as the distance between adjacent reversals does not become smaller than the width of the magnetization transition and also requires that the individual transitions be identical. In square wave recording which refers to a series of transitions

with alternating polarity and a fixed bit spacing B, the playback signal can be written in terms of the voltage from a single transition as

$$v(x) = \sum_{n=-\infty}^{\infty} (-1)^n v_{sp}(x - nB) \ , \ B = \frac{\lambda}{2}. \tag{3.24}$$

A parameter named channel density D_c is defined as the ratio of PW_{50} to the physical bit length B. With the isolated pulse in Fig. 3.10 with $d = 10nm$, we plotted the playback signal with multiple transitions for $B = 400$ nm and D_c=0.21 in Fig. 3.11, and with $B = 120$ nm in Fig. 3.12.

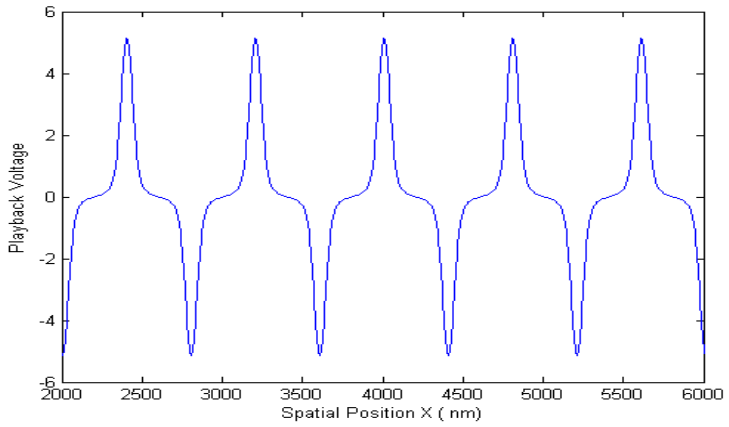

Fig. 3.11 Square wave recording playback signal with B=400nm

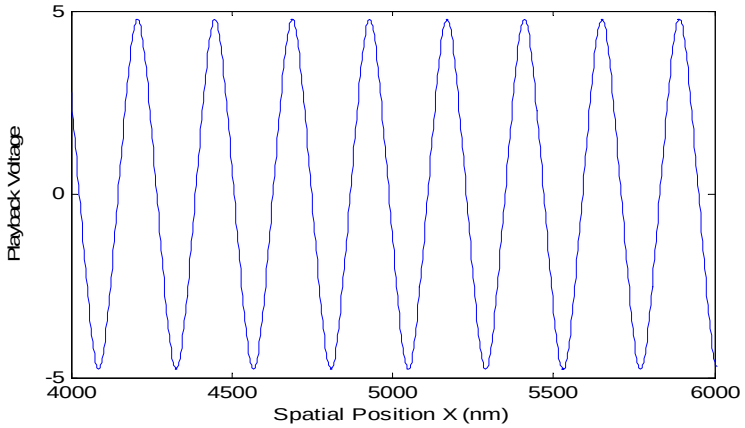

Fig. 3.12 Square wave recording playback signal with B=120nm

At low densities, the replay pulses are isolated and do not overlap as shown in Fig. 3.11. With reduced spacing between transitions, the isolated replay pulses begin to

interfere destructively causing a reduction in overall replay signal amplitude as indicated for the case in Fig. 3.12 where the resulting signal resembles a sinusoidal waveform. An important parameter in characterizing the head and medium performance in a recording system is the peak amplitude signal as a function of linear density. This indicates the persistence of signal with reduced transition spacing before reaching the system's noise floor. This is known as the 'roll-off' curve.

For a fixed gap length $g = 35nm$, fixed MR element thickness $t = 5nm$, media thickness $\delta = 10nm$, transition parameter is calculated with (3.4) for each magnetic spacing where $H_c = 4150Oe$ and $M_r\delta = 0.37memu/cm^2$. Readback pulse for different values of magnetic spacing is calculated with conformal mapping potential model and tanh transition model. The resulting peak replay voltage normalized to the peak replay voltage of an isolated pulse is plotted as a function of linear density in Fig. 3.13. Linear density is defined as the reciprocal of the bit-spacing, *1/B*. The linear density is expressed in terms of the number of Flux Changes (reversals) per Inch (FCI) along the medium.

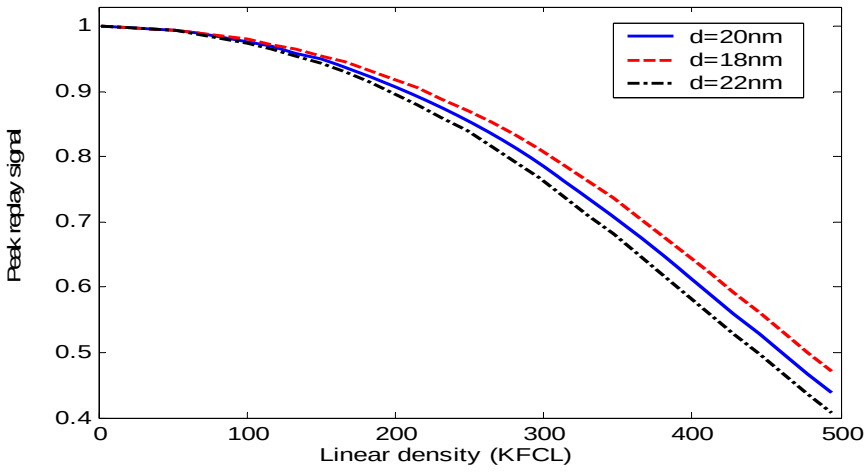

Fig. 3.13 Roll off curves of different magnetic spacing

It can be seen that the peak replay signal decreases monotonically with recording density. Furthermore, the reduction in the value of effective magnetic spacing reduces the slope of the roll-off curve, hence improving the signal amplitude at short recording wavelengths.

Investigations suggest that the replay head gap length limits the maximum achievable packing density, and increased gap width will degrade the data retrieval resolution of the reading head at high bit density [22]. With a fixed magnetic spacing $d = 20\,\text{nm}$ and all the other parameters same as before, the variation of gap length effect on roll off curve is plotted in Fig. 3.14.

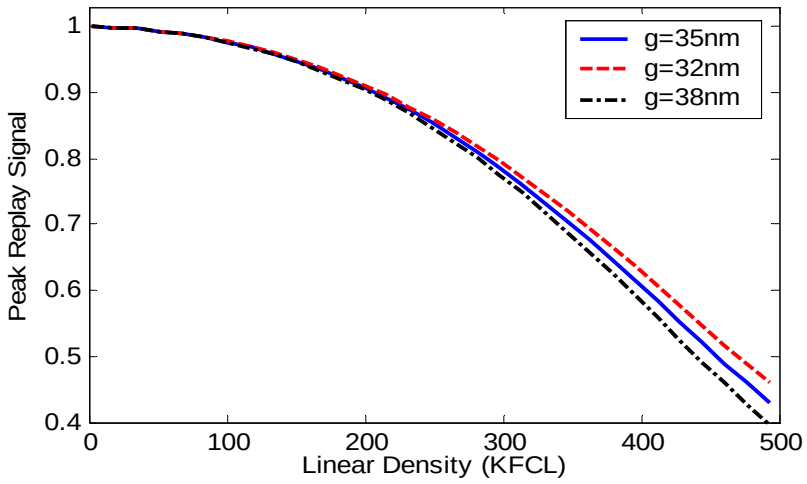

Fig. 3.14 Roll off curves of different gap length

It is seen that with the same magnetic spacing, the falling rate of the roll-off curve will be smaller with narrower gap length at high densities.

In triple harmonic method, infinite series of "111100" is written onto the disk. With linear superposition of isolated pulses in Fig. 3.10, multiple transition response is plotted in Fig. 3.15 with B=60nm and D_c=1.4:

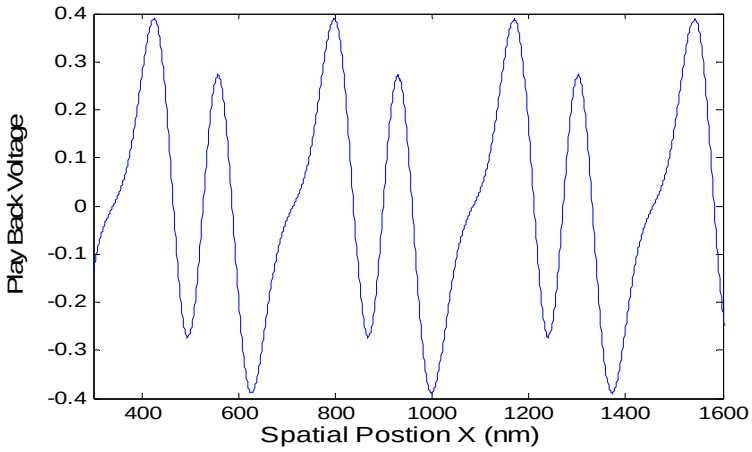

Fig. 3.15 111100-code playback signals

The waveform obtained from this modeling platform agrees well with the experimental waveform, as can be seen in Chapter 4.

3.4 Spectral Analysis

3.4.1 Isolated Pulse Frequency Response

In magnetic recording, many of the important issues such as power spectral densities of signal and noise are of interest and are easier to study in frequency domain. Spatial Fourier transform of the playback signal $v(x, y)$ is taken to obtain the frequency response. The integral with respect to x over infinity in the playback signal expression (3.8) is a correlation integral. Correlation in the spatial domain is equivalent in the frequency domain to a multiplication of the complex conjugate of the Fourier transform of the potential function with the Fourier transform of the magnetization gradient [22]. For uniform magnetization throughout the depth of the medium, the Fourier transform of the horizontal playback signal in (3.8) is thus

$$V_{MR}(k) = V_0(jkM_x(k)) \int_{y=d}^{y=d+\delta} \Phi^*(k, y)dy\,,\ k = \frac{2\pi}{\lambda}\,. \tag{3.25}$$

For an even head sensitivity function, the infinite integral over x in this particular case can either be treated as a correlation or a convolution integral without distinction since $\Phi_s^*(k) = \Phi_s(k) = H_s(k)/(jk)$ and it could be written in terms of surface head sensitivity transforms times the spacing loss term:

$$\Phi\ (k, y) = \Phi_s\ (k) e^{-|k|y} = H_s(k) e^{-|k|y}\ /(jk)\,. \tag{3.26}$$

Substituting (3.26) into (3.25) and integrating with respect to y over the magnetic medium thickness yields

$$V_{MR}(k) = V_0\ F\ (k).[H_s(k)].\left[e^{-|k|d}\right].\left[\frac{1-e^{-|k|\delta}}{k\delta}\right] \tag{3.27}$$

$$F(k) = \frac{jk}{2M_r} M(k)\,. \tag{3.28}$$

There are three terms in square brackets in (3.27). The first term is the gap loss function. For a constant field distribution along the surface of gap (Karlqvist head), the gap loss can be approximated by the Sinc function $\frac{\sin(kg)}{(kg)}$. For MR head under Potter approximation $H_s(k)$ is defined in (3.20). The second term is the spacing loss term that is first found and quantified by Wallace (1951) [18], and reflects the decrease of signal amplitude with increasing distance between the ABS and the media. The final term is the thickness loss term. At long wavelengths, expanding the exponential to first order in which case the thickness loss term approaches unity, and the reproduced voltage frequency response will be scaled by the medium thickness can approximate this term. At short wavelengths, on the other hand, when $\lambda << \delta$, the exponential term reduces to zero and the playback response effectively becomes flat with wavelength and independent of the medium thickness.

Substituting $M_x(k)$ of the transitions listed in Table 3.1 and the above loss factors into (3.27) produces the playback spectra of an isolated playback pulse in terms of the wave number k as

$$\left|\frac{V(k)}{V_0}\right|_{\text{arctan}} = \left[\frac{4}{k^2 g}\sin\left(\frac{k(t+g)}{2}\right)\sin(kg/2)\right]\left[1-e^{-k\delta}\right]e^{-k(d+a)} \tag{3.29}$$

$$\left|\frac{V(k)}{V_0}\right|_{\text{tanh}} = \frac{\pi^2 a e^{-kd}}{\sinh(\pi^2 ak/4)}\left[\sin\left(\frac{k(t+g)}{2}\right)\frac{\sin(kg/2)}{kg}\right]\left[1-e^{-k\delta}\right] \tag{3.30}$$

$$\left|\frac{V(k)}{V_0}\right|_{error} = e^{-\frac{\pi k^2 a^2}{4}}\left[\frac{4}{k^2 g}\sin\left(\frac{k(t+g)}{2}\right)\sin(kg/2)\right]\left[1-e^{-k\delta}\right]e^{-kd} \ . \tag{3.31}$$

The advantage of using an arctangent transition from a calculation standpoint becomes clear by examining (3.29). The exponential term due to the arctangent magnetization transition e^{-ka} is known as the medium loss term. Loss of signal in this case is interpreted to be due to the departure from the ideal step change in magnetization with zero transition width parameter due to the magnetic medium's hysteresis characteristics. The voltage obtained from a finite width arctangent transition is the same as that obtained from a perfectly sharp transition at a net effective spacing $d_{eff} = d + a$. It is much easier to calculate the response from a step transition rather than performing a correlation, so this feature is very convenient for analytical calculation.

3.4.2 Harmonic Ratio Methods and Spectrum Comparison

As mentioned before, one harmonic ratio method uses all "1" data pattern (square wave recording) and the other uses "111100" data pattern (triple harmonic method). The harmonic signal and signal spectrum of those two methods are compared by the

modeling platform described before.

3.4.2.1 Square Wave Recording

The Fourier transform of a given sequence as in (3.23) is simply

$$V(k) = V_{sp}(k)\sum_{n}(-1)^n e^{ikx_n}. \tag{3.32}$$

where x_n is the location of the n th transition written in the sequence. For square wave recording, the Fourier transform of (3.27) can be written in terms of the Dirac Delta function as

$$V(k) = 2k_0 V_{sp}(k)\sum_{m=-\infty}^{\infty}\delta(k-(2m+1)k_0) \tag{3.33}$$

where k_0 is the fundamental wave number and is defined by $k_0 = \pi / B$. Therefore, the Fourier transform of an infinite series of alternating playback pulse is an infinite sequence of odd harmonic impulses whose amplitude is weighted by $2k_0$ times the Fourier transform of the isolated playback pulse. Practical spectral measurements involve a spectrum analyzer that gives the spectral power or RMS voltage content of the input signal within a frequency bandwidth. Taking the square root of the average power of (3.33) yields

$$V_{rms}(k = mk_0) = \frac{2k_0}{\sqrt{2\pi}}\left|V_{sp}(k)\right|, \;\; m = 1,3,5,7\ldots. \tag{3.34}$$

Substituting (3.27) into (3.34) yields

$$V_{rms}(k = mk_0) = \frac{2V_0}{\sqrt{2\pi m}}\left|F(mk_0)\right|.(1-e^{-mk_0\delta})\left|H_s(mk_0)\right|e^{-mk_0 d}. \tag{3.35}$$

Note that the harmonics are weighted by spectral components of the head field, the transition shape, spacing loss, and a term dependent on the medium thickness from $m = 1,3,5,\ldots$.

Consider square wave recording over a wide range of recording density, the fundamental component is measured at each frequency and plotted as an envelope versus recording frequency; such a plot is referred to as the 'spectrum'. Substituting (3.27) to (3.31) in (3.35), with gap length $g = 35nm$, MR element thickness $t = 5nm$, media thickness $\delta = 10nm$, transition parameter $a = 12nm$, magnetic spacing $d = 20nm$, radius $r = 1.256inch$, and velocity $RPM = 7200$, the spectrum with different transition models are plotted in Fig. 3.16.

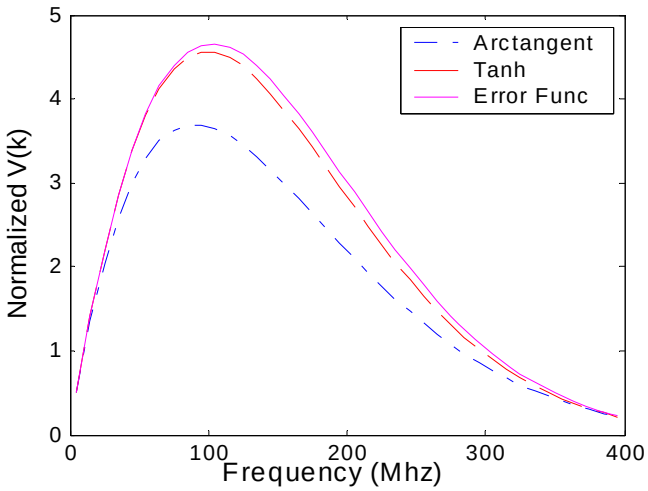

Fig. 3.16 Square wave spectrum of the fundamental component with different transition models

The spectra with arctangent and tanh model are quite similar, while the result with the arctangent model has smaller magnitude. The smaller magnitude with arctangent corresponds to smaller amplitude of the isolated pulse as seen in Fig. 3.8. Since the spectrum of arctangent model and the other two models differs obviously within the experimental testing range, the calculation results based on different transition models will affect the accuracy of testing method in practical study; arctangent model may not be a good choice.

In computer simulation, Fast Fourier transform (FFT) is often used to do frequency

analysis of discrete signals. It is a discrete Fourier transform algorithm that effectively reduces the number of computations. Isolated pulse in Fig. 3.10 with $d = 10nm$ is duplicated multiple times before FFT, and the resulted $V(k)$ are plotted in Fig. 3.17, with D_c=0.23.

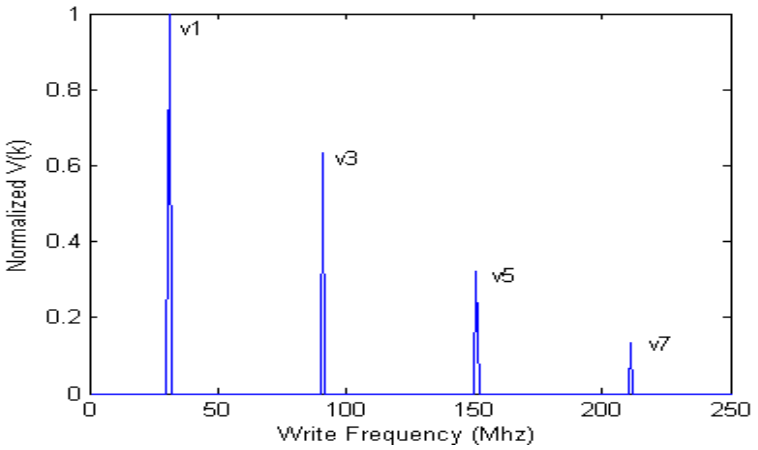

Fig. 3.17 Square Wave voltage spectrums

As expected there are only odd harmonic components at multiples of k_0. At each harmonic the amplitude is proportional to $V_{sp}(k)$ as in (3.34). The write frequency f relates to spacing B as

$$f = \frac{ve}{2B} = \frac{vk_0}{2\pi} \tag{3.36}$$

where ve is the rotating velocity of the disk.

3.4.2.2 Triple Harmonic Pattern Recording

In triple harmonic method, infinite series of "111100" is written onto the disk. The Fourier transform of the playback signal relates to isolated pulse voltage as

$$V_{pattern}(k) = V_{sp}(k)(1 - e^{ikB} + e^{2ikB} - e^{3ikB} + e^{4ikB}) \sum_{n=-\infty}^{\infty} e^{ik6nB} . \tag{3.37}$$

Since delta functions posses the property as

$$\delta(ax) = \frac{\delta(x)}{|a|} \quad , \tag{3.38}$$

from (3.33), (3.37) can be written in terms of the Dirac Delta function as

$$V_{pattern}(k) = \frac{(1 - e^{ikB} + e^{-2ikB} - e^{-3ikB})}{3} k_0 V_{sp}(k) \sum_{m=-\infty}^{\infty} \delta(k - \frac{mk_0}{3}) \tag{3.39}$$

where k_0 is the fundamental wave number and is defined by $k_0 = \pi / B$ .From (3.39) we could see that Fourier transform of triple harmonic method pattern will include both odd harmonics and even harmonics.

Here we consider one period waveform voltage of "111100" written at a spacing of $B_{0:}$

$$V(k) = V_{sp}(k)(1 - e^{-ikB_0} + e^{-2ikB_0} - e^{-3ikB_0}) \tag{3.40}$$

$$k_1 = \frac{2\pi}{\lambda_1} = \frac{2\pi}{6B_0} = \frac{\pi}{3B_0}, \; k_3 = \frac{2\pi}{\lambda_3} = \frac{2\pi}{2B_0} = \frac{\pi}{B_0} = \mathrm{k}_0 \tag{3.41}$$

Since

$$V(k_1) = V_{sp}(k_1) = V_{sp}(k_1)(1 - e^{-i\frac{\pi}{3}} + e^{-i\frac{2\pi}{3}} - e^{-i\pi}) \tag{3.42}$$

$$V(k_3) = V_{sp}(k_3)(1 - e^{-i\pi} + e^{-2i\pi} - e^{-3i\pi}) = 4V_{sp}(k_3) \quad , \tag{3.43}$$

the 1st harmonic and 3rd harmonic intensity of pattern "111100" can be derived as

$$V_{pattern}(k_1) = \frac{1}{3} k_3 V_{sp}(k_1), \qquad V_{pattern}(k_3) = \frac{4}{3} k_3 V_{sp}(k_3) \tag{3.44}$$

Frequency domain results of Fig. 3.15 are plotted in Fig 3.18.

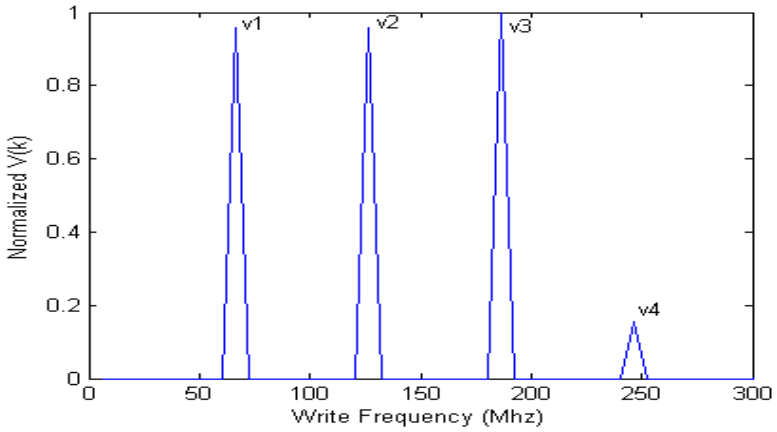

Fig. 3.18 spectrum of readback signal of "111100" pattern

In Fig. 3.18, only the first four harmonics are plotted since the higher harmonics are small enough to be ignored. We could see that in triple harmonic method, the signal energy is concentrated in the first three harmonics and the amplitude of them are strong and comparable at the high channel density 1.4, while the signal energy is linearly distributed to all of the odd harmonics in the square wave recording and the amplitude of the 3^{rd} harmonic is significantly smaller compared to the 1^{rd} harmonic even at the low channel density 0.2.

3.4.2.3 Energy Distribution of Harmonics

Conventional square wave harmonic method and triple harmonic method calculate the ratio of 3rd harmonic amplitude and 1st harmonic amplitude of readback signal for fly-height measurement. With the variation of the bit spacing, the energy of the harmonics re-distributes. The higher the intensity of the harmonics is, the higher the measurement precision will be. We could calculate the intensity of harmonics at various recording densities. The three main harmonic intensities of the two methods at different channel densities are plotted in Fig. 3.19 and Fig. 3.20. The intensities are all normalized with the peak value of the 1st harmonic in square wave recording.

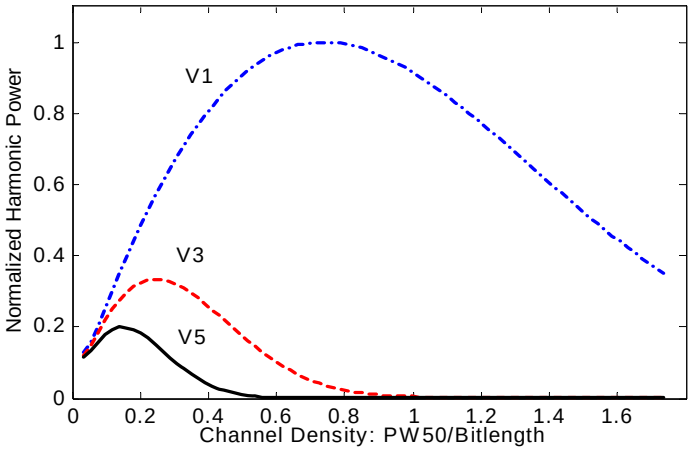

Fig. 3.19 Normalized Harmonic Power of the conventional square wave recording

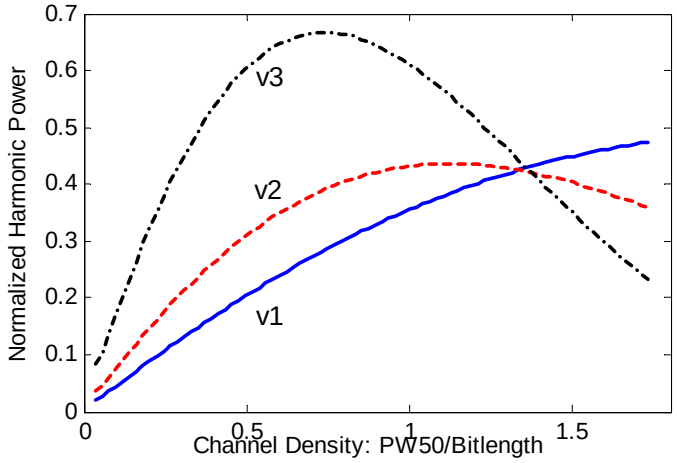

Fig. 3.20 Power Spectrum of the triple harmonic method

It could be seen although 1st harmonic of the square wave recording has higher amplitude than that of triple harmonic method, the amplitudes of its higher harmonics decrease fast and makes this method valid only at low channel density. But in triple harmonic method, the three harmonic intensities are high and comparable when the channel density is high. This is a significant advantage for in-situ fly-height measurement since the fly-height sensitivity is proportional to the channel density. In general, the best testing range of the channel density for the fly-height measurement in the harmonic based methods are the regions where the tested harmonics are of comparable power strength. This is because the SNR is proportional to the harmonic

intensity, and hence higher SNR means higher tolerance to the measurement-induced error ΔV . Detailed discussion will be in Chapter 4.

3.5 Summary

A platform is developed for studying the readback signal based head-disk system characterization methods with flexibility of theoretical model selection and parameters setup. The critical head-disk system parameters' effect on head disk system performance has been studied both in time and frequency domains.

Chapter 4
In-Depth Analysis of Harmonic Ratio Based Fly-Height Measurement Methods

Harmonic Ratio based fly-height method is the best in-situ solution so far to measure fly-height fluctuations and characterize the lubricant related issues in high-density recording systems. In this chapter, evaluations of harmonic ratio based fly-height measurement methods are done based on testing sensitivity and accuracy. An approach to achieve both high testing sensitivity and accuracy is proposed.

4.1 Measurement Sensitivity

Real time in-situ fly-height measurement is realized by having two band pass filters to obtain the real time variation of the targeted two harmonic signals. Simulation is done to study the sensitivity of harmonic intensity to the fly-height change at different densities. The harmonic intensities of read back signal are calculated with Fourier series based model [18] of shielded MR head and Tanh transition model. It can be seen from Fig. 4.1 that the readback signal harmonic intensity is very sensitive to fly-height variations at high channel density, and the higher harmonic V_3 is more sensitive than the lower harmonic V_1.

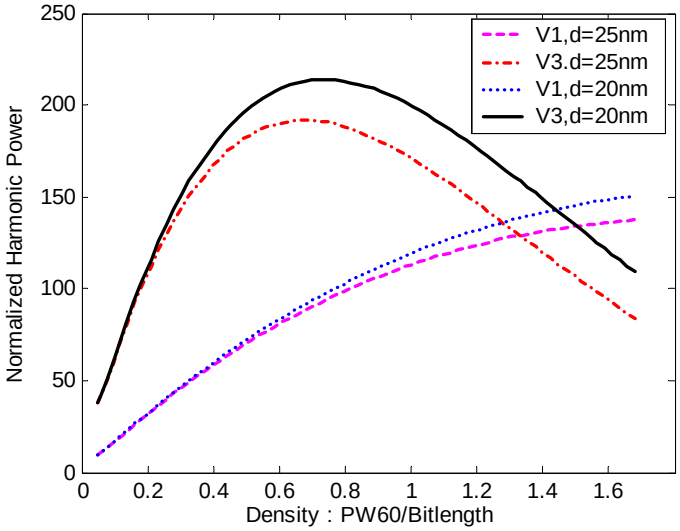

Fig. 4.1 Harmonic intensity at different channel density

From Wallace equation and Eq. (2.15), we know that for a given head, the relationship of relative fly-height variation ΔFH and tested harmonic ratios of the first three harmonics are as below:

$$\Delta FH = -\frac{3\lambda}{4\pi}\left[\ln\left(\frac{V_3}{V_1}\right) - \ln\left(\frac{V_{30}}{V_{10}}\right)\right] \tag{4.1}$$

$$\Delta FH = -\frac{3\lambda_3}{4\pi}\Delta\ln(\frac{V_3}{V_1}) = -\frac{3\lambda_3}{2\pi}\Delta\ln(\frac{V_2}{V_1}) = -\frac{3\lambda_3}{2\pi}\Delta\ln(\frac{V_3}{V_2}) \tag{4.2}$$

where V_{10} and V_{30} are the amplitude of the first and third harmonic of the reference position, respectively.

We define sensitivity function S as the ratio of ΔFH to the harmonic ratios:

$$S_{ab} = \Delta FH / \Delta\ln(\frac{V_a}{V_b}) \tag{4.3}$$

where a and b represent the harmonics selected for the harmonic ratio analysis. Then the testing sensitivity function S of the three harmonic ratios is as below:

$$S_{31} = \frac{4\pi}{3\lambda_3}, S_{21} = S_{32} = \frac{2\pi}{3\lambda_3}. \quad (4.4)$$

From Eq. (4.4) we could know that testing sensitivity of harmonic ratio based triple harmonic fly-height measurement method is proportional to testing density. Furthermore, in the preferred testing range, its signal is concentrated on 1st, 2nd and 3rd harmonics mainly. Among the combination of the three main harmonics, the first and third harmonic ratio has the highest sensitivity.

4.2 Measurement Precision

Another important performance indicator is the measurement precision. In real work, there always exists measurement-induced error ΔV. Take into consideration the ΔV, the testing precision is determined by the harmonic intensity, because the SNR is proportional to the harmonic intensity. The higher the intensity is, the higher the tolerance to the possible measurement error ΔV could be. Since the fly-height calculation is based on the ratio of two harmonics, the harmonic with the lower intensity at the chosen density will play more important role in determining the testing precision. In general, the best testing range of the channel density for the fly-height measurement in the harmonic based methods are the regions where the tested harmonics are of comparable power strength. But in triple harmonic method, the three harmonic intensities are high and comparable at high channel density, which makes it advantageous over the conventional square wave recording based method.

4.2.1 Repeatability Function

Triple harmonic method is based on 111100 pattern. Normally, the harmonic ratio between the 3rd and 1st harmonics is used to derive flying height information:

$$\ln(\frac{V_3}{V_1}) = -\frac{4\pi}{3\lambda_3} d + \ln C(g, \delta, t, \lambda, a) \tag{4.5}$$

where d is the magnetic spacing, and C is a function determined by the recording wavelength λ, head parameters such as gap length g and MR element thickness t, and medium magnetic layer thickness δ, and transition parameter a.

The magnetic spacing could be estimated with

$$d = -\frac{3\lambda_3}{4\pi}(\ln(\frac{V_3}{V_1}) - \ln C(g, \delta, t, a, \lambda)). \tag{4.6}$$

Eq. (4.6) describes the relationship between fly-height and system parameters. There are two possible sources which may affect the testing repeatability: variation of system parameters which can affect $\ln C$, and noise during measurement which may affect the repeatability of $\ln(\frac{V_3}{V_1})$. Since properties of these two sources may also vary with testing density, we may have to compromise testing sensitivity with testing precision when choosing testing density, and the details are discussed in the following part.

4.2.2 Effect of Variation of System Parameters on Fly-Height Measurement

4.2.2.1 Media Thickness Effect

From Eq. (4.6), head and medium parameters g, T and δ influence fly-height measurement results. For the same head, the read transducer gap length g and read element T are constants, but there may exist variation of magnetic layer thickness δ over different parts of disk surface, and also the mean magnetic layer thickness of different disks may vary.

The nominal shield-to shield length is assumed as 75 nm which including 3nm thick free layer. The magnetic spacing d and transition length a are assumed to be 21 nm and 12 nm, respectively. The selection of these parameter values is based on the actual head-media parameters as will be discussed later. The readback signal is calculated with Fourier series based model of shielded MR head and tanh transition model.

Fig. 4.2 shows that 5% variation of magnetic layer thickness, which is 1nm here, induces no more than 0.5nm fly-height variation, which is less than 3% of the magnetic spacing. Compared to other sources induced measurement repeatability concerns, this variation is still within the acceptable range. And another finding is that the media variation induced fly-height error is almost a constant within our testing density.

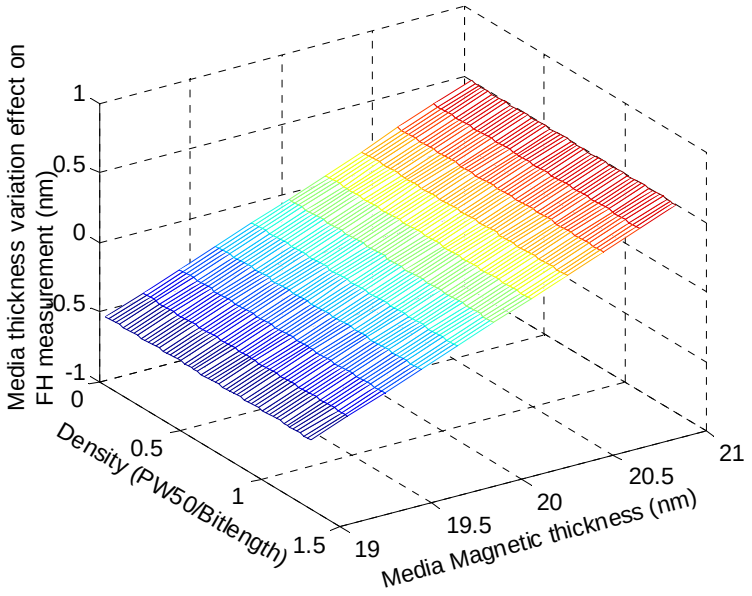

Fig. 4.2 Media thickness effect on fly-height measurement.
(5% Media thickness change only leads to 3% variation of magnetic spacing)

Experiment is done to study the media thickness effect on fly-height measurement. Testing is done on spinstand with same test head flying over ten different pieces of disks of same design. The tested PW50 and harmonic ratio of triple harmonic patterns are illustrated in Table 4.1, the fly-height is calculated with $-\frac{3\lambda_3}{4\pi}\ln(\frac{V_3}{V_1})$. The nominal media magnetic thickness of these disks is around 20nm, and the testing radius and RPM are 1.1054inch and 15000r/min, respectively. Two recording densities 1.32 and 0.66 are considered.

Disk#	PW_{50} (nm)	$\ln(\frac{V_3}{V_1})$ (600Mflux/s)	ΔFH (nm) (600Mflux/s)	$\ln(\frac{V_3}{V_1})$ (300Mflux/s)	ΔFH (nm) (300Mflux/s)
1	96.837	0.049	0.000	0.930	0.000
2	95.339	0.018	-0.108	0.986	0.397
3	94.180	-0.057	-0.373	0.971	0.291
4	93.678	-0.070	-0.419	0.963	0.233
5	95.099	0.018	-0.109	0.952	0.154
6	95.105	-0.083	-0.465	0.936	0.042
7	96.093	-0.083	-0.463	0.938	0.056
8	94.075	0.037	-0.041	0.950	0.142
9	94.592	0.031	-0.064	0.917	-0.088
10	94.341	-0.083	-0.463	0.958	0.201
FH variation	(nm)		0.465		0.485

Table 4.1 Effect of media thickness variation on fly-height measurement

Here, ΔFH is the fly-height reading difference tested over different disks. The disk #1 is used as the reference.

The result in Table 4.1 is reasonable compared to theoretical study. The maximum fly-height variations tested with these ten disks are quite close at the two recording densities, and the value is close to 0.5 nm. But the variation here may not only due to the media magnetic thickness difference, but also due to the media overcoat thickness difference since magnetic spacing is considered here.

4.2.2.2 Gap Length Effect

Reader gap length *g* and read element thickness *t* will not affect the measurement of the fly-height fluctuation since they are constants for a given head. However, the exact value of gap length becomes important if one wants to estimate the absolute fly-height

with deduction of $\ln C$ from $\ln(\frac{V_3}{V_1})$ in Equation (4.6), or wants to estimate fly-height difference among different heads.

Fig. 4.3 shows the fly-height variation caused by the variation of gap length. The readback signal is calculated with Potter's approximation model of shielded MR head and tanh transition model. All the parameters are same as that in Section 4.2.2.1 except gap length variation is considered here. It can be seen that an increased gap length leads to an overestimated fly-height and a decreased gap length leads to an underestimated fly-height. Furthermore, the higher the channel density used for fly-height measurement, the larger will be the variation caused by gap length variation.

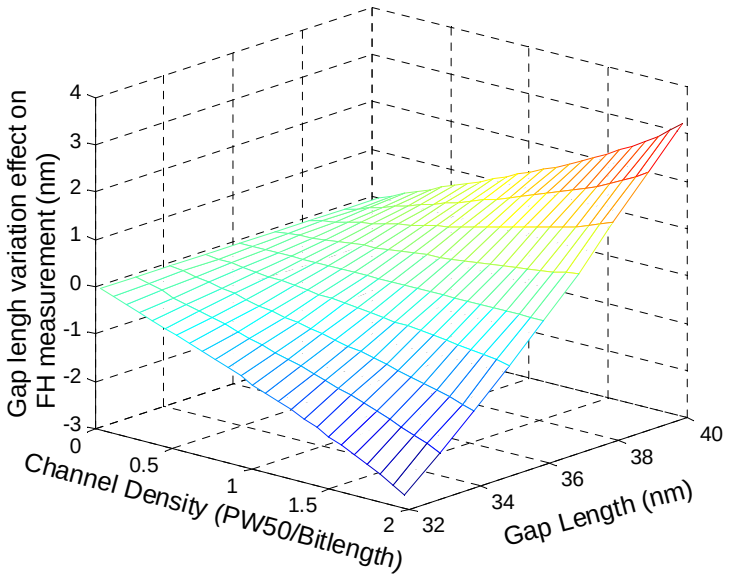

Fig. 4.3 Gap length variation effect on fly-height measurement

4.2.3 Effect of Noise on Fly-Height Measurement

In addition to the effect of system parameters effect on the fly-height measurement, the possible testing accuracy of harmonic intensities can also affect the testing

repeatability of the in-situ fly-height measurement. The general variation analysis function is as below:

$$\Delta F\ (x,y,z) = \left|\frac{\partial F}{\partial x}dx\right| + \left|\frac{\partial F}{\partial y}dy\right| + \left|\frac{\partial F}{\partial z}dz\right| \tag{4.7}$$

where ΔF is the variation of function F caused by the variation of x, y and z, respectively.

From Eqs. (4.6) and (4.7), the relationship between the fly-height variation ΔFH of different harmonic ratio combinations and the harmonic amplitude variation ΔV, induced by noise and voltage testing resolution in the experiment, are as below:

$$\begin{aligned}
\Delta FH_{31} &= \left|\Delta V_3 * \frac{\partial FH}{\partial V_3}\right| + \left|\Delta V_1 * \frac{\partial FH}{\partial V_1}\right| = \frac{3\lambda_3}{4\pi}\left(\left|\frac{\Delta V_3}{V_3}\right| + \left|\frac{\Delta V_1}{V_1}\right|\right) \\
\Delta FH_{21} &= \left|\Delta V_2 * \frac{\partial FH}{\partial V_2}\right| + \left|\Delta V_1 * \frac{\partial FH}{\partial V_1}\right| = \frac{3\lambda_3}{2\pi}\left(\left|\frac{\Delta V_2}{V_2}\right| + \left|\frac{\Delta V_1}{V_1}\right|\right) \\
\Delta FH_{32} &= \left|\Delta V_3 * \frac{\partial FH}{\partial V_3}\right| + \left|\Delta V_2 * \frac{\partial FH}{\partial V_2}\right| = \frac{3\lambda_3}{2\pi}\left(\left|\frac{\Delta V_3}{V_3}\right| + \left|\frac{\Delta V_2}{V_2}\right|\right)
\end{aligned} \tag{4.8}$$

It can be seen from (4.8) that the variation of the fly-height measurement is also correlated to transition wavelength (λ) and the amplitude of harmonic intensity (V_1, V_2, V_3). Shorter wavelength and higher harmonic intensity will contribute to smaller variation of fly-height measured and, therefore, better repeatability of flying height testing data. In other words, investigation should be done on choosing suitable transition wavelength or recording density to achieve high sensitivity of testing method as well as to minimize the variation of fly-height test readings. Furthermore, if we assume similar ΔV for different harmonics, then we see that ΔFH_{31} is much smaller compared to ΔFH_{21} and ΔFH_{32}.

4.2.3.1 Peak Detection and Testing Accuracy

One advantage of triple harmonic method is that it can be used to evaluate the dynamic response of fly-height under various working and slider-disk interaction conditions. One possible approach for achieving the highest possible dynamic response is to use peak detection to detect the peak amplitude of each harmonic channel.

In this case, the noise in the readback signal will include channel/electronics noise and media noise. The powers of channel and electronics noises are normally fixed values. The dominant type of media noise in high coercivity thin film media is known to be the transition noise. The power of transition noise becomes larger when bit density is high, as the reading head will read more transitions per each unit of reading time [13].

Simulation work is done based on Eq. (4.8). As a first approximation and for the convenience of analysis, we assume the harmonic power variation ΔV is due to channel noise and transition noise. In Figs. 4.4 and 4.5, the harmonic power V_3 and V_1 at different densities are calculated as that in Section 3.4.3. The power of channel noise is assumed to be 0.5% of the maximum value of V_3 over a channel density range of 0.2~2.5. The power of transition noise is assumed to be 3% of the $V_1(k)$. And both of them increase within the channel density range considered. The fly-height errors induced by channel noise and transition noise are calculated with $\frac{3\lambda_3}{4\pi}\left(\left|\frac{\Delta V_3}{V_3}\right|+\left|\frac{\Delta V_1}{V_1}\right|\right)$.

The Harmonic power and the fly-height error versus channel density are plotted in Figs. 4.4 and 4.5, respectively.

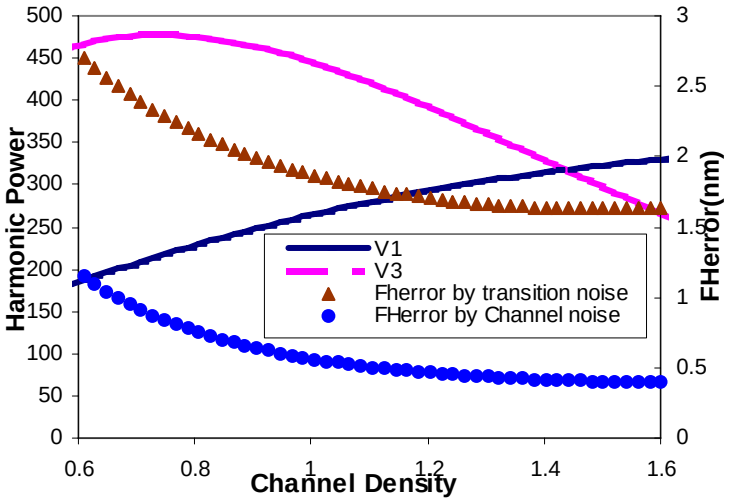

Fig. 4.4 Harmonic Power and fly-height error caused by transition noise and channel noise

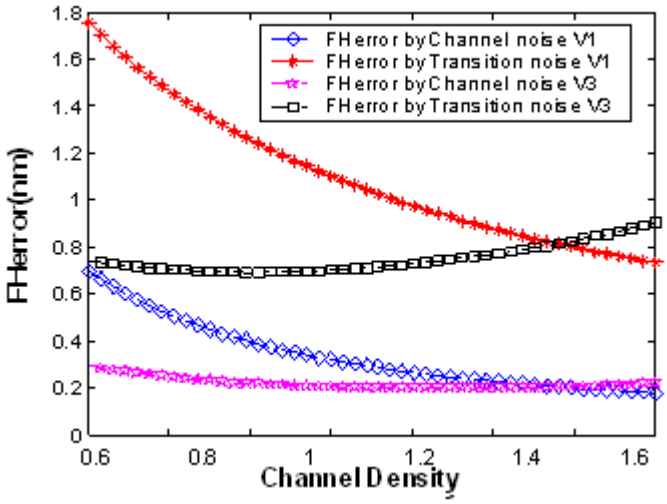

Fig. 4.5 Fly-height error caused by transition noise and channel noise

In general, results suggest testing at higher channel density will correspond to smaller error caused by channel noise and transition noise, if the channel noise can be assumed as constant. Furthermore, higher channel density leads to reduced flying height error caused by noise in V_1, no matter whether the noise comes from channel / electronics or transition noise. The reasons for such phenomenon include that the λ_3 in Eq. (4.8) decreases with density, and V_1 increases as channel density is increased within the channel density range considered. On the other hand, the fly-height error caused by

noises in V_3 increases after V_3 reaches its peak value, especially its transition noise component.

The approach to minimize the noise effect on fly-height measurement is to average the peak amplitude and remove the effect. Furthermore, more advance approaches such as low pass filter and envelope detection may be chosen for higher accuracy.

4.2.3.2 Envelope Detection and Testing Accuracy

Another approach in harmonic analysis is to use band pass filter to pick up the desired harmonic and use envelope detection approach to obtain harmonic amplitude. A typical block diagram of the programmable filters for the in-situ fly-height test is illustrated in Fig. 4.6.

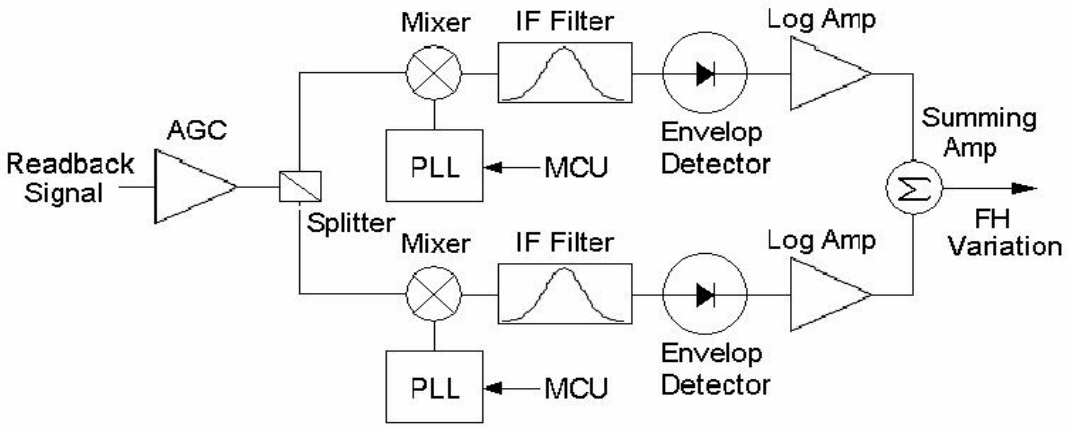

Fig. 4.6 Block diagram of the programmable filters for the in-situ fly-height test

As shown in Fig. 4.6, the readback signal will first reach automatic gain controller (AGC) unit, as is the common practice in every disk drive. Then, the amplified readback signal goes through the programmable filter which basically consists of two symmetrical channels of intermediate frequency (IF) mixer, IF band pass filter, mixer-based envelope detector and logarithmic amplifier. The local oscillators are

implemented in the form of wideband phase-lock loop (PLL) synthesizers, producing sinusoidal signals in the range of 100 kHz ~ 600 MHz. They are programmed individually via a serial interface with a micro controller unit (MCU), which communicates with the host computer and coordinates the system performance.
The output signal is the difference of the logarithmic output voltages from the two filtering channels.

The data read/write frequency is in the range of 50~500 MHz. The resonance frequency of slider and flying height is normally within the range of 20 kHz~200 kHz. Therefore, it is possible to introduce low pass filter, data averaging approach, and envelope detection to greatly reduce the effects of the high frequency noises, such as the media noise and channel noise. As a result, the fly-height testing repeatability will be mainly dependent on the voltage testing repeatability which is reflected by ΔV .

In other words, the envelope detection approach will be a better choice than peak detection approach. The discussion in the rest part of this chapter will be focused on envelope detection approach only.

4.3 Experiment Investigations

4.3.1 Experiments

This section describes the instrumentation as well as data acquisition technique used most frequently in this thesis work. Fig. 4.7 is a block diagram of the experimental configuration. The central part is a Guzik 1701 Spinstand tester, including a spinstand, mechanical control, and write/read electronics. The basic parametric tests (write

current, overwrite test and PW50 measurements) and frequency tests (roll-off curve measurements) were performed using the built-in functions of the WITE (Windows Integrated Test Environment) software package accompanying the Guzik spinstand. The playback signal from the head can either be analyzed with the Guzik's built-in testing routines, or input directly into external analyzers, such as a spectrum analyzer and a digital oscilloscope. All the measurement instruments can be interconnected and coordinated by GPIB (General Purpose Interface Bus) control.

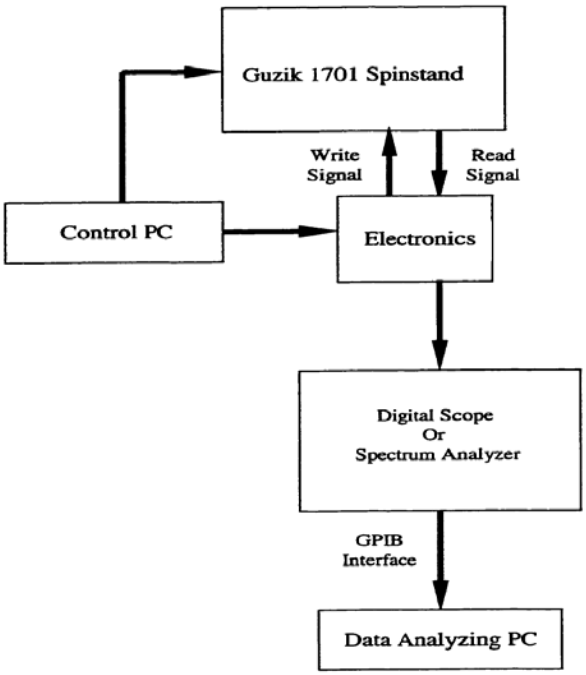

Fig. 4.7 Block diagram of the experimental configuration

Disks of 2.5 inch diameter are mounted on the air bearing motor spindles and the spindle rotational speed is programmable from 0 to 15000 RPM (revolutions per minute).

The spinstand used in this thesis work is equipped with a closed loop micro positioning system to achieve high positioning accuracy. In addition, skew angle could

be adjusted by using a rotary positioner that is driven by a step motor. The read/write process is controlled by the electronics that include the Read Write Analyzer (RWA), the Analog Box, the Universal Preamplifier (UP) and the Head Preamplifier. The read/write control commands from the control computer are sent to the UP through the RWA and Analog Box to control all the read/write signals including write data, write current and analog read data. Both the write and read functions can be synchronized with a timing signal derived from the physical rotation of the spindle.

The magnetic recording channel is characterized by both time and frequency responses. Consequently, data are usually taken in both of these two measurement domains. A Lecroy 7200 digital scope is used in this work for time domain analysis and Agilent 8562E/EC spectrum analyzers are utilized for frequency domain measurements. A digital oscilloscope converts an incoming analog waveform and stores the results as digital information.

A spectrum analyzer measures the frequency components of the incoming signal. It measures the time averaged signal amplitude in a narrow bandwidth centered about a frequency that is swept over the range of interest. The 8562E/EC spectrum analyzer used in this thesis work has a specialty that allows it to work in the zero-frequency-span mode. In this mode, the center frequency is fixed instead of being swept over a range and the spectrum analyzer measures the time variation of the component amplitude at the center frequency in the incoming signal. This feature makes it suitable for both the harmonic based fly-height and gap length estimation methods. The hardware electronics should be able to detect the changing amplitudes of the two major harmonics of the readback signal of the data pattern recorded at different writing

frequencies and obtain the logarithmic ratio of the detected harmonic amplitudes.

In our experiment, the readback signal got from the universal amplifier board of the Guzik spinstand is sent simultaneously into two 8562E/EC spectrum analyzers with identical channels and with centre frequency tuned to the two respective harmonics. With the results displayed in the logarithmic scale, the video outputs from the two spectrum analyzers can be sent directly into the digital oscilloscope and the instantaneous logarithmic ratio of the detected harmonic amplitudes are obtained with a simple subtraction process. Both the fly-height and gap width estimation are based on the harmonic ratio obtained. The equipment configuration is shown in Fig. 4.8.

Fig. 4.8 Experimental setup for harmonic based in-situ fly-height and gap width measurement

4.3.2 Heads and Media Characterization

A batch of GMR heads for 80 Gbit/in^2 areal density recording was used in the experimental investigation. The nominal shield-to-shield spacing is 75nm, and the slider used in this experiment has a fly-height about 11nm at velocity of 15000rpm. The air-bearing surface design of those sliders is illustrated in Fig. 4.9. The magnetic layer thickness of the disk media is about 20nm, $H_c = 4150$ Oe, and $M_r\delta = 0.37$.

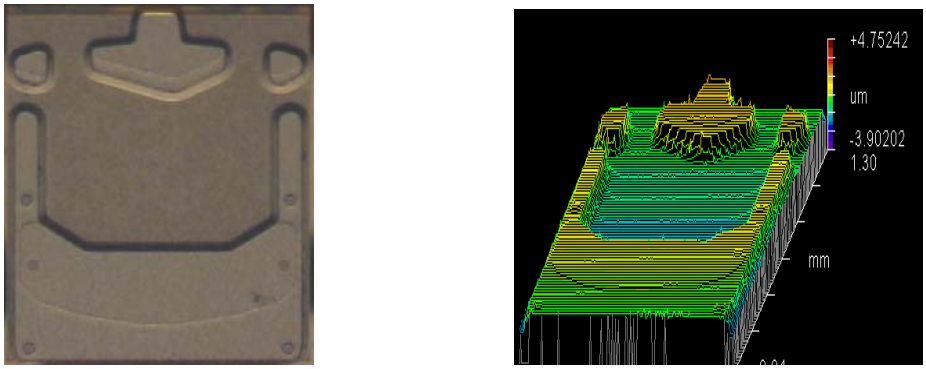

(a) (b)

Fig. 4.9 ABS design (a) 2-D image and (b) 3-D image of the slider used in the experiment

Write current and read bias current are important parameters, and suitable values should be chosen for characterization of a given head and medium combination. The choice of write current depends on a number of factors including the mode and wavelength of writing, the overwrite ratio and head saturation. Typical saturation test result is plotted in Fig. 4.10. Ideally, the write current that maximizes the short wavelength response should be selected for high-density recording. In practice, however, overwrite conditions dictate a somewhat higher operating current. The overwrite ratio in dB was determined by writing a square wave pattern at 33 KFCI (kilo flux change per inch), the low frequency (LF) data pattern, and then measuring the average peak amplitude *A1*. The old pattern was then overwritten (on the same track) with a high frequency (HF) data pattern (HF = 2LF) and the residual amplitude of the old LF pattern, *A2*, was then measured with a band pass filter (or a spectrum analyzer). The overwrite ratio is then found using

$$OW = 20\log_{10}(A_2 / A_1) \text{ (dB)}. \tag{4.9}$$

The logarithmic overwrite ratio is a measure of the ability of new recording data to suppress previously written data [24]. Hence, the write current value was chosen to be 45mA, which can provide good, overwrite capability with suitable wavelength

performance, and at the same time avoiding head saturation. Theory has shown that the overwrite ratio is dependent on hard transition shift and recording wavelength, and hence this ratio varies with different recording conditions [23]. With high current values, the peak replay voltage remains steady as shown in Fig. 4.10. This was attributed to head saturation, where large values of current are required to produce significant change in the head field gradient to affect the written transition width and hence in peak replay voltage [17]. As a result, the transition lengths remain almost constant irrespective of the applied head field gradient.

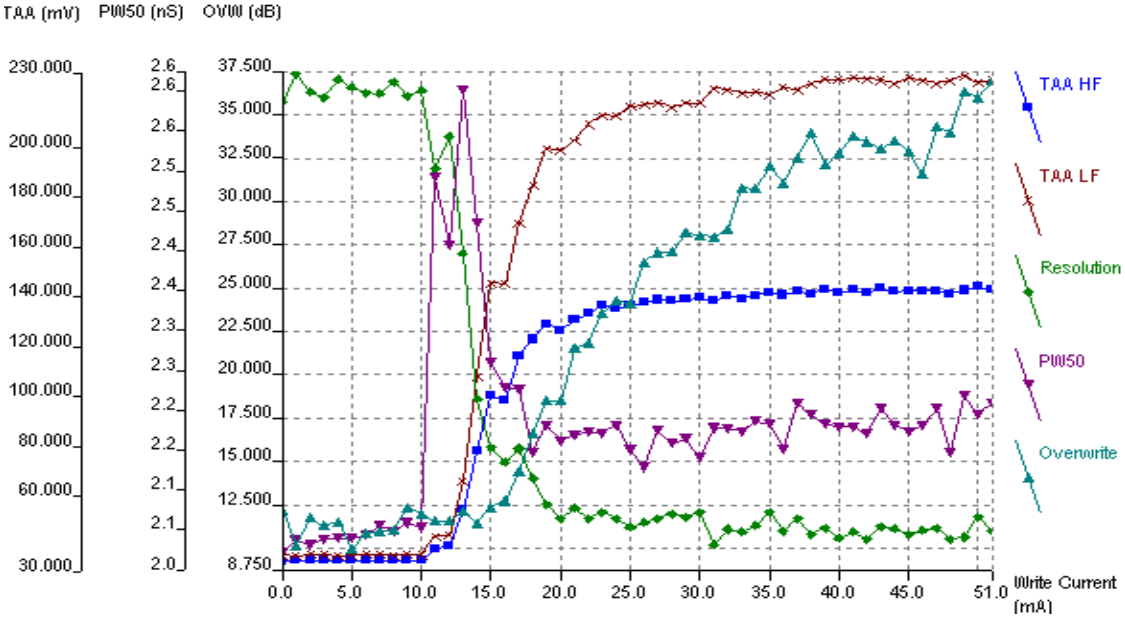

Fig. 4.10 Track average voltages; overwrite ratio and PW50 as a function of write current

The transfer curve of MR element is intrinsically nonlinear, which causes the readback pulse of MR heads to be asymmetry. We should find an optimum value of the read bias current to ensure low readback amplitude asymmetry (also called track average amplitude (TAA) asymmetry in Guzik tester) and high TAA value. Fig. 4.11 shows a typical MR saturation curve where the read bias current is selected as -4mA.

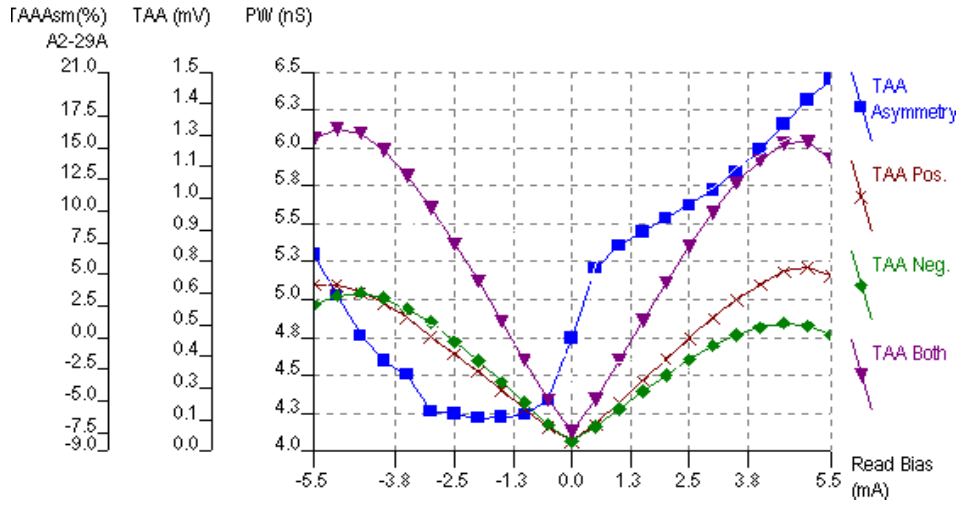

Fig. 4.11 MR saturation curves

Roll-off curve obtained using the frequency testing function in Guzik Spinstand, tested at RPM 15000 is plotted in Fig. 4.12. The average track amplitude of HF pattern decreases to half of its maximum value at around 400KFCI.

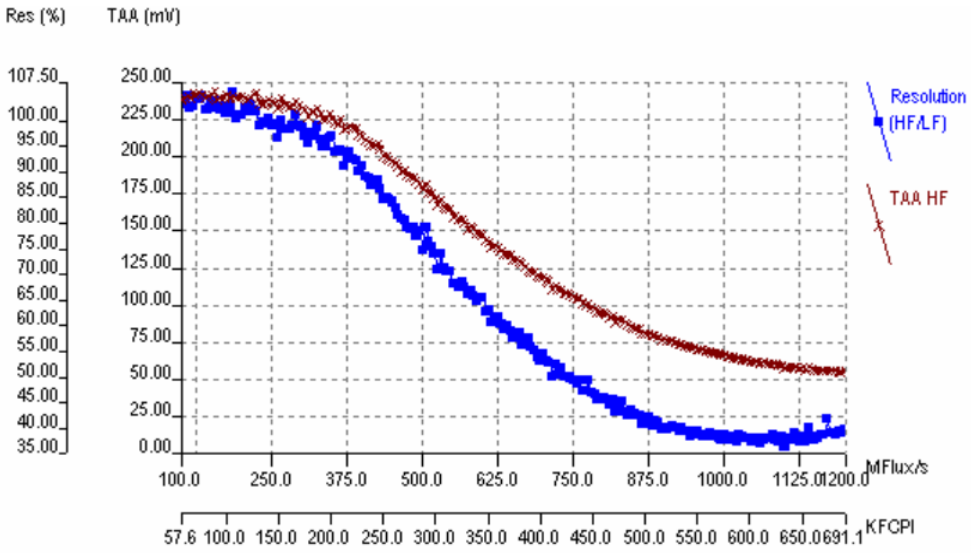

Fig. 4.12 Roll-off curve

4.3.3 Comparison of Theoretical and Experiment Waveforms

The waveform at recording density 1.32 of the same head in Fig. 4.10 was captured and plotted in Fig. 4.13(a) and the theoretical simulation waveform with tanh transition model and Fourier series method introduced in Chapter 3 is plotted in Fig.

4.13(b). The simulation parameters are same as those used in the experiment, and the head, media and testing system parameters are illustrated in Table 4.2. The PW50 is tested with saturation test function of GUZIK as in Fig. 4.10, and is also confirmed with oscilloscope capturing the averaged isolated pulses.

PW50(nm)	g(nm)	t(nm)	d(nm)	FH(nm)	magnetic thickness(nm)	RPM (r/min)	Radius(inch)
97	36	3	21	11	24	15000	1.1054

Table 4.2 Head, media, and testing system parameters

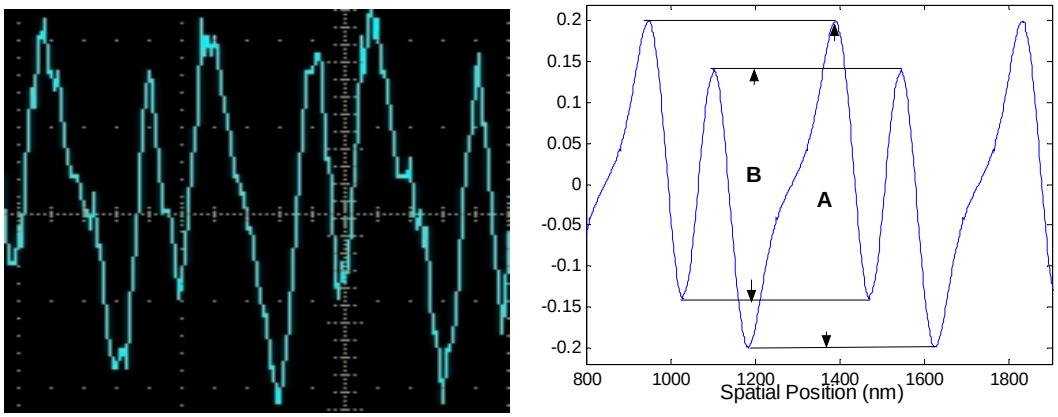

(a) (b)

Fig. 4.13 (a) Experiment waveform at density 1.32 (b) Simulation waveform at density1.32

In Fig. 4.13(b), the A and B values are defined as the peak-to-peak values of the "1001" pulses and "11" respectively, and the A/B ratio of the experimental waveform and the simulation waveform at multiple densities are compared in Fig. 4.14.

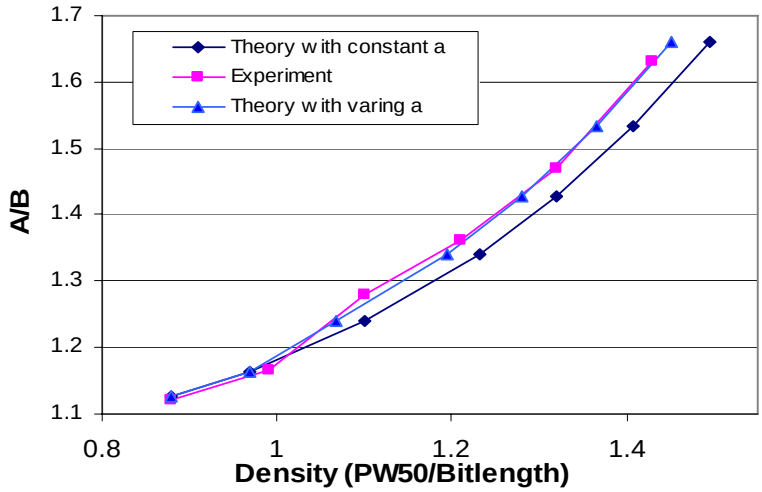

Fig. 4.14 Comparison between A/B of experiment and simulation waveforms at multiple densities

The A/B ratios tested at higher densities are bigger than that with simulation results as in the Fig. 4.14 above. It has been reported that the demagnetization field from the previous transitions [13, 14] and the nonlinearities at high density will lead to increased transition parameter. Therefore, we fit the experimental result with varying transition parameter a value in simulation, and the transition parameter at different densities is illustrated in Table 4.3.

Density (PW50/Bitlength)	0.88	0.99	1.1	1.21	1.32	1.43
Fitting a value (nm)	12	12	13	13	13	13

Table 4.3 Transition Parameter for Fitting

4.3.4 Testing Repeatability

4.3.4.1 Triple Harmonic Method

Experiment was done to investigate the fly-height variation and testing repeatability. Nine heads of the same batch with similar design parameters as in Section 4.2.2 was

used in the experiment. Triple harmonic code of different recording densities were written on radius of 1.1 inch of a 2.5 inch disk rotating at 15000 RPM, and then the first three harmonics of readback signal are tested.

For each head and at each selected testing density, testing was done twice with band erase operation in between, and the differences between the harmonic ratios of the two testing are used to derive the possible fly-height variation ΔFH . The ΔFH derived with $\ln(\frac{V_2}{V_1})$, $\ln(\frac{V_3}{V_1})$ and $\ln(\frac{V_3}{V_2})$ at different densities are illustrated in Tables 4.4, 4.5 and 4.6, respectively. The maximum and average ΔFH of these nine heads are calculated and plotted in Figs 4.15 and 4.16, respectively. The average PW_{50} of 104nm is used for user density calculation.

Head	PW50 (nm)	ΔFH (nm) (600 Mflux/s)	ΔFH (nm) (450 Mflux/s)	ΔFH (nm) (300 Mflux/s)	ΔFH (nm) (240 Mflux/s)	ΔFH (nm) (150 Mflux/s)	ΔFH (nm) (120 Mflux/s)
1	100.027	0.025	0.113	0.224	0.380	0.149	0.268
2	99.304	0.025	0.040	0.135	0.011	0.075	0.265
3	97.617	0.004	0.000	0.033	0.086	0.058	0.361
4	104.728	0.091	0.038	0.147	0.362	0.081	0.248
5	106.768	0.102	0.119	0.052	0.201	0.385	0.416
6	95.527	0.059	0.059	0.061	0.086	0.675	0.226
7	110.370	0.006	0.005	0.034	0.007	0.118	0.161
8	102.827	0.026	0.003	0.186	0.088	0.092	1.139
9	119.125	0.004	0.059	0.160	0.076	0.113	0.094
Max	119.125	0.102	0.119	0.224	0.380	0.675	1.139
Average	104.033	0.038	0.048	0.115	0.144	0.194	0.353

Table 4.4 Fly-height variation calculated with V_{21} of triple harmonic method

Head	PW50 (nm)	ΔFH (nm) (600 Mflux/s)	ΔFH (nm) (450 Mflux/s)	ΔFH (nm) (300 Mflux/s)	ΔFH (nm) (240 Mflux/s)	ΔFH (nm) (150 Mflux/s)	ΔFH (nm) (120 Mflux/s)
1	100.027	0.016	0.007	0.017	0.103	0.040	0.298
2	99.304	0.011	0.047	0.026	0.060	0.037	0.135
3	97.617	0.003	0.001	0.016	0.031	0.059	0.221
4	104.728	0.023	0.032	0.059	0.069	0.032	0.210
5	106.768	0.058	0.109	0.039	0.069	0.217	0.011
6	95.527	0.058	0.115	0.100	0.183	0.166	0.149
7	110.370	0.001	0.008	0.077	0.007	0.016	0.099
8	102.827	0.007	0.016	0.006	0.005	0.203	0.335
9	119.125	0.024	0.017	0.025	0.008	0.135	0.059
Max	119.125	0.058	0.115	0.100	0.183	0.217	0.335
Average	104.033	0.022	0.039	0.041	0.059	0.100	0.169

Table 4.5 Fly-height variation calculated with V_{31} of triple harmonic method

Head	PW50 (nm)	ΔFH(nm) (600 Mflux/s)	ΔFH (nm) (450 Mflux/s)	ΔFH (nm) (300 Mflux/s)	ΔFH (nm) (240 Mflux/s)	ΔFH (nm) (150 Mflux/s)	ΔFH (nm) (120 Mflux/s)
1	100.027	0.006	0.100	0.189	0.175	0.069	0.329
2	99.304	0.003	0.053	0.084	0.132	0.002	0.005
3	97.617	0.003	0.001	0.000	0.025	0.059	0.081
4	104.728	0.044	0.025	0.265	0.225	0.018	0.172
5	106.768	0.013	0.098	0.130	0.339	0.049	0.438
6	95.527	0.058	0.171	0.139	0.453	0.343	0.072
7	110.370	0.003	0.020	0.187	0.007	0.085	0.360
8	102.827	0.040	0.035	0.197	0.097	0.313	0.469
9	119.125	0.052	0.092	0.110	0.060	0.156	0.212
Max	119.125	0.058	0.171	0.265	0.453	0.343	0.469
Average	104.033	0.025	0.066	0.145	0.168	0.122	0.237

Table 4.6 Fly-height variation calculated with V_{32} of triple harmonic method

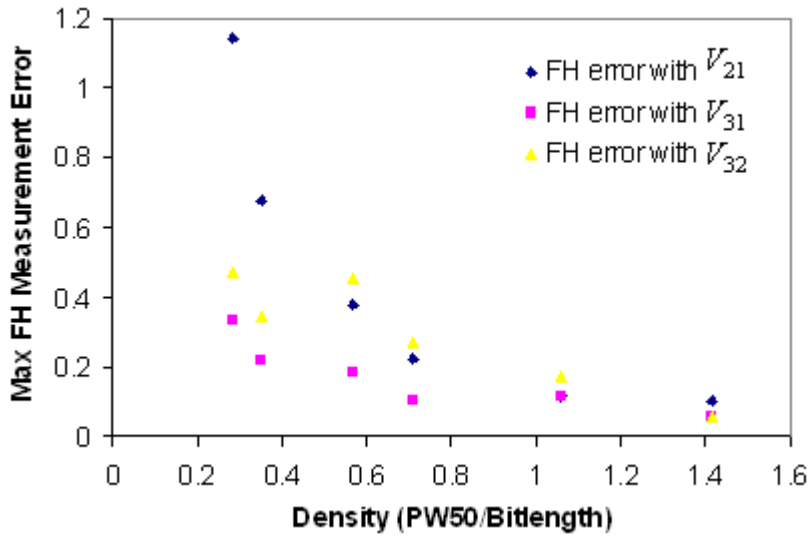

Fig. 4.15 Maximum fly-height variation (nm) with different harmonic ratios and densities

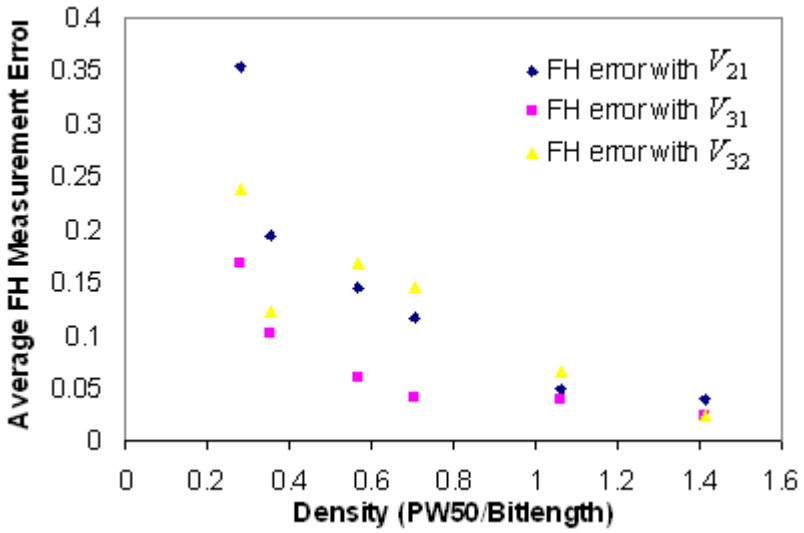

Fig. 4.16 Average fly-height variation (nm) with different harmonic ratios and densities

It could be seen from Figs. 4.15 and 4.16 that the fly-height variation shows a clear descending trend with increasing recording density, and the average fly-height variation of the nine heads is much smaller than the maximum fly-height variation. Furthermore, ΔFH_{31} decreases fast and reaches its almost steady value when the channel density is above 0.7. Also, ΔFH_{31} is much smaller than ΔFH_{21} and ΔFH_{32} when the channel density is low whilst the ΔFH_{31}, ΔFH_{21}, and ΔFH_{32} become comparable when the channel density is high. It can also be observed that ΔFH_{21} is bigger than ΔFH_{32} at density below 0.4, but they become comparable at higher densities.

Simulation is done for the fly-height variation with triple harmonic code based on Eq. (4.8). Assuming that ΔV is constant for all harmonics and its value is about 0.5% of the peak voltage of V_3 in Fig. 3.21, the ΔFH_{31}, ΔFH_{21} and ΔFH_{32} are plotted in Fig. 4.17, which shows similar trend as experiment data. The minor difference may be due

to factors such as noise, testing resolution, and asymmetry of the waveform, which may affect the even harmonic.

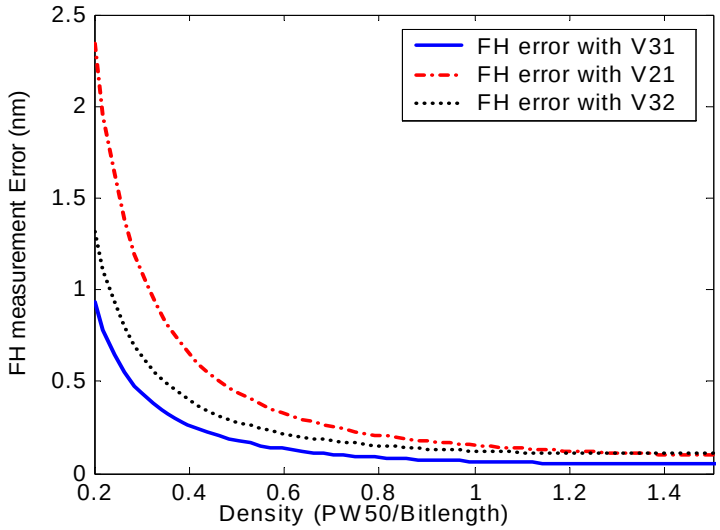

Fig. 4.17 Simulated fly-height variation with different harmonic ratios and densities

In conclusion, for triple harmonic method, *FH* testing with the $\ln(\frac{V_3}{V_1})$ at higher density is preferred for both high sensitivity and repeatability.

4.3.4.2 Square Wave Method

Same experiment was done for fly-height measurement repeatability with square waveform method. The ΔFH derived with $\ln(\frac{V_3}{V_1})$ at different densities is illustrated in Table 4.6, and the maximum and average ΔFH of these nine heads are calculated and plotted in Fig. 4.18.

Head	PW50 (nm)	ΔFH 40 (Mflux/s)	ΔFH 50 (Mflux/s)	ΔFH 80 (Mflux/s)	ΔFH 100 (Mflux/s)	ΔFH 150 (Mflux/s)
1	100.027	0.063	0.056	0.017	0.294	0.678
2	99.304	1.100	0.425	0.019	0.048	0.295
3	97.617	0.134	0.100	0.052	0.206	0.416
4	104.728	0.134	0.321	0.200	0.033	0.071
5	106.768	0.520	0.198	0.079	0.246	0.206
6	95.527	0.068	0.804	0.021	0.091	0.326
7	110.370	0.272	0.043	0.077	0.180	0.006
8	97.554	0.493	0.030	0.204	0.003	0.228
9	119.125	0.173	0.084	0.086	0.001	0.030
Max	119.125	1.100	0.804	0.204	0.294	0.678
Average	103.447	0.329	0.229	0.084	0.123	0.251

Table 4.7 Fly-height variation calculated with V_{31} of all one pattern at different densities

It could be seen that the calculated fly-height error decreases first from density 0.1 and reaches the minimal fly-height error at around density 0.2. The ΔFH stabilizes within a small density range and then increases fast.

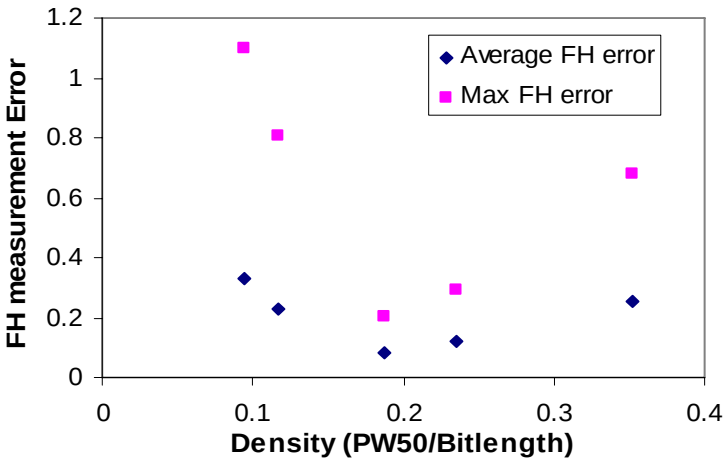

Fig. 4.18 Average and maximum fly-height variation (nm) of all one pattern at different densities

Simulation is done for the fly-height variation based on Eq. (4.6). Assuming again that the voltage testing resolution induced ΔV is a constant for all harmonics and its value is about 0.5% of the peak voltage of V_3 in Fig. 3.21, the ΔFH_{31} is plotted in Fig. 4.19:

$$\Delta FH_{31} = \left|\Delta V_3 * \frac{\partial FH}{\partial V_3}\right| + \left|\Delta V_1 * \frac{\partial FH}{\partial V_1}\right| = \frac{3\lambda_3}{2\pi}\left(\left|\frac{\Delta V_3}{V_3}\right| + \left|\frac{\Delta V_1}{V_1}\right|\right). \quad (4.10)$$

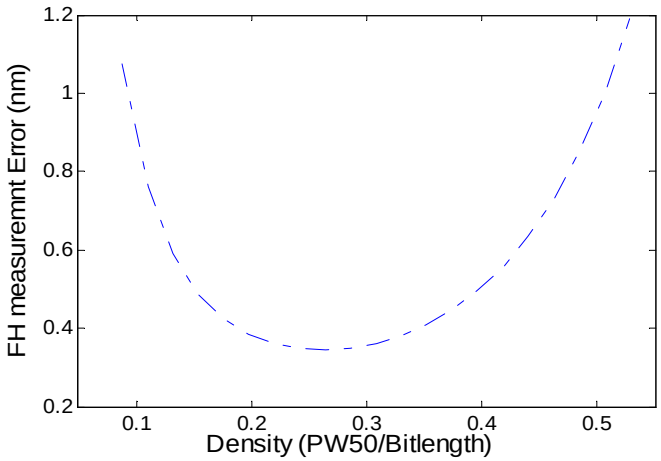

Fig. 4.19 Simulated fly-height variation of all one pattern at different density

Compared with triple harmonic method, the suitable testing range with small fly-height variation for square waveform method is much narrower. Furthermore, the ΔFH increases fast after density 0.3 due to the fast decrease of V_3. The triple harmonic method is better in terms of testing repeatability.

4.4 Summary

Sensitivity and precision are the two important criteria in evaluating harmonic based fly-height measurements methods. Triple harmonic *FH* method can achieve higher sensitivity and precision than square wave harmonic method.

Chapter 5
Harmonic Analysis Method, Gap Length Effect and Estimation of Gap Length Deviation

This chapter is focused on the following two topics. The first is experimental investigation on fly-height reading deviation caused by gap length difference among different heads. Experimental data suggests that the deviation increases as the testing channel density increases. Analysis suggests that the only possible root cause for such phenomena is gap length difference of different heads. The second topic is how to estimate gap length difference of different heads of same design and from the same fabrication process. A novel method is proposed for the quantitative estimation of the gap length difference of a batch of MR/GMR heads with same structure and similar design.

5.1 Gap Length Effect on Fly-Height Measurement

5.1.1 Experiment Design

Fly-height is estimated by the following equation, as discussed in the previous chapters

$$FH = -\frac{3\lambda_3}{4\pi}\ln(\frac{V_3}{V_1}) - \ln C(g,\delta,t,a,\lambda) \qquad (5.1)$$

.

However, it is not easy to estimate the actual gap length g and free layer thickness t of each testing head, magnetic layer thickness δ of disk media used in testing and

transition parameter a. Therefore, a common practice is to use the nominal value of those parameters to calculate $\ln C(g, \delta, t, a, \lambda)$ and, then, the fly-height. Such an approach could be acceptable only if the differences between actual $\ln C(g, \delta, t, a, \lambda)$ and $\ln C(g, \delta, t, a, \lambda)$ calculated with the nominal value of those head-media parameters are negligible.

Fly-Height differences of the testing heads are not a function of channel density. Therefore the fly-height difference histograms obtained at different channel densities should be the same if nominal values can really be used to replace the actual values of head-media parameters with negligible error.

The purpose is to analyze the fly-height deviation caused by the difference between actual head-media parameters and nominal parameters. Therefore, it is acceptable to use $FH + \ln C$ to calculate fly-height difference histogram among different heads (same nominal value of g and t) and evaluate fly-height difference caused by the deviation of head-media parameters from their nominal values.

5.1.2 Experimental Conditions and Nominal Head-Media Parameters

A batch of 130 heads with same nominal head parameters and same design are used in the experiment. The parameters of those heads are same as the heads used in the experimental study reported in Chapter 4, the nominal shield-to-shield spacing of those heads is 75nm and their nominal fly-height is about 11nm at velocity of 15000rpm. The magnetic layer thickness of the medium is about

24nm, $H_c = 4150\ Oe$, and $M_r\delta = 0.37\ memu/cm^2$.

The triple harmonic code is written at radius of 1.1 inch of a 2.5 inch disk rotating at 15000 rpm, and the first and third harmonics are used for fly-height calculation.

5.1.3 Experimental Results and Discussion

Fig. 5.1 illustrates fly-height difference histogram among those 130 heads assuming the head-media parameters can be replaced by their nominal values.

The fly-height with maximum likelihood among those 130 heads ($\overline{FH_{130}}$) is selected as reference fly-height for the deviation calculation

$$\Delta FH_i = \overline{FH_{130}} - FH_i \ . \tag{5.2}$$

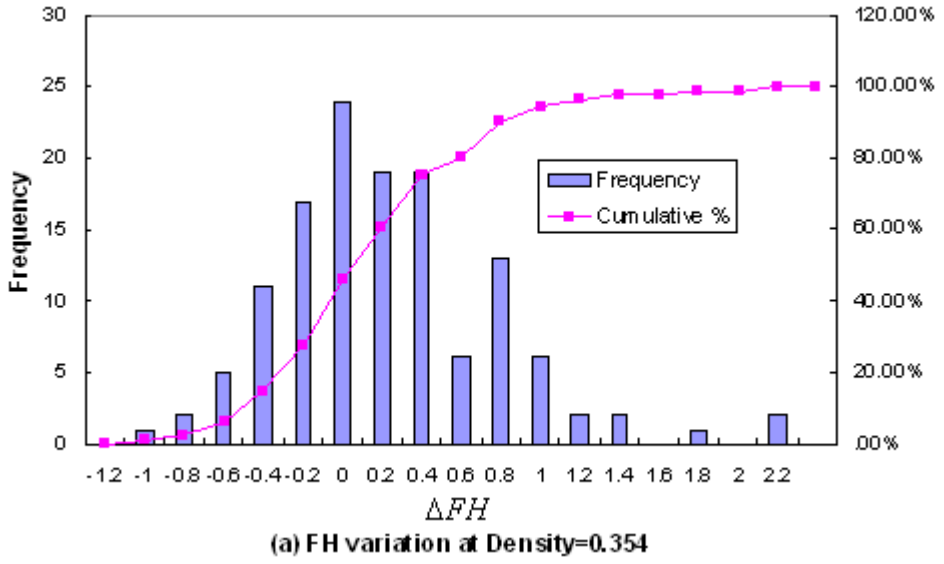

(a) FH variation at Density=0.354

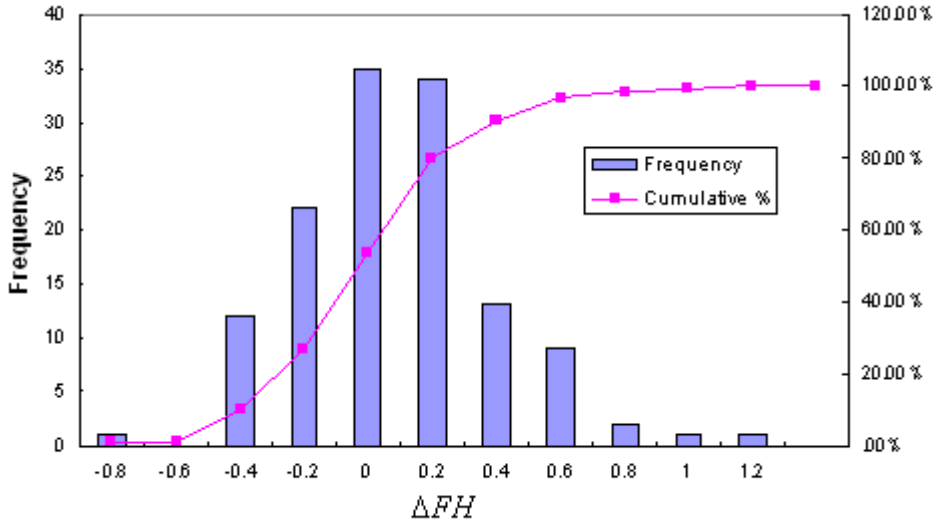

(b) FH variation at Density=0.566

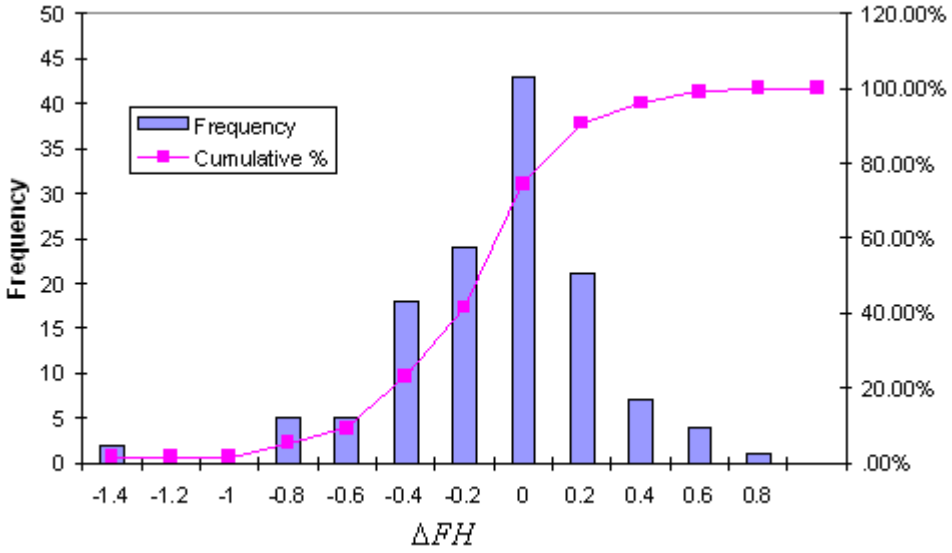

(c) FH variation at Density=0.708

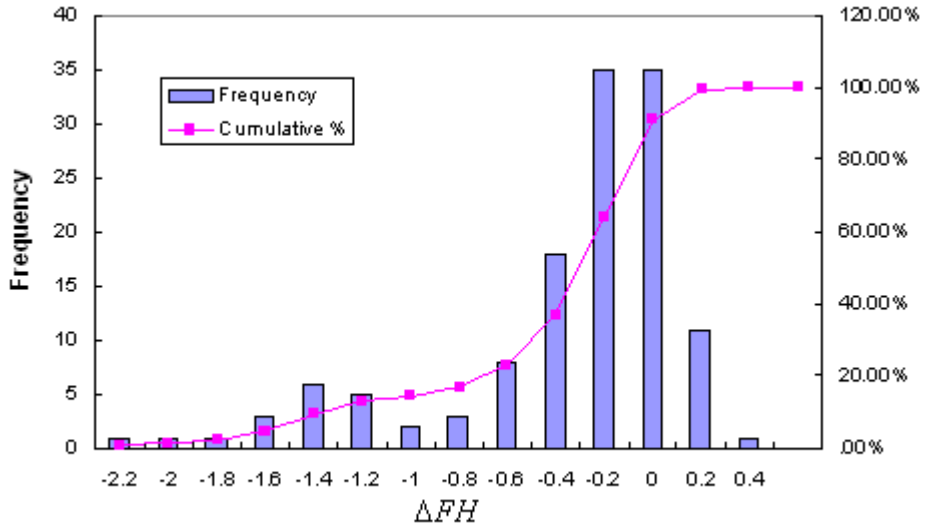

(d) FH variation at Density=1.061

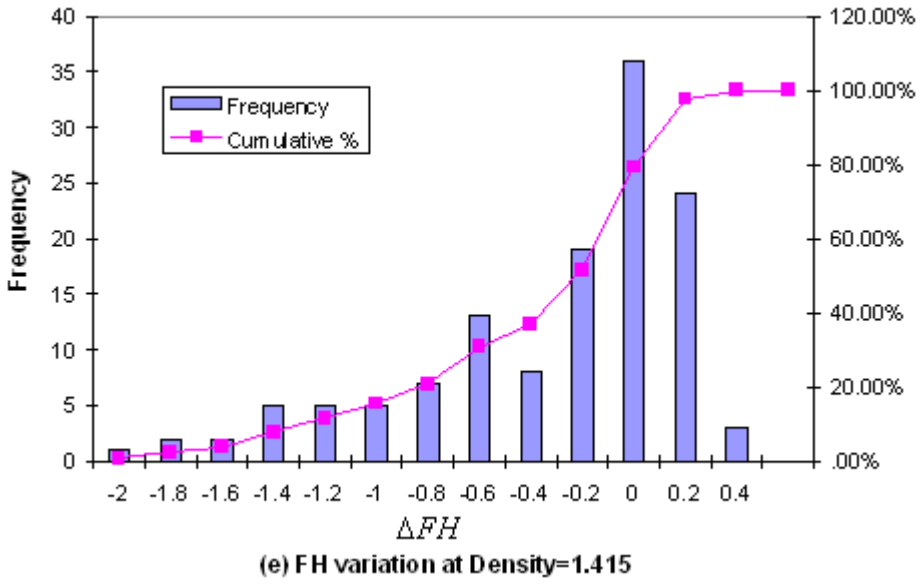

Fig. 5.1 Fly-height variation ΔFH of 130 heads calculated at different testing densities

As mentioned before, the fly-height is not a function of channel density and the fly-height difference histograms obtained at different channel densities should be same if the nominal values can be really used to replace the actual values of the related head-media parameters. However, it can be observed clearly that the histograms obtained at different channel densities are quite different.

From Eq. (5.1), we know that fly-height is a constant relative to testing density whilst $\ln C$ varies with density. If the $\ln C$ is same for all the heads, there should be no difference between the above figures. The difference of the above figures reminds that there exists $\ln C$ variation within the 130 heads and it is the $\ln C$ variation with testing density which leads to the difference of the above figures. In other words, it is not acceptable to use nominal values to replace the actual values, especially at high channel densities.

5.1.4 Further Experimental Analysis and Phenomenon Confirmation

Further experimental analysis is focused on a group of heads of negligible fly-height differences at one channel density, if nominal head-media parameters are used to replace the actual ones. The investigation is to see how the fly-height difference histograms for these heads change when the testing channel density is changed (still using nominal head-media parameters to replace the actual ones).

A group of 43 heads at maximum likelihood fly-height tested at the channel density 0.708, as illustrated in Fig. 5.1, are selected for the investigation in this section. Those heads have similar calculated $FH + \ln C$ value (variation<0.2nm) at the density 0.708.

Assuming that the maximum likelihood value of $FH + \ln C$ of the 43 heads is $\overline{FH_{43} + \ln C_{43}}$, for each head, we could calculate the $\Delta(FH_i + \ln C_i)$ as

$$\Delta(FH_i + \ln C_i) = (\overline{FH_{43} + \ln C_{43}}) - (FH_i + \ln C_i) \quad (5.3)$$

The histograms of the $FH + \ln C$ variation $\Delta(FH_i + \ln C_i)$ of these 43 heads calculated at the densities 0.708, 1.061 and 1.415 are plotted in Figs. 5.2 (a), 5.2 (b) and 5.2 (c), respectively.

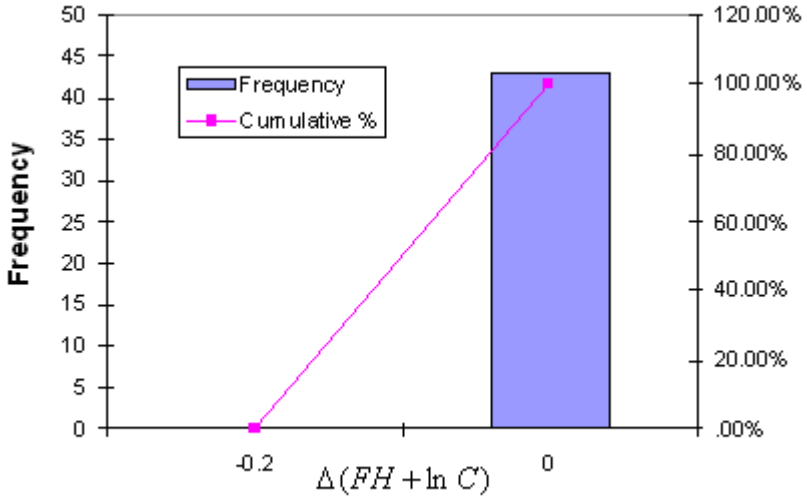

(a) FH+lnC Variation at Density 0.708

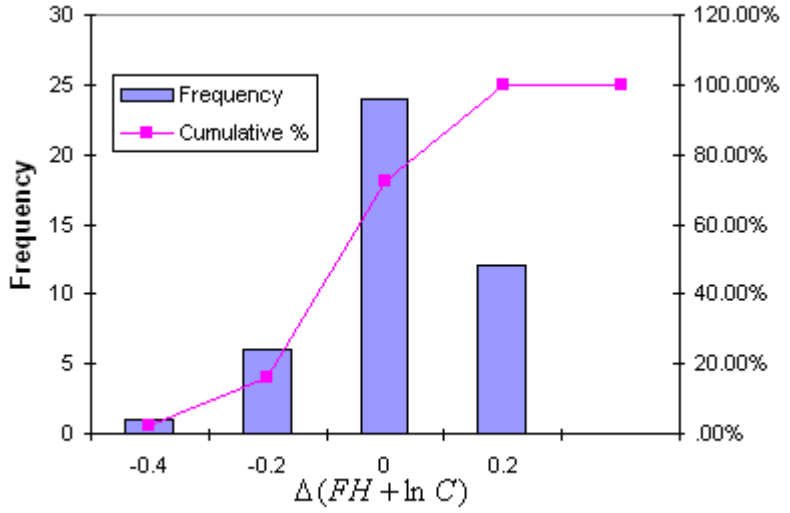

(b) FH+lnC variation at Density=1.061

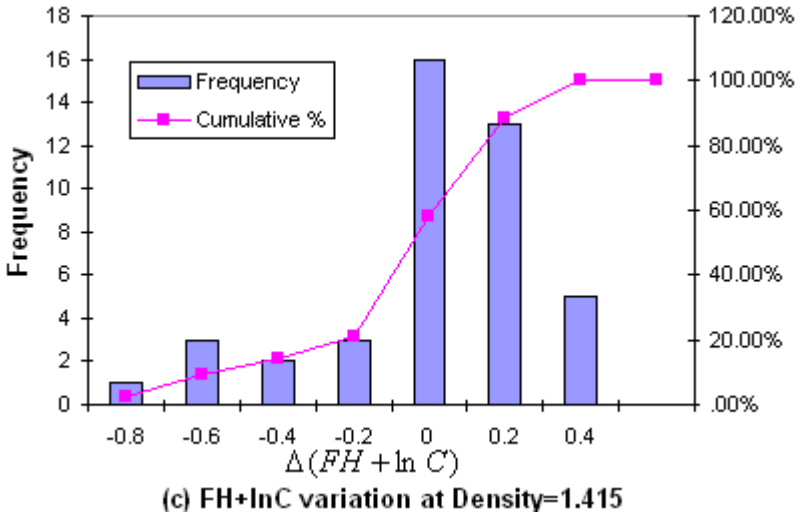

(c) FH+lnC variation at Density=1.415

Fig. 5.2 $\Delta(FH+\ln C)$ of 43 heads calculated at different densities

From Fig. 5.2, we can see the calculated $FH+\ln C$ variation of these 43 heads with

density. The $FH + \ln C$ values of the 43 heads differ within the range of 0.2nm at density 0.708. The variation shows an increasing trend with the increase of density: the variation range increased to 0.6nm and then 1.2nm, when channel density is increased to 1.061 and then 1.415, respectively. Furthermore, the shape of the distribution changes with density, and the difference becomes bigger when density difference becomes larger.

Table 5.1 illustrates the $FH + \ln C$ value of the 43 heads at three densities and their relative rank based on the $FH + \ln C$ values of each head. It is clear that the values of the same head differ at different density, and the relative rank also changes when the channel density is changed. If the $\ln C$ is same for all the heads, the relative rank of the heads will be same at different densities since the relative fly-height difference remains the same. Otherwise, the variation in $\ln C$ among the different heads makes the relative rank of the heads change at different densities.

FH+lnC(0.708)	rank(0.708)	FH+lnC(1.061)	rank(1.061)	FH+lnC(1.415)	rank(1.415)
-6.199	1	-1.976	31	0.208	30
-6.196	2	-2.198	4	-0.097	4
-6.194	3	-2.246	2	-0.015	10
-6.186	4	-2.087	13	0.148	21
-6.181	5	-2.218	3	-0.166	1
-6.179	6	-2.014	25	0.287	33
-6.173	7	-1.752	42	0.612	39
-6.172	8	-1.689	43	0.751	40
-6.171	9	-1.903	35	-0.052	6
-6.168	10	-2.083	14	0.175	24
-6.165	11	-2.027	23	0.171	23
-6.155	12	-2.041	20	0.319	34
-6.151	13	-1.848	39	0.434	37
-6.146	14	-2.162	7	0.055	16
-6.142	15	-1.977	29	0.154	22
-6.140	16	-2.042	19	0.208	29
-6.139	17	-1.990	28	-0.061	5
-6.131	18	-2.030	22	0.086	18

-6.124	19	-2.124	12	-0.035	7
-6.120	20	-2.187	6	0.002	11
-6.119	21	-1.812	41	0.873	41
-6.119	22	-2.151	9	-0.015	9
-6.107	23	-2.039	21	0.188	26
-6.100	24	-2.157	8	0.053	15
-6.092	25	-2.194	5	0.035	14
-6.089	26	-1.860	38	0.374	36
-6.079	27	-2.067	18	0.895	42
-6.068	28	-2.249	1	-0.151	2
-6.068	29	-2.142	11	-0.031	8
-6.048	30	-1.976	30	0.065	17
-6.043	31	-2.006	26	0.194	28
-6.039	32	-1.895	37	0.605	38
-6.038	33	-1.941	33	0.194	27
-6.034	34	-2.147	10	0.021	13
-6.028	35	-2.082	15	0.945	43
-6.022	36	-2.077	16	0.010	12
-6.020	37	-1.991	27	0.211	31
-6.018	38	-1.901	36	0.355	35
-6.018	39	-1.837	40	0.255	32
-6.008	40	-2.069	17	-0.107	3
-6.008	41	-1.973	32	0.141	19
-6.004	42	-1.940	34	0.147	20
-6.003	43	-2.023	24	0.185	25

Table 5.1 The value and rank of $FH + \ln C$ of 43 heads at different densities

5.1.5 Root Cause Identification

A) Media Thickness Effect

From (5.1) we know that $\ln C$ is a function of both the head and media parameters, including the gap length g, free layer thickness t, magnetic thickness δ, transition parameter a, *etc.*

The experimental work reported above is from the same disk. Therefore, the histogram difference can not be from media thickness. Furthermore, as illustrated in Fig. 5.3, media thickness difference does cause variation of fly-height but this variation does

not change much at different channel densities. In other words, the histogram change can not be due to media thickness variation.

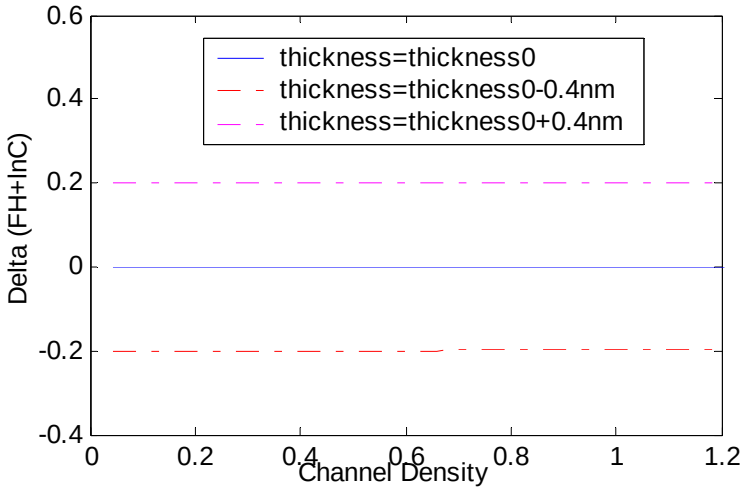

Fig. 5.3 $\Delta(FH + \ln C)$ (nm) variation at different channel densities of different media thickness (nominal gap length $\delta_0 = 20nm$)

B) Transition Parameter Effect

The transition parameter *a* may differ at different testing densities, as reported in Chapter 4 and Fig. 4.14. However, the transition parameter effect would be same for different reading heads and should not affect the relative ranking among different heads. In other words, the experiment data reported above suggest that transition parameter can not be ranked as the main cause.

C) Free Layer Thickness Effect

Another possible source is the variation in free layer thickness *t* variation among different heads. However, the free layer thickness is merely around 3 nm and its variation can not be more than 10% according to current sputtering technology. In other words, the effect of free layer thickness variation is also negligible in being the root cause.

D) Gap Length Effect

Given the above analysis, we could say that the change in relative rank of $FH + \ln C$ values of the 43 heads at different testing densities is mainly due to the gap length variation of the different heads. Fig. 5.4 illustrates the relationship between $FH + \ln C$ and channel density. The relationship suggests that the value of $FH + \ln C$ increases as the channel density is increased, if the actual gap length is different from its nominal value.

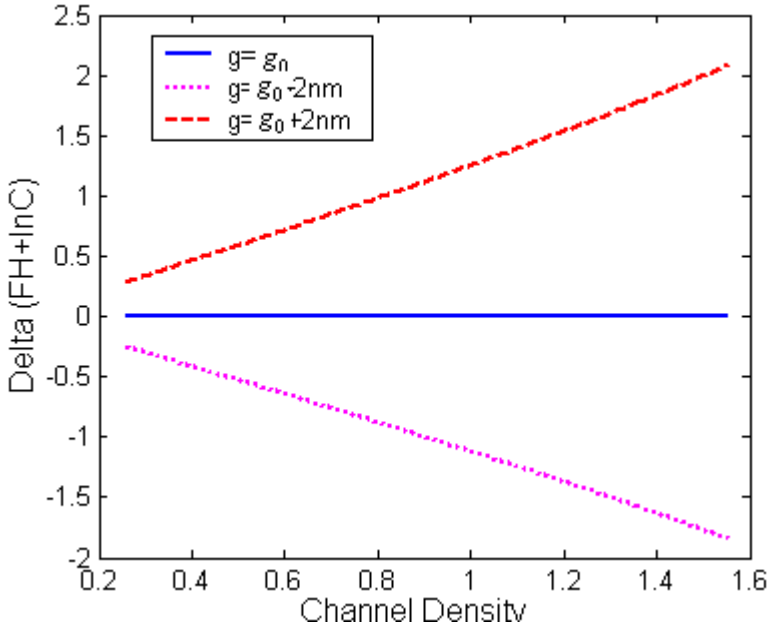

Fig. 5.4 $\Delta FH + \ln C$ (nm) variation at different channel densities and different gap lengths (nominal gap length $g_0 = 36nm$)

5.1.6 Further Discussion on Gap Length Effect at Different Sensitivity Variation with Density

To further study the density effect on the $\ln C$ variation among the batch of 43 heads caused by gap length variation of the different heads, we calculated the $\ln C$ difference ($\Delta \ln C$) between two different densities with the following formula:

$$\Delta \ln C(\lambda_1, \lambda_2) = -\frac{3\lambda_1}{4\pi} \ln(\frac{V_3}{V_1})\Big|_{\lambda 1} + \frac{3\lambda_2}{4\pi} \ln(\frac{V_3}{V_1})\Big|_{\lambda 2}, (\lambda_1 < \lambda_2) \quad (5.4)$$

where the λ_1 and λ_2 are the wavelengths of the two recording densities tested, respected. Here, the fly-height term in (5.1) has been eliminated given the fact that fly-height is a constant for each head.

Function $\Delta\Delta \ln C(\lambda_1, \lambda_2)$ is introduced to describe the variation of $\Delta \ln C$ among the batch of heads using maximum likelihood value as a reference point:

$$\Delta\Delta \ln C_i(\lambda_1, \lambda_2) = \Delta \ln C_i(\lambda_1, \lambda_2) - \overline{\Delta \ln C_{43}(\lambda_1, \lambda_2)} \quad (5.5)$$

where $\overline{\Delta \ln C_{43}(\lambda_1, \lambda_2)}$ is the maximum likelihood value of $\Delta \ln C_i(\lambda_1, \lambda_2)$ of the 43 heads.

The $\Delta\Delta \ln C(\lambda_1, \lambda_2)$ of the 43 heads with multiple density combinations are calculated and the histograms of the results are plotted in Fig. 5.5.

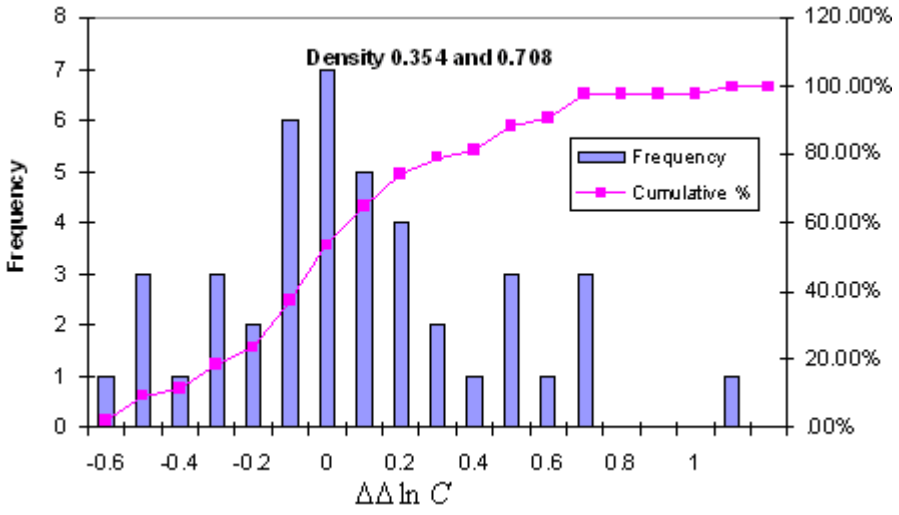

Fig. 5.5 (a) $\Delta \ln C$ variation $\Delta\Delta \ln C$ of 43 heads calculated at densities 0.354 and 0.708

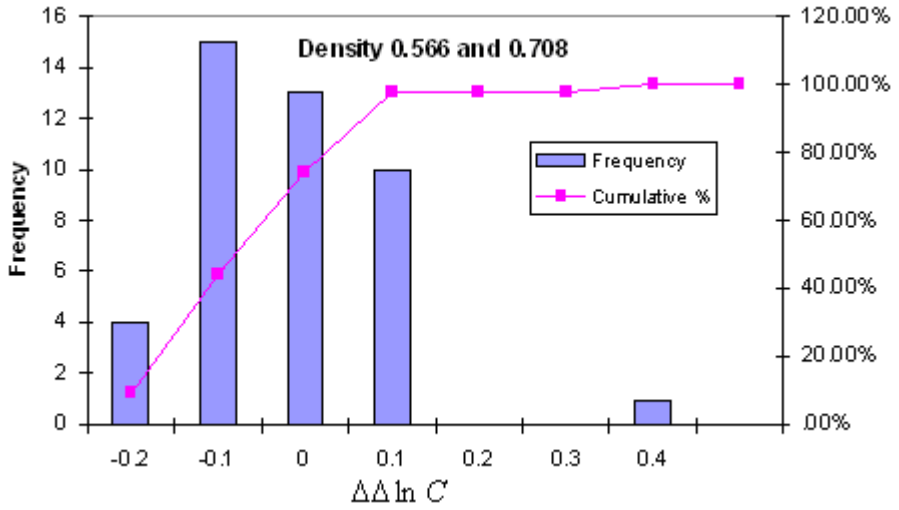

Fig. 5.5 (b) $\Delta \ln C$ variation $\Delta\Delta \ln C$ of 43 heads calculated at densities 0.566 and 0.708

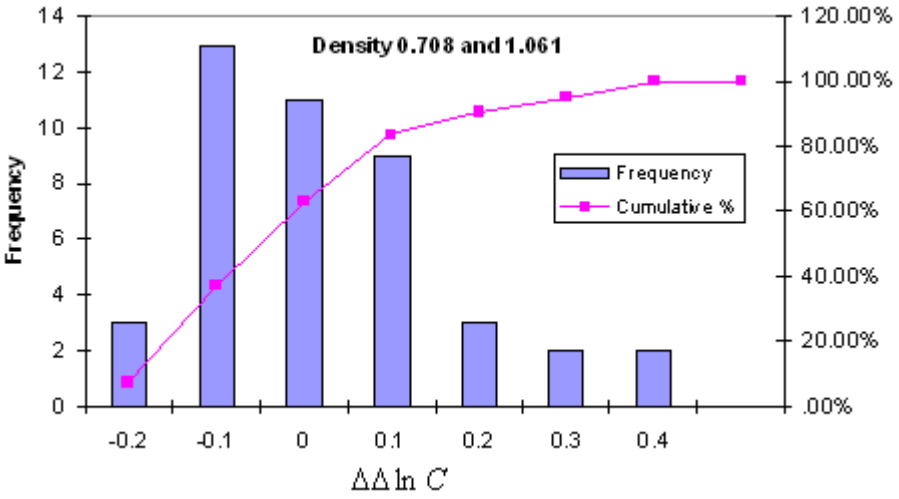

Fig. 5.5 (c) $\Delta \ln C$ variation $\Delta\Delta \ln C$ of 43 heads calculated at densities 0.708 and 0.1.061

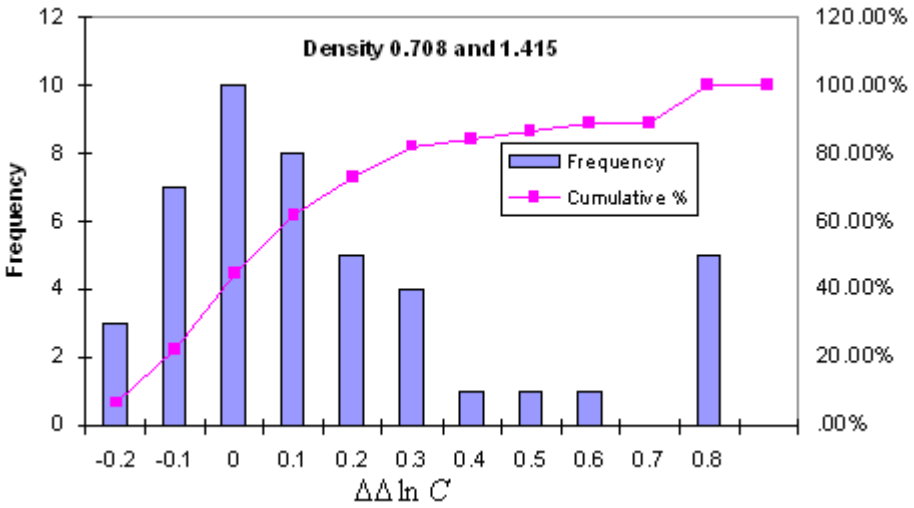

Fig. 5.5 (d) $\Delta \ln C$ variation $\Delta\Delta \ln C$ of 43 heads calculated at densities 0.708 and 1.415

The following observations can be made from the results illustrated in Fig. 5.5:

a) The distribution of $\Delta\Delta \ln C(\lambda_1, \lambda_2)$ of 43 heads becomes wider when the difference between the two densities becomes larger.

b) The histograms in Figs. 5.5(b), (c) and (d) are similar.

c) Histogram involving lower channel density, as the case illustrated in Fig. 5.5 (a), is somehow different from the rest histograms.

The observations also suggest that the testing repeatability is another important factor in selecting the two channel densities. The big difference between Fig. 5.5(a) and the rest is believed to be due to the channel density used in Fig. 5.5(a) which is only 0.354. According to the results presented in Chapter 4, a channel density of 0.354 is not high enough to secure testing repeatability and the resulting measurement error can not be ignored.

For verification, the histograms of the results with the density 0.566 as one of the two densities are plotted in Fig. 5.6.

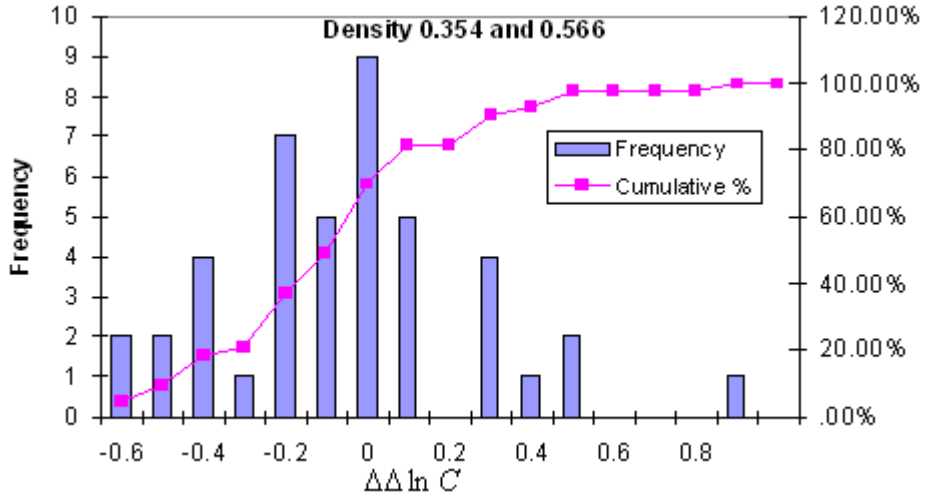

Fig. 5.6 (a) $\Delta \ln C$ variation $\Delta\Delta \ln C$ of 43 heads calculated at densities 0.354 and 0.566

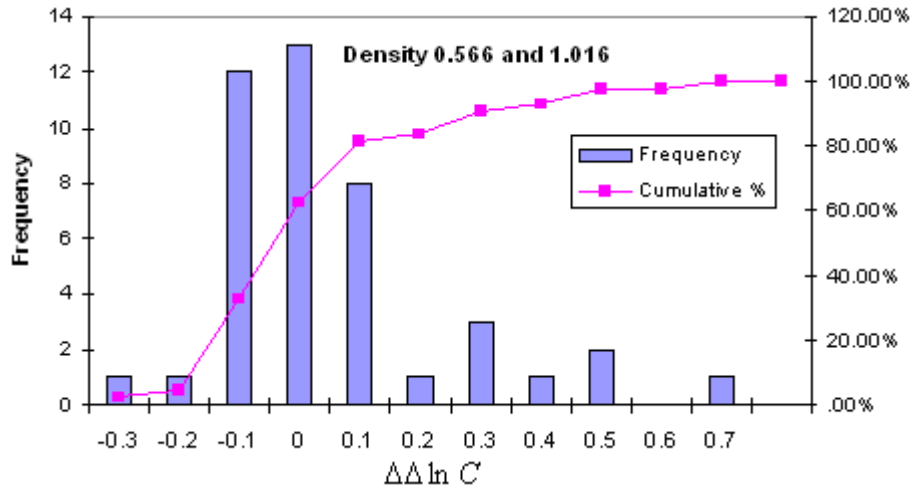

Fig. 5.6 (b) $\Delta \ln C$ variation $\Delta\Delta \ln C$ of 43 heads calculated at densities 0.566 and 1.016

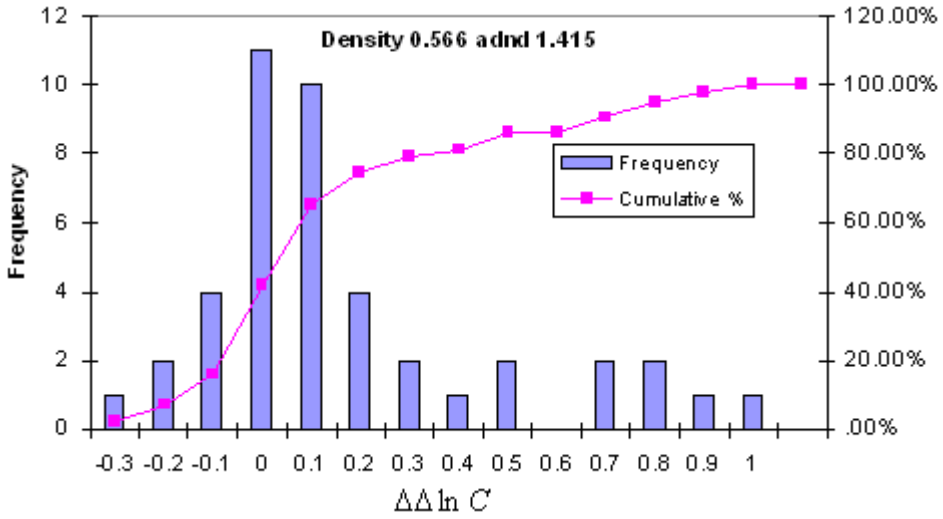

Fig. 5.6 (c) $\Delta \ln C$ variation $\Delta\Delta \ln C$ of 43 heads calculated at densities 0.566 and 1.415

Again, it could be seen that Fig. 5.6(a) shows different trend compared to the other two results, which has been explained with the low testing accuracy of density 0. 354.

5.2 Gap Length Variation Estimation

According to the above discussion, it is desirable if one can come up with a methodology to estimate the gap length deviation among different heads. Gap length itself is one of the most critical parameters of a head-media system. It would be of

great importance if one can come up with a methodology to estimate the gap length variation among different heads.

5.2.1 Motivation for Exploring New Methodology

Fig. 5.7(a) shows the typical structure of shielded multi-layer spin valve head, the most common head structure used in commercial disk drives [24]. The magnetization in the pinned layer is fixed in the transverse direction by exchange coupling with an antiferromagnetic layer. Only the magnetization in the sensing layer is allowed to respond to the magnetic field from the data storage media. The data retrieval resolution of spin-valve reading head is a function of the spacing between the shield layer and the free layer of the spin-valve head ---- the head gap length. Fig. 5.7(b) is the simple geometrical configuration used in readback signal modeling of shielded spin-valve head, where t is the thickness of sensing layer.

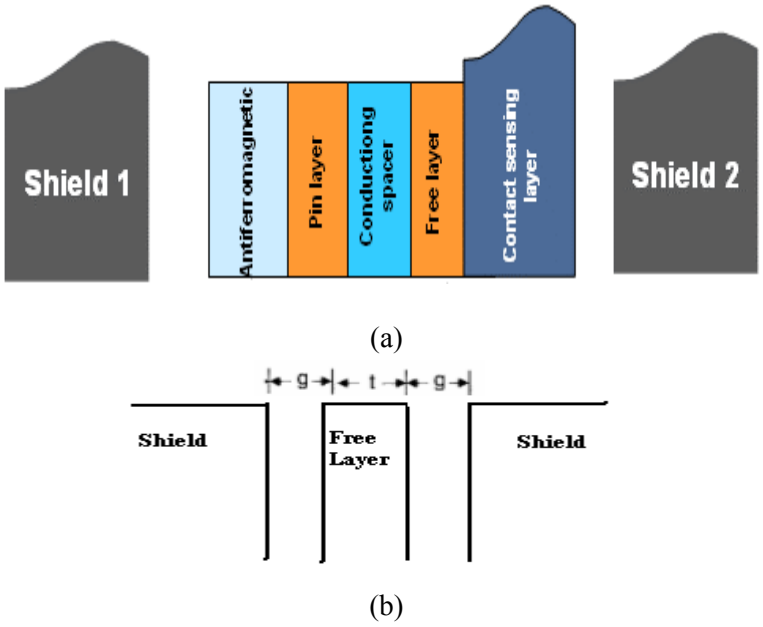

Fig. 5.7 (a) Structure and (b) geometrical scheme for the evaluation of gap length variation of typical spin valve reading head

In Chapter 3, we saw that variation of gap length has big influence on recording system performance. It is important to develop suitable methodology for the testing and evaluation of the gap length variation not only during head fabrication process (wafer level) but also at magnetic integration level (read/write testing level), since it is not easy to achieve sub-nanometer uniformity of multi-layered film stack with a thickness of 70~80 nm over a 5 inch or 8 inch wafer. However, little work is available in the public domain regarding how to experimentally evaluate the gap length variation at magnetic integration level. In previous arts, the gap length was evaluated by fitting a function of linear density to spectral measurements of the fundamental peak replay signal [17] [25]. Various analytical models were proposed including simple ones with Potter approximation, and more accurate ones which not only take the effects of shield gap length and MR element thickness into consideration, but also model the left-right asymmetry and base-line offset of the readback pulse by bringing in a small frequency independent phase shift [25]. The model in [25] matches the experimental data well but it requires knowing many system parameters in advance for curve fitting. In fact, parameters such as transition length parameter and fly-height are not easy to be known accurately in practical situations at head-disk integration level. It is therefore necessary to propose a new method that is easy to implement and require minimal system information.

5.2.2 Theory of the Methodology

The key for gap length variation estimation is to remove the effects caused by media thickness, head's fly-height and other factors.

Such estimation is achieved in this work by introducing a reference head so as to set a reference of gap length value and calculate the gap length difference between reference head and sample head. This is achieved by introducing a so-called 'G function', as described below.

Dual testing wavelength method is introduced to work with the reference head concept and eliminate the effects caused by the fly-height of those heads, media thickness, and other head-media system parameters in the gap length variation estimation. This is achieved by introducing a gap length variation function denoted 'GL'.

5.2.2.1 G Function and Gap Length Difference between Reference Head and Sample Head

The relationship between harmonic ratio of the triple harmonic method and the head disk interface parameters is as follows:

$$FH + \ln C = -\frac{3\lambda_3}{4\pi}\ln(\frac{V_3}{V_1}) \ . \tag{5.3}$$

Here, $\ln C$ is a function of both the head and media parameters including gap length g, free layer thickness t, magnetic thickness δ, transition parameter a, *etc,* and it varies with testing density. If we have a reference head with expected gap length and the relationship remains as

$$FH_0 + \ln C_0 = -\frac{3\lambda_3}{4\pi}\ln(\frac{V_{30}}{V_{10}}) \ , \tag{5.4}$$

given a reference head and a sample head, it should be possible to determine the gap length difference between the two heads if we could eliminate the other parameters' influence on harmonic ratio of readback signal.

In reality, the GMR element may not be in the center position between the two shields. The sensing layer thickness t may fluctuate among different heads. However, previous arts [25] suggest that the possible GMR element position offset and the GMR element thickness variation introduce negligible effect on the response function and pulse shape. Therefore, the geometrical scheme in Fig. 5.7(b) is suitable for theoretical analysis of gap length variation, and symmetry of the two gap lengths can be assumed.

All the system parameters used in the calculation correspond to those used in the experiment in Section 5.1. The nominal shield-to shield length is assumed as 75 nm, which includes a 3nm thick free layer.

A function G is defined as

$$G = \ln C - \ln C_0 \ . \tag{5.5}$$

The relationship among function G, gap length variation and channel density are illustrated in Figs. 5.8 and 5.9. The nominal gap length is set as 36nm. The readback signal is calculated with simplified conformal mapping model [21] of shielded MR head and tanh transition model.

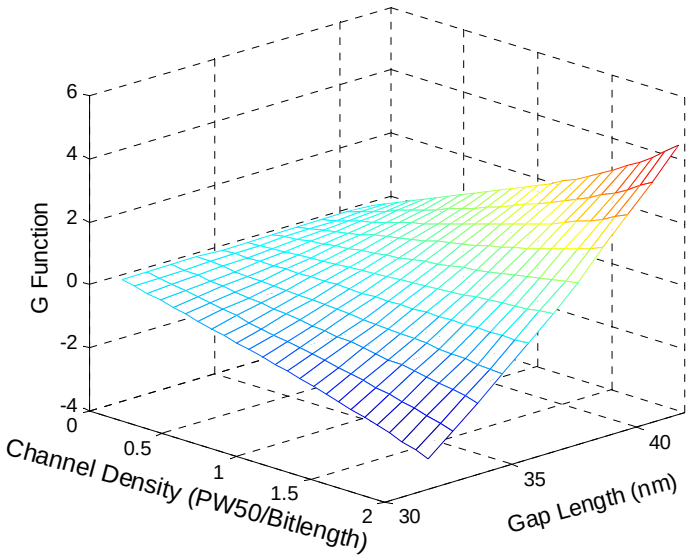

Fig. 5.8 Dependence of the function G on channel density and gap length variation

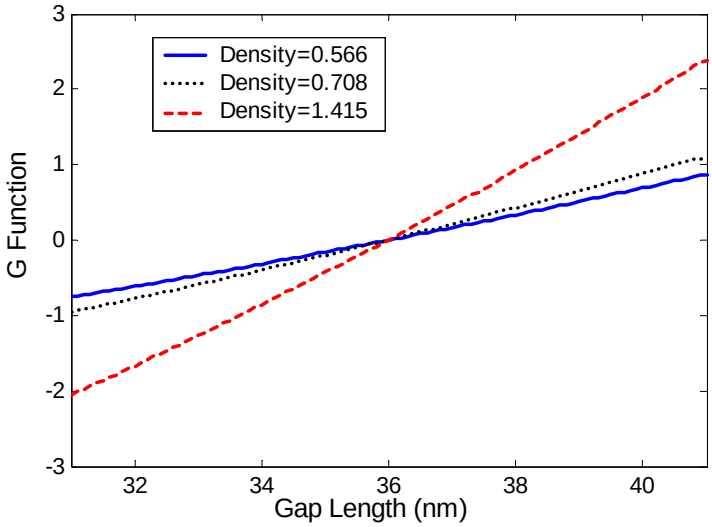

Fig. 5.9 Dependence of the function G on gap length variation at three densities

It is clear from Figs. 5.8 and 5.9 that the absolute value of *G* function increases as the gap length deviation increases. Also, higher channel density results in large slope of the *G* function, which is accordance with the fact that gap loss effect becomes more significant when channel density is high.

5.2.2.2 Gap Length Variation Function and Gap Length Estimation

A gap length variation function is defined to quantitatively study the gap length difference between the sample head and the reference head:

$$GL(\lambda_1,\lambda_2) = -\frac{3\lambda_1}{4\pi}\left[\ln(\frac{V_3}{V_1})\Big|_{\lambda 1} - \ln(\frac{V_{30}}{V_{10}})\Big|_{\lambda 1}\right] + \frac{3\lambda_2}{4\pi}\left[\ln(\frac{V_3}{V_1})\Big|_{\lambda 2} - \ln(\frac{V_{30}}{V_{10}})\Big|_{\lambda 2}\right] \quad (5.6)$$

where V_3 and V_1 are the amplitudes of the 3rd and 1st harmonics, respectively, of the sample head, and V_{30} and V_{10} are the 3rd and 1st harmonic signals, respectively, of the reference head. The analysis is carried out at two different bit densities and the corresponding fundamental harmonic wavelengths at those two bit densities are λ_1 and λ_2 ($\lambda_1 < \lambda_2$), respectively.

With the result of Fig. 5.9, *GL* function for three different combinations of recording densities are calculated and plotted as a function of gap length, as illustrated in Fig. 5.10.

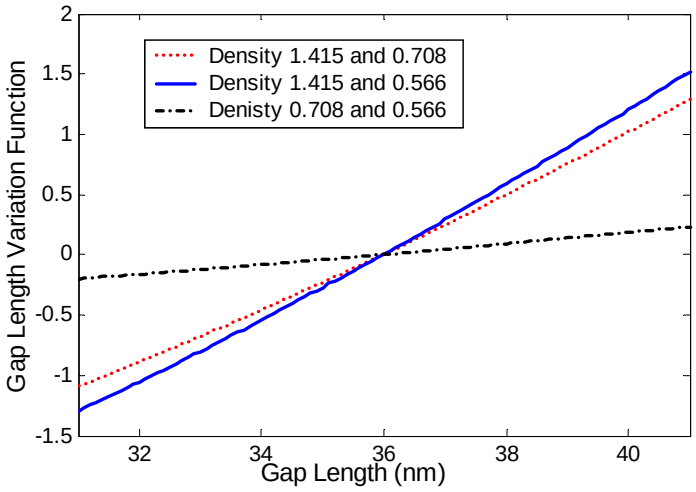

Fig. 5.10 *GL* function and its dependence on channel density and gap length variation (nominal value: 36nm)

It could be seen from Fig. 5.10 that the sensitivity of gap length variation function to the gap length variation differs obviously for different density combinations. The larger the difference between the two densities, the higher the sensitivity will be. As discussed in Chapter 4, the triple harmonic method has the advantage of having good accuracy and repeatability within a wide density range. Such an advantage can be used to estimate gap length difference between different heads.

Analytical form of Eq. (5.6) can be obtained with Potter's approximation formula (3.20) discussed in Chapter 3:

$$GL(\lambda_1,\lambda_2) = -(\frac{3\lambda_1}{4\pi})\ln\left[\frac{\sin(\frac{\pi(t+g)}{\lambda_1})\sin(\frac{\pi g}{\lambda_1})\sin(\frac{\pi(t+g_0)}{3\lambda_1})\sin(\frac{\pi g_0}{3\lambda_1})}{\sin(\frac{\pi(t+g)}{3\lambda_1}\sin(\frac{\pi g}{3\lambda_1})\sin(\frac{\pi(t+g_0)}{\lambda_1})\sin(\frac{\pi g_0}{\lambda_1}))}\right]$$

$$+(\frac{3\lambda_2}{4\pi})\ln\left[\frac{\sin(\frac{\pi(t+g)}{\lambda_2})\sin(\frac{\pi g}{\lambda_2})\sin(\frac{\pi(t+g_0)}{3\lambda_2})\sin(\frac{\pi g_0}{3\lambda_2})}{\sin(\frac{\pi(t+g)}{3\lambda_2}\sin(\frac{\pi g}{3\lambda_2})\sin(\frac{\pi(t+g_0)}{\lambda_2})\sin(\frac{\pi g_0}{\lambda_2}))}\right]. \quad (5.7)$$

It has been confirmed by other researchers [25] that the signal energy of modern spin-valve heads is largely concentrated within the range of the first gap null predicted by the Potter approximation. The energy would be very small after the first gap null frequency. Therefore, the difference between results from Eq. (5.7) and the accurate nonlinear potential model is very small and can hardly be noticed. Therefore, this simple linear model can be used for the estimation of the gap length variation with acceptable accuracy.

5.2.3 Experiment Results

The theory developed in Section 5.2.2 is implemented to estimate the gap length variation of 130 heads based on the experiment results presented in Section 5.1. Two groups of density combination, densities 1.415 and 0.708, and densities 1.415 and 0.566, are selected for gap length variation estimation considering both estimation sensitivity and testing repeatability.

Firstly, the gap length variation functions of the experimental results in Section 5.1 with the two density combinations are calculated and plotted in Fig. 5.11 and Fig. 5.13, respectively, based on (5.6). The reference head is selected after plotting the histogram. The selection of the reference is self defined as long as we could get reasonable gap length value, and the reference head selection will not affect the estimated gap variation within a batch of heads.

Secondly, the theoretical results of the gap length variation functions of the two density combinations are calculated with the nonlinear model, illustrated in Fig. 5.10, and are presented in Tables 5.2 and 5.3, respectively.

Thirdly, with the results of experimental gap length variation function, we could estimate the gap lengths of the 130 heads referring to the Tables 5.2 and 5.3 for the two combinations. The estimation results with the two density combinations are plotted in Fig. 5.12 and Fig. 5.14, respectively.

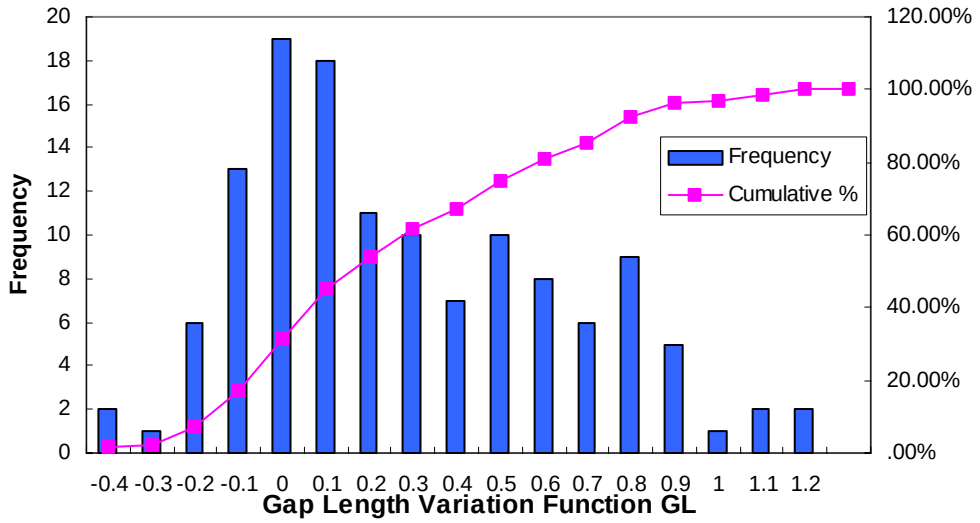

Fig. 5.11 Experimental gap length variation function for Densities 0.708 and 1.415

Gap Lenth (nm)	31.000	31.100	31.200	31.300	31.400	31.500	31.600	31.700	31.800	31.900
Gap Length Function	-1.094	-1.078	-1.062	-1.032	-1.016	-1.000	-0.969	-0.953	-0.936	-0.920
Gap Lenth (nm)	32.000	32.100	32.200	32.300	32.400	32.500	32.600	32.700	32.800	32.900
Gap Length Function	-0.888	-0.872	-0.855	-0.823	-0.806	-0.789	-0.772	-0.740	-0.723	-0.706
Gap Lenth (nm)	33.000	33.100	33.200	33.300	33.400	33.500	33.600	33.700	33.800	33.900
Gap Length Function	-0.673	-0.655	-0.638	-0.620	-0.587	-0.569	-0.551	-0.533	-0.499	-0.481
Gap Lenth (nm)	34.000	34.100	34.200	34.300	34.400	34.500	34.600	34.700	34.800	34.900
Gap Length Function	-0.463	-0.429	-0.411	-0.392	-0.374	-0.339	-0.320	-0.301	-0.283	-0.247
Gap Lenth (nm)	35.000	35.100	35.200	35.300	35.400	35.500	35.600	35.700	35.800	35.900
Gap Length Function	-0.228	-0.209	-0.190	-0.154	-0.134	-0.115	-0.096	-0.076	-0.039	-0.020
Gap Lenth (nm)	36.000	36.100	36.200	36.300	36.400	36.500	36.600	36.700	36.800	36.900
Gap Length Function	0.000	0.020	0.058	0.078	0.098	0.118	0.156	0.176	0.197	0.217
Gap Lenth (nm)	37.000	37.100	37.200	37.300	37.400	37.500	37.600	37.700	37.800	37.900
Gap Length Function	0.237	0.277	0.298	0.318	0.339	0.360	0.400	0.421	0.442	0.463
Gap Lenth (nm)	38.000	38.100	38.200	38.300	38.400	38.500	38.600	38.700	38.800	38.900
Gap Length Function	0.504	0.526	0.547	0.568	0.590	0.632	0.654	0.675	0.697	0.719
Gap Lenth (nm)	39.000	39.100	39.200	39.300	39.400	39.500	39.600	39.700	39.800	39.900
Gap Length Function	0.762	0.784	0.806	0.829	0.851	0.895	0.917	0.940	0.963	0.985
Gap Lenth (nm)	40	40.1	40.2	40.3	40.4	40.5	40.6	40.7	40.8	40.9
Gap Length Function	1.008042	1.053178	1.076159	1.099203	1.12231	1.145482	1.191611	1.215014	1.238481	1.262012

Table 5.2 Theoretical gap length variation function for densities 0.708 and 1.415

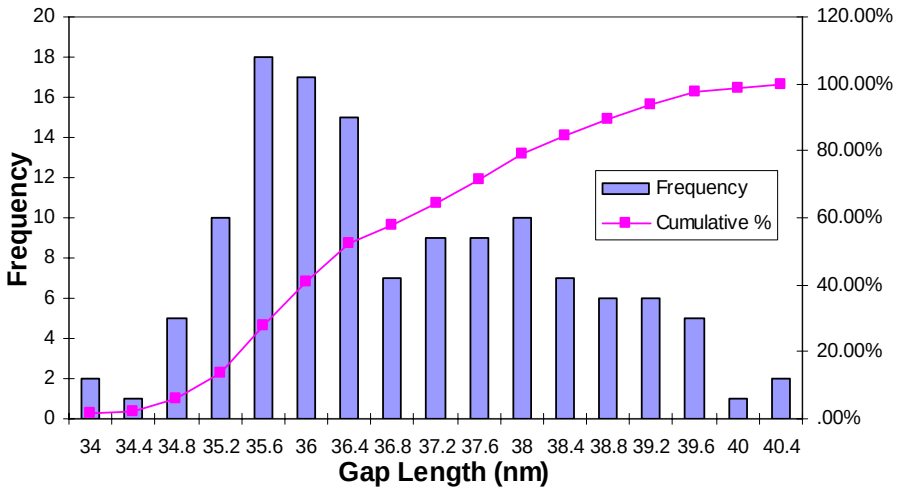

Fig. 5.12 Estimated gap length for densities 0.708 and 1.415

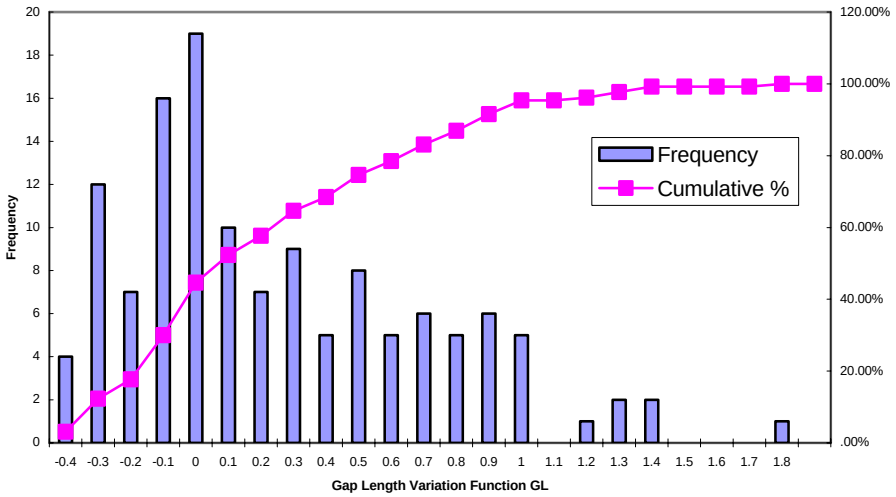

Fig. 5.13 Experimental gap length variation function for Densities 0.566 and 1.415

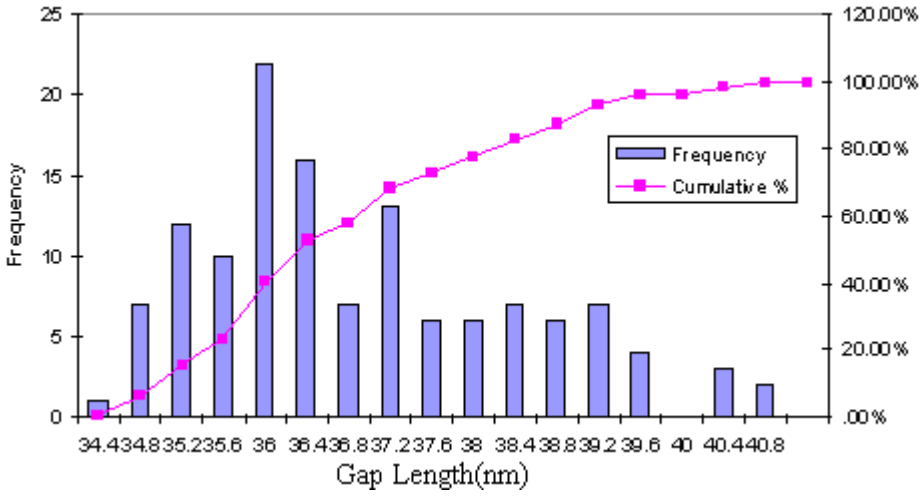

Fig. 5.14 Estimated gap length for densities 0.566 and 1.415

Gap Lenth (nm)	31.000	31.100	31.200	31.300	31.400	31.500	31.600	31.700	31.800	31.900
Gap Length Function	-1.295	-1.276	-1.257	-1.222	-1.202	-1.183	-1.147	-1.127	-1.108	-1.088
Gap Lenth (nm)	32.000	32.100	32.200	32.300	32.400	32.500	32.600	32.700	32.800	32.900
Gap Length Function	-1.051	-1.031	-1.012	-0.974	-0.954	-0.934	-0.914	-0.876	-0.855	-0.835
Gap Lenth (nm)	33.000	33.100	33.200	33.300	33.400	33.500	33.600	33.700	33.800	33.900
Gap Length Function	-0.796	-0.775	-0.754	-0.734	-0.694	-0.673	-0.652	-0.631	-0.591	-0.569
Gap Lenth (nm)	34.000	34.100	34.200	34.300	34.400	34.500	34.600	34.700	34.800	34.900
Gap Length Function	-0.548	-0.507	-0.485	-0.464	-0.442	-0.400	-0.378	-0.356	-0.334	-0.292
Gap Lenth (nm)	35.000	35.100	35.200	35.300	35.400	35.500	35.600	35.700	35.800	35.900
Gap Length Function	-0.270	-0.247	-0.225	-0.182	-0.159	-0.136	-0.113	-0.090	-0.046	-0.023
Gap Lenth (nm)	36.000	36.100	36.200	36.300	36.400	36.500	36.600	36.700	36.800	36.900
Gap Length Function	0.000	0.023	0.068	0.092	0.115	0.139	0.184	0.208	0.232	0.256
Gap Lenth (nm)	37.000	37.100	37.200	37.300	37.400	37.500	37.600	37.700	37.800	37.900
Gap Length Function	0.280	0.327	0.351	0.376	0.400	0.425	0.472	0.497	0.522	0.547
Gap Lenth (nm)	38.000	38.100	38.200	38.300	38.400	38.500	38.600	38.700	38.800	38.900
Gap Length Function	0.595	0.620	0.646	0.671	0.696	0.746	0.771	0.797	0.823	0.849
Gap Lenth (nm)	39.000	39.100	39.200	39.300	39.400	39.500	39.600	39.700	39.800	39.900
Gap Length Function	0.899	0.925	0.952	0.978	1.004	1.056	1.082	1.109	1.136	1.162
Gap Lenth (nm)	40.000	40.100	40.200	40.300	40.400	40.500	40.600	40.700	40.800	40.900
Gap Length Function	1.189	1.242	1.269	1.296	1.324	1.351	1.405	1.433	1.460	1.488

Table 5.3 Theoretical gap length variation function for densities 0.566 and 1.415

Comparing the gap length variation functions of the two recording density combinations in Figs. 5.11 and 5.13, we could see that even though there is a small difference in the shape of the distributions, the results are within comparable range. The results calculated with the density combination of 1.415 and 0.708 range from -0.5 to 1.1, and majority of the results for the density combination 1.415 and 0.566 range from -0.4 to 1.4, except the one around 1.8 which is believed to be due to measurement error (results related to this head will not be included in the rest of the discussion).

Observe from Fig. 5.15, 90% of the estimated gap lengths of the 129 heads vary from 34.5nm to 39.5nm, which is a reasonable range for a batch of heads with same design. Also, the two density combinations give similar histograms, as illustrated in Fig. 5.15.

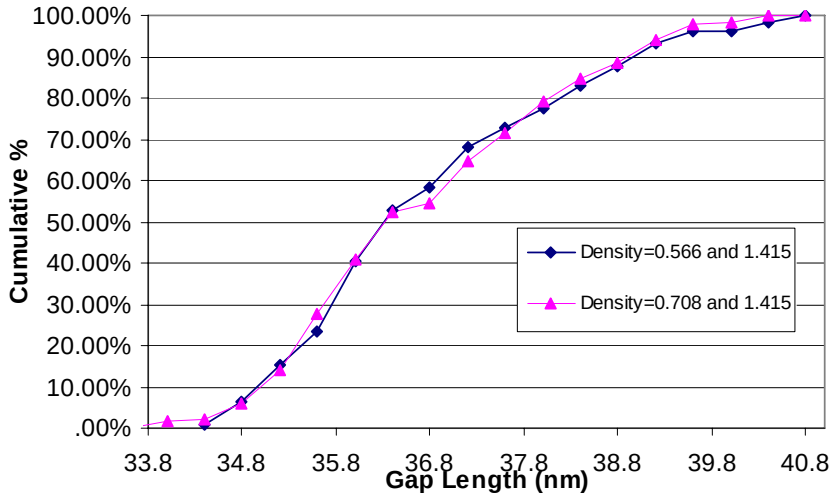

Fig. 5.15 Comparison of cumulative curves of estimated gap length at different density combinations (densityies 0.566 and 1.415, densities 0.708 and 1.415)

Therefore, it can be concluded that, with the method proposed in Section 5.2.2, the gap length variation within the same batch of heads can be estimated by testing the harmonic ratio $\ln(\frac{V_3}{V_1})$ of each head at selected testing density combination. The two channel densities should be high enough to secure the testing repeatability. Also, the difference between the two densities should be large enough to provide high sensitivity for gap length estimation.

5.3 Summary

A novel method for the estimation of gap length difference among different heads is proposed. The method works at head-gimbal assembly level, and it can effectively evaluate the gap length variation of a batch of heads with similar design. The testing process is easy to implement. The testing sensitivity and accuracy are high with correct choice of the density combination.

Chapter 6
High Density Recording and Nonlinearity Effect

In this chapter, the challenges and problems faced in high density and high data rate recording are discussed and their effects on readback signal and triple harmonic method are studied experimentally and theoretically. Firstly, the channel response effect was observed and its effect on high-density recording with high writing frequency was discussed. Secondly, nonlinearities like nonlinear transition shift, hard transition shift cause the output readback signal to deviate from that predicted by the principle of linear superposition, therefore affect the harmonic based fly-height testing. Thirdly, the nonlinear transition shift effect is discovered to be more evident in high data rate recording because of the finite field rising effect.

6.1. Performance Analysis at High Recording Density

Two factors are important for the analysis of high density magnetic recording systems. The first is frequency response of the channel and how to compensate channel frequency response effect so as to make sure the testing accuracy. The second is nonlinearity effects at high density. This section discusses frequency response effect and compensation technology. The nonlinearity effect will be discussed in Sections 6.2 and 6.3.

High recording frequency is a possible choice in order to achieve high recording density and high data transfer rate.

We have to characterize the channel response of the system and determine the bandwidth limit of the replay amplifier and channel as they influence the testing results as seen in Eq. (2.11) in Chapter 2.

The gain and bandwidth of the replay channel were measured by injecting a sinusoidal signal in the range of 1 – 230MHz into a special head calibrator board. The board converts the single-ended signal from the signal generator to a differential signal with the level of the signal attenuated to be comparable with the signal that head senses from disk, and could be injected to the input of the head amplifier. We then measure the peak-to-peak output signal at different frequencies using a digital signal oscilloscope. The peak-to-peak value of the input sine wave signal was also measured at the output of the signal generator to allow for drift in the input signal. Fig. 6.1 illustrates the measured voltage gain in decibels determined using the Guzik head calibrator board. It could be seen that the –3dB corner frequency is approximately at 200MHz.

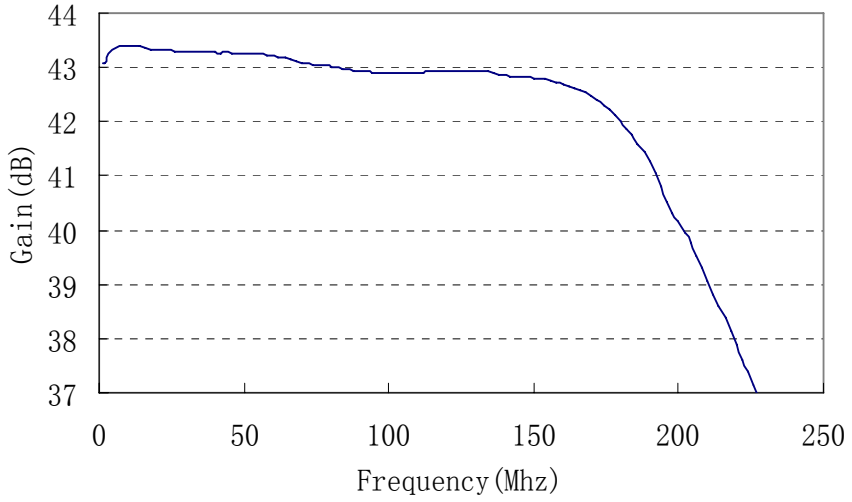

Fig. 6.1 Frequency response of the readback channel

Fig. 6.1 shows that the amplifier gain of the readback channel is not flat above 160 MHz and the –3dB corner frequency is approximately at 200MHz. As seen in Table 6.1, with the fixed radius 1.216inch, the writing frequency must be higher for higher velocity case to achieve the same linear density.

	Writing frequency (MHz)						
RPM 8000	72	96	120	144	168	192	216
RPM 6000	54	72	90	108	126	144	162
Density (kfci)	152.7	203.5	254.4	305.3	356.2	407.1	458

Table 6.1 The writing frequency (MHz) at different RPM for certain linear density

Since the accuracy of the test result is proportional to the intensity of the readback signal, we must make sure that the writing frequency should be within the range of high enough gain in Fig. 6.1. But since high linear density is needed to achieve fly-height testing sensitivity, thus, high frequency will be necessary.

With the harmonic ratio tested at two velocities, we get $\ln(\frac{V_3}{V_1})$ and $\ln(\frac{V_{30}}{V_{10}})$, and we could calculate the fly-height change of the slider flying at these two velocities with Eq. (6.1). The difference in the harmonic ratio reflects the change in effective magnetic spacing at these two velocities. Since the amplifier gain of the channel is not a constant at different frequencies, we need to eliminate the difference of the gain at the two frequencies of V_3 and V_1, according to the channel response illustrated in Fig. 6.1. The calculated results without and with compensation of channel response are illustrated in Fig. 6.2 and Fig. 6.3.

$$\Delta(d+a) = -\frac{3\lambda}{4\pi}\left[\ln\left(\frac{V_3}{V_1}\right) - \ln\left(\frac{V_{30}}{V_{10}}\right)\right] \tag{6.1}$$

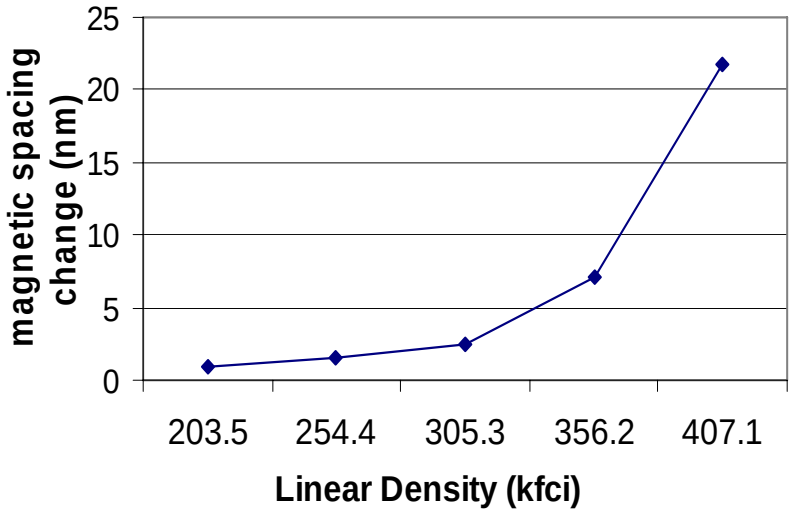

Fig. 6.2 Effective magnetic spacing change (nm) without compensation of channel response

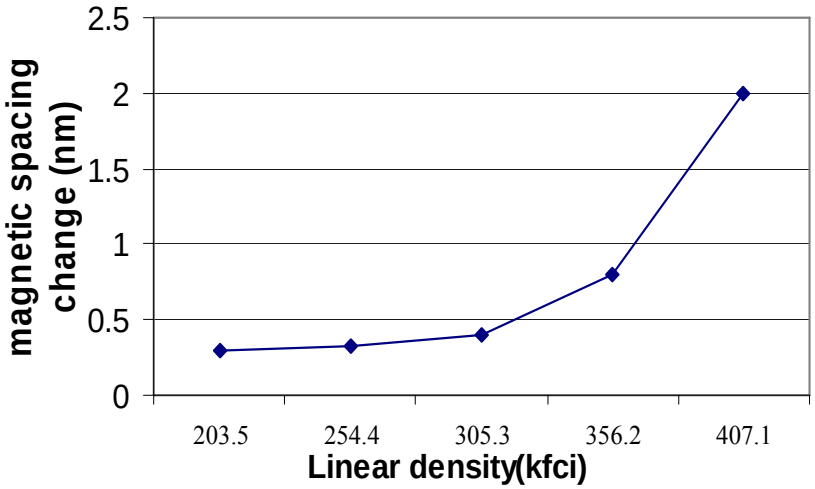

Fig. 6.3 Effective spacing change (nm) with compensation of channel response

Firstly, it is noted that in high frequency range, the degradation of the gain influences the results a lot and compensation is necessary. Secondly, it is found that the measured magnetic spacing change is not a constant at different linear density, though the difference should be a constant. It can be further noticed that in the low density range the effective spacing change of Fig. 6.3 almost remains constant and reflects that the fly-height difference at these two velocities is quite small.

The difference starts to increase once the density reaches certain value. Since the fly-height change should be a constant and should not vary with writing density, the increase appearing in Fig. 6.3 is believed to be due to the variation of transition parameter change in the high density and high recording frequency region.

To preserve linearity, it was assumed that the transition length is a constant at different densities in the previous chapter. However, the agreement between the measured and theoretical signal roll-off curves dictated an increase in the transition width parameter with the increase in density [13]. As transitions are written closer, it is expected that the slope of a newly written transitions will be influenced by the neighboring transition's demagnetizing fields in addition to the writing head field. This is enhanced by the increase in transition length of individual transitions at high densities due to partial erasure [26]. The results in Fig. 6.3 suggest that the transition parameter at 8000 RPM increases faster with the increase of density than that at 6000 RPM in high density region.

6.2 Nonlinearity at High Bit Density and Its Effects on Accuracy of In-Situ Flying Height Analysis

6.2.1 Nonlinearity at High Linear Density Recording

As discussed in Chapter 3, the linear superposition principle is valid when the channel density is low and it is acceptable to predict the playback signal from a sequence of transitions by summing the output of isolated readback pulses. However, nonlinear interactions between magnetic transitions are no more negligible when the channel density is high and such interactions result in nonlinear distortions of readback signal.

The nonlinear distortions include the nonlinear amplitude loss and the nonlinear transition shift. Those non-linearities are due to the interaction between the writing head field and the demagnetization fields from the adjacent transitions in the vicinity, and lead to proximity-effect induced transition shift. When a transition is recorded on the magnetic medium, a demagnetization field $H_{ext}(x)$ is added to the head field $H_h(x)$, expanding or shrinking the write bubble [27] and causing the present transition to be recorded at a location different from the "expected" location x_0. The writing occurs when $H_h(x) + H_{ext}(x) = H_c$, where $H_h(x)$ is the magnetic field of the writing head and H_c is the media coercivity. The net transition shift is calculated as

$$\Delta = -\frac{H_{ext}(x)}{dH_h / dx \mid_{x=x0}} \tag{6.2}$$

where x_0 is the transition location. There are two principal sources of proximity shift. The first source comes from the downstream transitions from old data patterns that are not yet erased by the write field of the recording head, which is referred to as the inter-pattern effect that leads to hard transition shift (HTS). The second source comes from the upstream transitions, which are the newly formed transitions just being written by the recording head, and this types of effect is referred to as the intra-pattern effect which leads to nonlinear transition shift (NLTS) [27] [28].

6.2.2 Interactions between NLTS and HTS

6.2.2.1 Transition Shift over AC Erased Track

The harmonic analysis presented in this work is based on 111100 pattern, with each "1" representing a magnetic transition. The location of the transitions may be affected

by the nonlinearity effected mentioned above.

Consider a series of transitions written on the AC erased medium. The demagnetization field from previous transitions expands the write bubble and result in an early written transition with nonlinear transition shift Δ. The amount of the transition shift is a function of the proximity of the preceding transitions to the transition to be formed. The function is defined as N ().

For a string of transitions, the first transition will not be affected by NLTS as no transition is there before this transition. The second transition will be shifted by $\Delta_2 = N(B_0)$, where B_0 is the nominal bit period. When the third transition is written, the demagnetization fields from both previous transitions add to the head field and the third transition is shifted by $\Delta_3 = N(B_0 + \Delta_2) - N(2B_0)$. The third transition will be shifted by a less amount than the second for two reasons. First, the demagnetization field from the second transition is partially cancelled by the opposing demagnetizing field from the first transition. Second, the NLTS of the second transition makes it further away from position of the expected new transition. Therefore, the intensity of the demagnetization field from the 2nd transition is reduced and so is the amount of transition shift caused by the 2nd transition.

6.2.2.2 Transition Shift over DC Erased Track

Consider a series of transitions written on the DC erased disk. In this case, the transitions formed by head field bubble against the DC erased media magnetization are considered ‘hard’ and transitions formed by head field bubble in a direction same as

media DC magnetization are ‘easy’. When a hard transition is written, a secondary writing zone is formed on the leading edge of the head write bubble. The demagnetization field from this secondary write zone shrinks the write bubble, and thus distorts and delays the transition written on the trailing edge of the write bubble, resulting in hard transition shift. When a train of transitions is written, each hard transition is affected both by NLTS and hard transition shift. Easy transitions are directly affected by NLTS only, but are also indirectly affected by HTS because changes in the position of hard transitions affect the NLTS of easy transitions. As a result, every second transition in a train of transitions will experience smaller net transition shift due to HTS while the effect of it is amplified by NLTS. When the first transition in a train is hard, the HTS and the oscillation of NLTS reinforce each other. When the first transition in a train is easy, the HTS and the oscillation of NLTS partially cancel each other. The transition shift for MR head with different initial medium magnetization has been measured by Taratorin [28] as in Fig. 6.4, where the first transition in the series is ‘hard’ for positively magnetized medium.

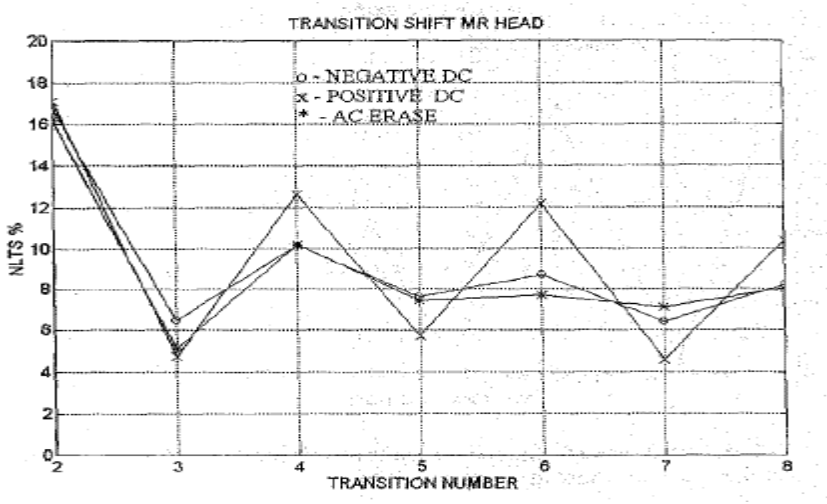

Fig. 6.4 Measured transition shift for MR head with different initial medium magnetization

6.2.3 Effect on Triple Harmonic Pattern

6.2.3.1 Transition Shift and All "1" Pattern

In a long square wave pattern (such as all "1" pattern), each transition will be shifted by the same amount of NLTS toward the previous traditions if the medium is effectively AC-erased prior to writing the square wave. If the medium is DC erased, the oscillation of the transition shift converges to the same steady level for both directions of the initial medium magnetization in a long train of transitions.

6.2.3.2 Transition Shift and Triple Harmonic Pattern

If a pattern containing relatively short sequences of consecutive transitions is written, the problem of interactions between NLTS and HTS becomes obvious in high-density recording and leads to complicated shift values for individual transitions in the pattern. For the pattern 111100 used in triple harmonic fly-height testing method, those nonlinear effects in the high density will make the waveform different from the waveform obtained by linear superposition. As a result, the harmonic intensity will be affected. Therefore, the nonlinear effect on testing result should be taken into consideration in harmonic analysis based on triple harmonic code. Referring to the NLTS value in Fig. 6.4, we simulate the waveform of the pattern 111100 and calculate its harmonic ratio with different erasing methods and by linear superposition, as in Fig. 6.5 and Table 6.2. The NLTS percentages of the second, third, and fourth transitions in pattern 111100 are listed in Table 6.2 referring to the NLTS value in Fig. 6.4. All the harmonic intensities have been normalized with the V_3 of linear superposition. The linear density here is 430kfci, and the first transition in the series is 'hard' for positively magnetized medium.

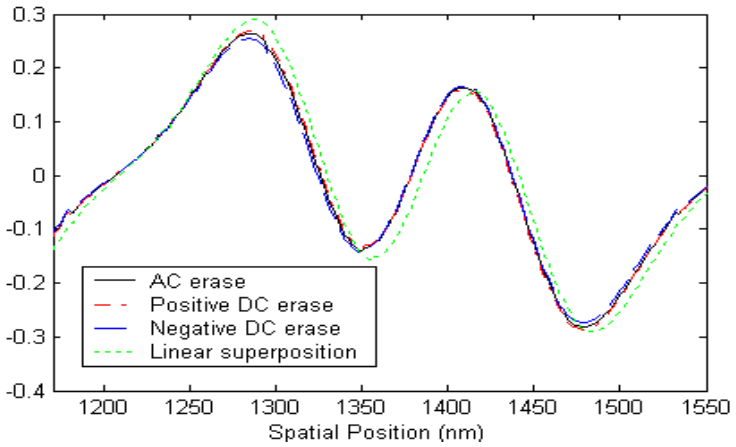

Fig. 6.5 Waveform with different erasing methods and linear superposition

	NLTS (%)	V_3	V_1	V_3 / V_1	$\ln(\frac{V_3}{V_1})$
Linear		1	1.446535	0.691307	-0.36917
Positive DC	(18,3,12)	0.976084	1.297334	0.770812	-0.26031
Negative DC	(12,7,10)	0.989797	1.409055	0.709696	-0.34292
AC	(14,5,10)	0.98685	1.361399	0.734538	-0.30851

Table 6.2 Illustration of nonlinearity effect on pattern 111100 with different erasing methods

The simulation result suggests that the variation of third harmonic, caused by NLTS effect, is quite small. On the other hand, the first harmonic is much more sensitive to the NLTS effect and NLTS leads to reduced first harmonic amplitude. From Table 6.2 we can see that the difference of positive DC erase and negative DC erase due to the effect of hard transition shift is obvious, and if the first transition happens to be hard the NLTS and HTS will enforce each other to make the $\ln(\frac{V_3}{V_1})$ becomes bigger than its value of that when the nonlinearity is negligible.

6.2.4 Enforced Nonlinearity Effect at High Data Rate Recording

The NLTS values were measured using spectral elimination method [30] at three RPM as a function of the linear density after applying the inverse MR transfer function. The transfer function of the MR read element was first measured using algorithm described in [30]. The radius is fixed at 1.216 inch of a 3.5” disk with magnetic moment of 0.37

$memu/cm^2$ and coercivity of 4150 Oe. The read bias current is selected as 3mA and the write current is set as 40mA, after optimization process based on saturation test. The writing data frequency is varied in proportion with the speed of disk rotation to keep recording density constant. The fly-height variation at the three velocities is trivial verified with commercial dynamic fly-height tester (DFHT) with optical FH measurement method.

Experimental data are illustrated in Fig. 6.6. The NLTS is of a rather constant value independent of medium velocity and recording frequency, when the recording density is not high. One thing interesting is that the data measured at different RPM is different, though the density remains the same. The higher the spindle speed, the lower the turning point density from which the NLTS starts to increase steadily. Furthermore, the higher the spindle speed is, the higher the measured NLTS value. As the bit density is same, the above mentioned difference must come from the rise time of the head field which has different rise time for different spindle speeds [33].

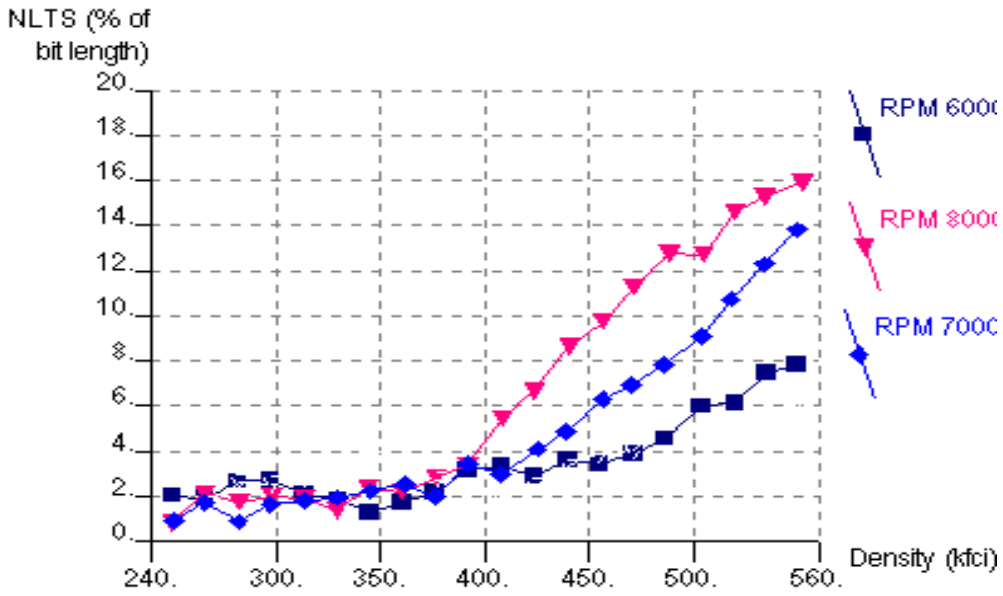

Fig. 6.6 NLTS as a function of linear recording density at various medium velocities

Fig. 6.6 suggests that NLTS is not only related to medium magnetic properties but also related to disk velocity at high data rate recording. To achieve high data rate recording, high disk rotating speed may be preferred for the same linear density, but extra factors may contribute to the nonlinearity at higher velocities. This is due to the finite rise time of the write current which arises primarily due to three reasons [33]: First, the write driver itself has a finite switching time; Second, the inductance of the head and the electrical connections further increase the rise time of the current delivered to the head; Third, eddy current field of the conductive head material causes head efficiency drop with frequency. As the writing frequency increases, the normalized rise time of the head field becomes large. Therefore, when a transition is written, the field direction may be switched before the saturation state is achieved and resulting in "early" shift of the transition, similar to the effect of NLTS. Once the τ_{10-90}, defined as time length between 10% and 90% of write field arises, is larger than the passing time over one bit, the NLTS degrades significantly.

Consider writing a dibit transition at nominal separation of B_0 and an additional timing shift τ of the second transition is introduced due to the finite flux rise time, the total NLTS of the second transition is given as [29]

$$\Delta = V\tau(B_0 / ve) - \frac{H_d(B_0 - V\tau(B_0 / ve))}{dH_h / dx\big|_{x=x0}} \tag{6.3}$$

where *ve* is the medium velocity and the timing shift will be reinforced by the demagnetization field H_d at high density. Note that τ is a function of the distance between adjacent transitions and it increases for smaller bit period. Therefore, with the same density, the transition shift increases with increase in data rate since the timing shift increases at higher velocity.

An additional factor should be considered at high recording frequency is that theoretical calculations [32] [34] based on small gap theory predict that the short flux rise time reduces the head filed gradient and results in a broader transition as below:

$$a = \sqrt{(\frac{M_r d\delta}{\pi H_c} * \frac{1+(veT/d)^2}{2(veT/d)})} \qquad veT > d \tag{6.4}$$

where T is the field rise time. Observe from (6.4) that a non-zero flux rise time affects the recording process more severely for a higher ve, a larger T, and a smaller d. Furthermore, it could be seen from (6.3) that the reduction of the field gradient will cause an additional increase in the transition shift.

In a series of transitions written on the medium, the oscillations of transition shift caused by nonlinearity effects in Fig. 6.4 are reinforced by the timing shifts, and the NLTS of a series of transitions is more evident than that of the dibit transition pairs [35]. Furthermore, both the intensity of the NLTS itself and its oscillation will be stronger at higher data rate recording with the same high recording density.

6.3 Fly-Height Testing in High Linear Density and High Data Rate Recording

With the aim to study the nonlinear transition shift effect on accuracy of triple harmonic fly-height testing method, the medium was positive DC erased or negative DC erased before the pattern 111100 was written. Then, first and third harmonics of readback signal are tested with the experiment apparatus in Chapter 4. The

experimental conditions are same as that in Fig. 6.3.

The power spectrum of V_3 and V_1 tested at 6000 RPM are plotted in Fig. 6.7. It is interesting to notice that the first harmonic signal V_1 can be affected by the current direction of the above mentioned DC erase, though the third harmonic signal V_3 is not that sensitive to the direction of the DC erasing current. The V_1 amplitude difference from different directions of DC erasing current indicates the existence of nonlinearity induced interference in the in-situ fly-height analysis of the triple harmonic method. The phenomenon can be explained as follows. The combined effect of hard transition shift and NLTS will cause transition shift of the two "1"s next to the "00" in the "111100" data pattern, and affects the 1st harmonic signal, especially at high densities.

With the theoretical analysis presented in the Sections 6.2.2 and 6.2.3, and the simulation data listed in Table 6.2, we can conclude that, for the negative DC erased track, the first transition in the 111100 pattern is a hard transition. The transitions experience more serious nonlinearity effect than that on a positively DC erased track case which has an easy transition as the first transition in the 111100 pattern. The hard transition shift enforces NLTS in the negative DC erase case and leads to bigger NLTS oscillation between individual transitions.

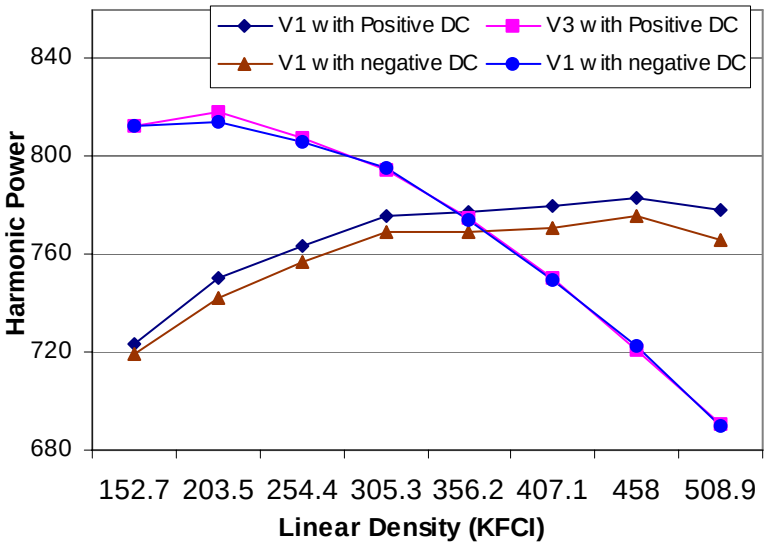

Fig. 6.7 Harmonic Power (dB) of V_3 and V_1 tested at 6000 RPM with different erasing methods

The harmonic ratio $\ln(\frac{V_3}{V_1})$ at 8000 RPM and 6000 RPM with the two erase methods are plotted against linear density in Fig. 6.8 and Fig. 6.9, respectively. The results suggest that the $\ln(\frac{V_3}{V_1})$ with the negative DC erase method has larger value than that with the positive DC erase, and will lead to underestimated fly-height.

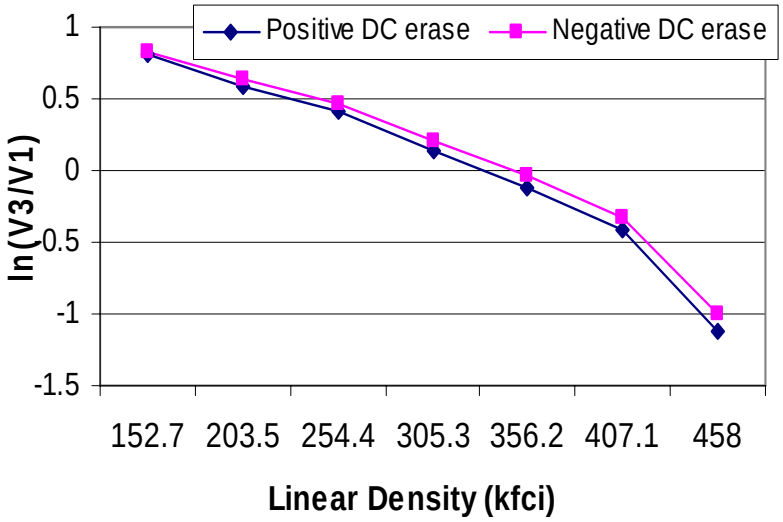

Fig. 6.8 Harmonic ratios with different DC erase methods at 8000RPM

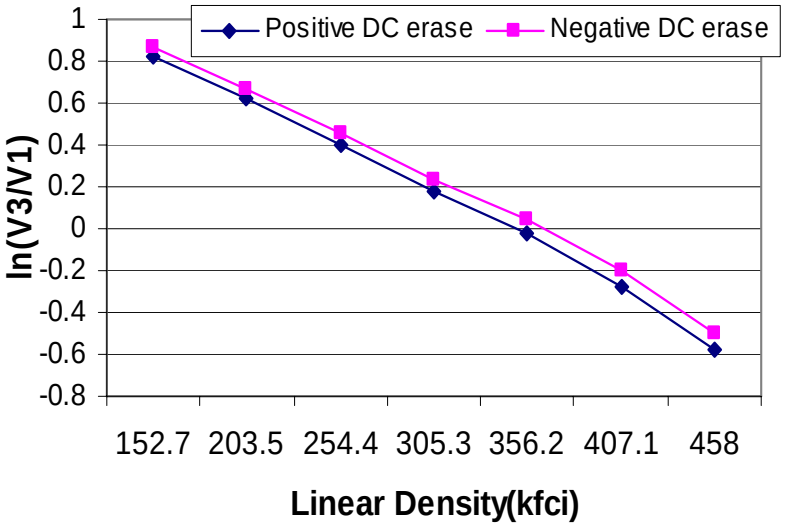

Fig. 6.9 Harmonic ratios with different DC erase methods at 6000RPM

As can be observed from Fig. 6.8 and Fig. 6.9, the limited bandwidth of the channel makes the data of 458kfci density tested at 8000 RPM seriously affected by the degradation of the amplifier gain, while the data of 6000 RPM with lower writing frequency has not been affected that much.

As Fig. 6.10 shows, the $\ln(\frac{V_3}{V_1})$ differences with the two erase methods show different trend in the high linear density region. Same transition density at two different disk speeds was realized by adjusting the writing frequency. The two curves almost overlap when the transition density is not high. However, the difference between the two curves increases as the transition density is increased. This corresponds to the result in Fig. 6.6 that NLTS is much more severe at the high velocity 8000 RPM than the velocity 6000 RPM, in the high linear density region. As discussed and concluded before, such phenomenon is believed to be due to the effect of the nonzero rise time of the writing field at high writing frequency.

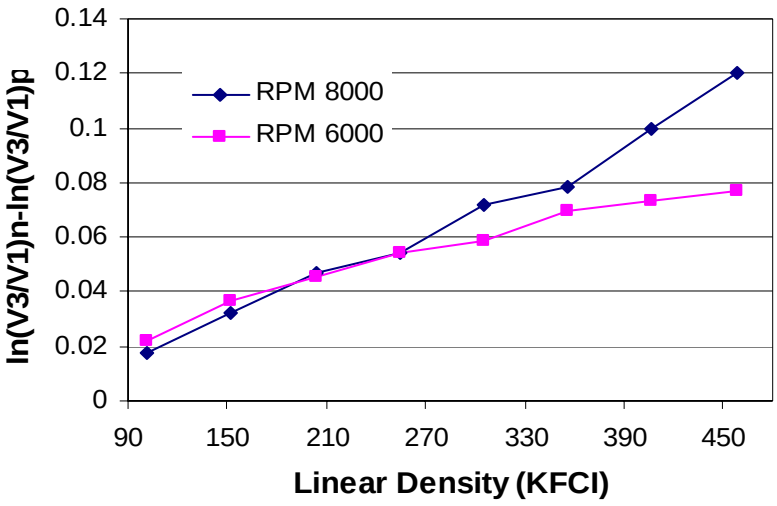

Fig. 6.10 Differences in the harmonic ratio between the two erase methods at two disk speeds

6.4 Summary

From the theory and experiments in this section we could conclude that the factors that affect triple harmonic fly-height testing method at high density and high data rate recording are as follows.

Firstly, the channel response limits the achievable working frequency and the testing result should be carefully compensated with the channel response especially in the high frequency region to guarantee high accuracy. Secondly, the nonlinear transition shift affects the testing result in the high-density region, and the phenomena will be more evident when hard transition shift enforces NLTS and leads to bigger NLTS oscillation between individual transitions. Thirdly, the nonlinear transition shift effect will be more evident in high data rate recording because of the finite rise time effect of the write field. Furthermore, transition parameter is increased in the high density and high recording frequency region.

The above factors affect the accuracy of the triple harmonic method in high density and high data rate recording. But since high density is required to assure high testing sensitivity, we need to compromise the accuracy and sensitivity because of the increasing demand for density and data rate in magnetic recording systems.

Chapter 7

Nonlinearity in Track Direction and Its Effects on Fly-Height Analysis

Improving the track density becomes a crucial challenge since track width and head dimensions are required to decrease continuously. Because the servo required to position the head accurately at the track center becomes more difficult with decreasing track width, the behavior of the device with off-track displacement is also of interest and the playback signal response in the cross-track direction needs to be characterized. Furthermore, track-edge recording phenomena becomes very important with small track width since heads are likely to pick up the data at track-edge, and also the high recording density makes the track-edge effect more obvious due to partial erasure. In this chapter, firstly the behavior of the device with off-track displacement is observed in experiment; secondly the recording physics underlying this phenomenon are studied, and is then utilized in a more accurate simulation model to study the issue.

7.1 Experiments in Track Direction

7.1.1 Cross-track Profile

For the same track, the readback signal can be different if the head is positioned at different radius positions of the track. This section investigates the effect of off-track position on fly-height measurement.

Firstly, experiment has been done to study the cross-track property of playback signal. We define 'positive off-track displacement' to indicate the movement of the head to the outer track direction respect to the written track below it, and 'negative off-track displacement' to indicate the head movement to the inner track direction. The slider used in this experiment has a fly-height about 15nm at velocity of 5000rpm. Its ABS is scanned with optical microscope and ZYGO microscope, and is plotted in Fig. 7.1 as below.

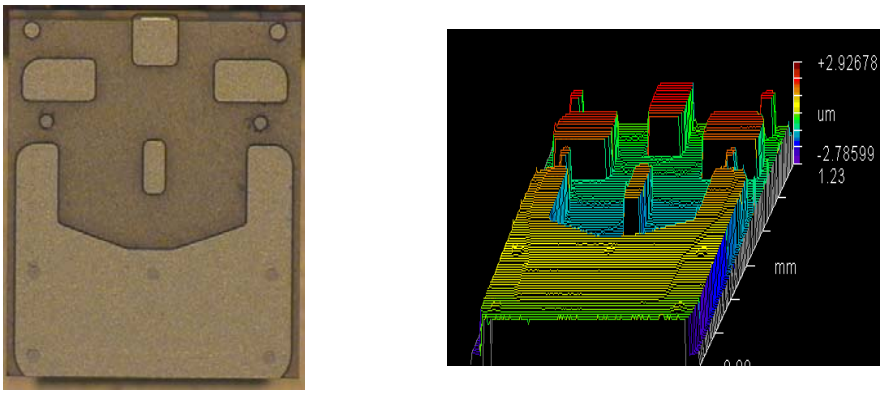

(a) (b)

Fig. 7.1 ABS design (a) optical microscope image and (b) ZYGO microscope image of the slider used in the experiment

From the track profile we know that the write width is about 10.5uin and read width is about 6.6uinch. The 111100 patterns are recorded on the media at a proper user density (around 1.0) and the readback signal at every cross-track position is tested. We plotted the cross-track profile of the logarithm amplitude ratios of the first and third harmonics and the cross-track profile of track average amplitude (TAA) in Fig. 7.2 with different scales, and found the tested harmonic ratio cross-track profile is much less sensitive to off-track displacement than the signal amplitude cross-track profile (TAA). So, we say that the proposed method has good off-track tolerance.

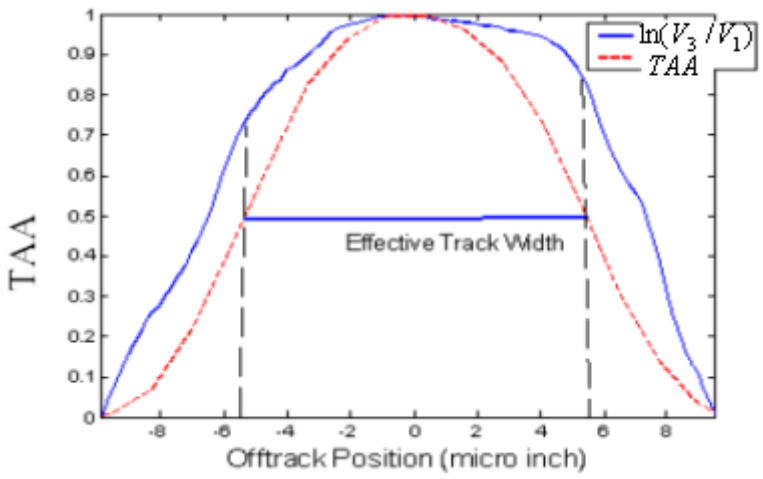

Fig. 7.2 Harmonic ratio cross-track profile and the signal amplitude cross-track profile.

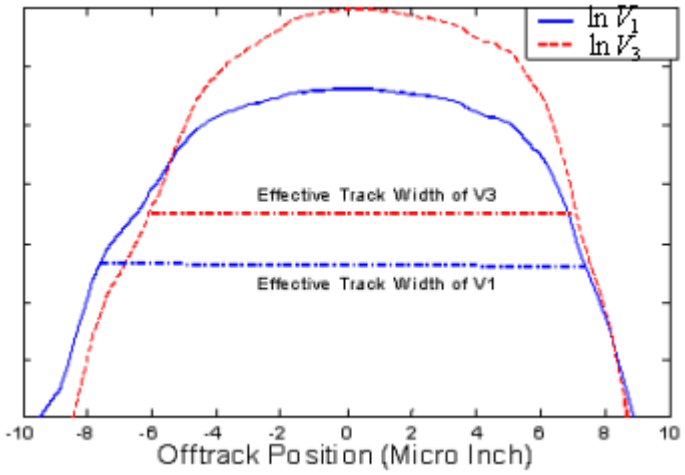

Fig. 7.3 Cross-track profile of the different harmonic densities

We plot the harmonic intensities in Fig. 7.3. From Figs. 7.2 and 7.3, it can be observed that both the harmonic intensity and the corresponding logarithm harmonic ratio decrease with the increase of the amount of off-track from the track center. The cross-track profiles of different harmonics are different. The high frequency harmonic of the playback signal tends to decrease more quickly with off-track displacement and shows smaller effective track width. This could be explained as follows. Since the gradient of the writing head field decreases greatly at the track-edge, it becomes much harder to write high frequency signal on the track while the low frequency parts of the signal are

less affected compared to the on-track situation. Furthermore, the increase in asymmetry of the shape of the readback signal with the increase of off-track displacement also causes further decrease in the intensity of high frequency harmonics.

7.1.2 Track-edge Effect at High Density

For further study, with a fixed velocity at 5000 RPM, we repeated the experiment in Section 7.1.1 at two recording frequencies: 120Mhz and 90Mhz at 1.126inch radius of a 3.5inch. The waveforms of triple harmonic method recorded at these two densities tested at track center are plotted in Fig. 7.4.

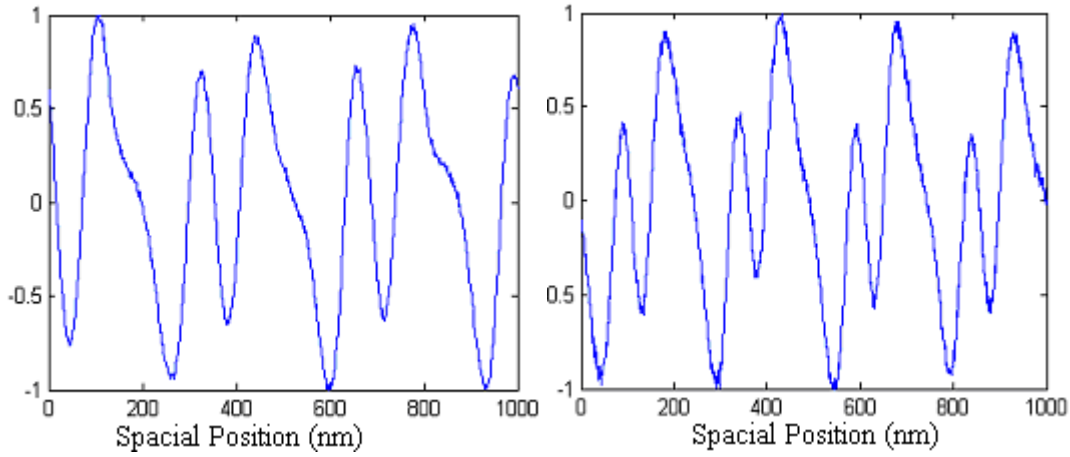

Fig. 7.4 Waveforms of triple harmonic method at 90Mhz (left) and 120Mhz (right)

With the $\ln(\frac{V_{30}}{V_{10}})$ at the track center as a reference, we calculated the effective magnetic spacing at every off-track position with formula (6.1), and the values of $\Delta(d+a)$ compared to track center are plotted in Fig. 7.5. The possible gain offset caused by different recording frequency will not lead to error since the harmonic ratio

is considered here. It is interesting to notice that the $\Delta(d+a)$ increases with the increase of off-track displacement. Since we are sure that d is a constant, this result suggests that the a value is not a constant along the cross-track position and it increases as the amount of off-track increases.

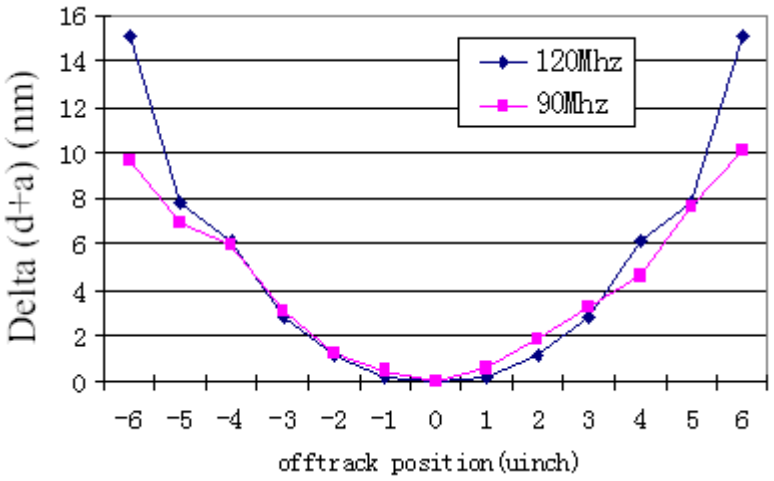

Fig. 7.5 Change in effective magnetic spacing(nm) compared to track center as a function of cross-track position

Furthermore, the two curves are almost the same until the head is at the edge of the track, and the curve corresponding to the higher recording density case increases faster at the track-edges. This suggests that the a variation in cross-track direction differs with recording density at the track-edge. As transitions are written closer at high densities, it is expected that track-edge plays an important role in transition percolation especially with narrow track widths, and the induced partial erasure yields a reduced effective track width and more serious a increase due to the magnetic poles at the track-edges [26].

To further confirm our experimental findings, we recorded isolated pulses on the media and captured the readback waveform at the track center and at different off-track positions with the oscilloscope. The waveforms are carefully aligned with the

trigger signal and multiple isolated pulses are averaged to ensure high accuracy, and these are shown in Fig.7.6. As expected, the pulse is widened and the amplitude decreases at the off-track position as a result of increase in transition length. Furthermore, as seen in Fig. 7.6, the peak positions of the pulses at off-track positions are shifted away from that of the track center. This indicates that the transition itself is not uniform in the cross-track position, with both the transition length and recorded position being variable. The above two phenomena become much more obvious at the track-edge compared to the on-track positions.

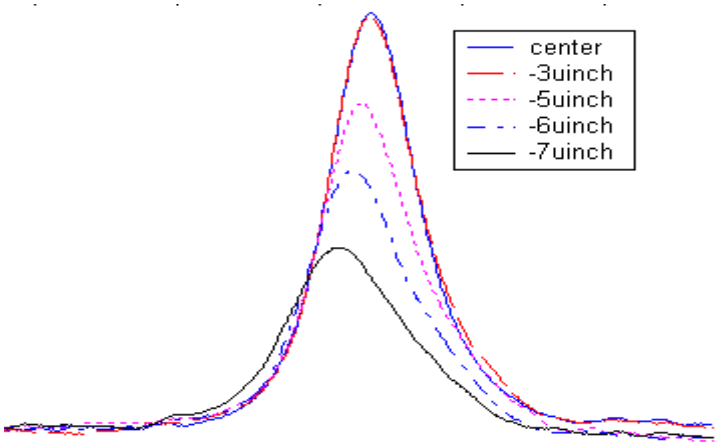

Fig. 7.6 Isolated pulse waveforms at track center and off-track positions

7.2 Theory and Simulation

7.2.1 Recording Physics Underlying the Phenomena

In previous chapters we assumed that the transitions are uniform in the cross-track direction, whereas in reality, the magnetization is not uniform across the recorded track. This affects the pulse shape versus track offset and deserves further exploration. The Williams-Comstock model assumes that the transition contour is written where the trailing head field is equal to the remnant coercivity of the medium. Fig. 7.7 shows the write filed direction and constant field magnitude contours. It is noticed that the field

direction is largely perpendicular to the contour at the right part of the figure while field has large components along the contour in the left part. The field perpendicular to the field magnitude contour results in transition charge. The charge distribution extends beyond the width of the inductive writer due to track-edge fields, so the effective track width could differ slightly from the physical width of the trailing pole. In reality, read-width is designed much smaller than the write width to avoid reading the poor signal at the track-edge.

The Magnetic Force Microscope (MFM) is the industry tool for examining the shape of the written transitions. An isolated track MFM measurement result with the constant field magnitude contour equal to the medium coercivity is illustrated in Fig. 7.8 [36]. It is clear that the transition shape is curved in cross-track direction and we define this as track-edge bending effect.

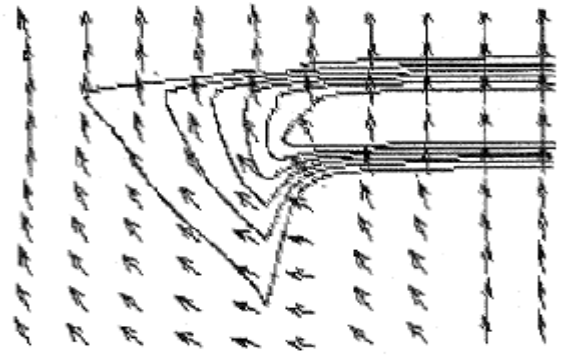

Fig. 7.7 Constant write field magnitude contours and in-plane vector field

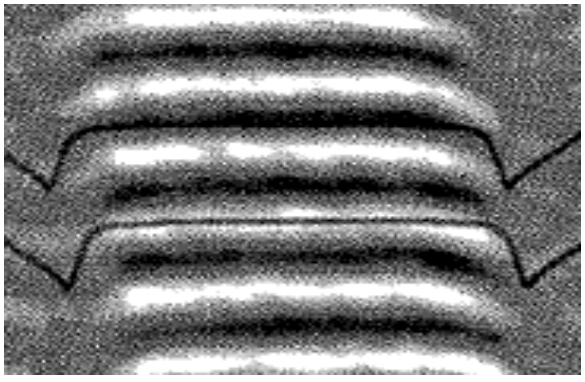

Fig. 7.8 MFM measurements of transitions and transition contour curve

Moreover, the non-uniformity of the write head field leads to non-uniform transition parameter across the track. The Williams-Comstock model assumes that the competition between the field gradient of the head and the demagnetization effects results in a transition that is perpendicular to the transition contour. At each point of the transition, a local "a" parameter characterizes the magnetization. With the non-uniform head field considered here, the "a" parameter becomes a function of cross-track position z since the actual field gradient of the in-plane field normal to the transition contour defined by $|H| = H_c$ is a function of z. Given a field model, the field gradient is used to calculate a local "a" parameter as

$$a(z) = \sqrt{\left[\frac{M_r t}{\pi}\right] \Big/ \frac{d}{dx} H(x,z)} \,. \tag{7.1}$$

The write field gradients become shallower with increasing off-track distance due to the head fields having large components along the coercivity contours as seen in Fig. 7.7. This leads to broadening of the resultant transition [37]. According to the variation of transition parameter, the track could be divided into three bands: signal band at the track center, noise band at the track-edge where the transition parameter begins to increase rapidly, and the erase band where the transition parameter becomes very large and shows AC erased state [38].

7.2.2 Simulation Model

Accurate modeling of the cross-track properties of magnetic recording requires complicated and time-consuming micro-magnetic calculation. A micro-magnetic simulator is a computer program designed to compute the local magnetization within a material. The user provides inputs such as the material geometry, the initial

magnetization, and the time evolution of the external magnetic field. It is also necessary to specify for each different material several parameters such as demagnetization, the exchange interaction field, and anisotropy.

A micro-magnetic model considering the media grain size and anisotropy field H_k distribution, and inter and intra grain exchange field is used for calculation. The 3-D Lindholm head field [39] is used as writing field to generate the magnetic transitions in the longitudinal media. A typical result of magnetization of media is illustrated in Fig. 7.9. It could be seen that the generated transitions show curved shape and transition parameter could increase rapidly at the track-edge.

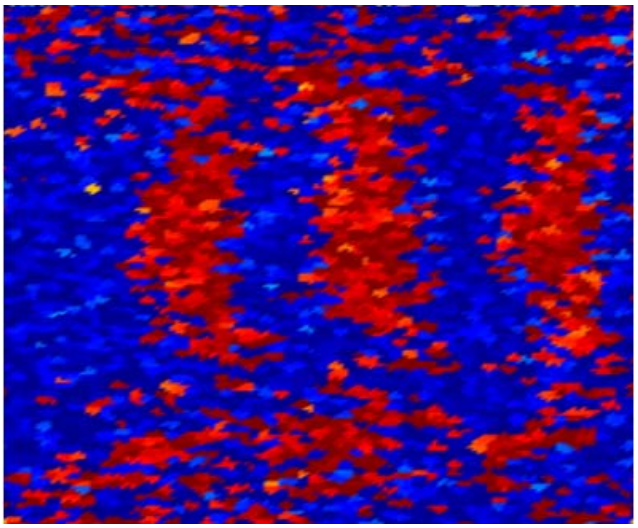

Fig. 7.9. Magnetization simulated with micro-magnetic model

Since the focus of our study in this thesis is system level, we prefer a model with less number of inputs and easy to calculate, but could describe the physical principle and property of the phenomena in experiment. The micro-track model meets our requirement here.

We modeled the above cross-track characteristics by modeling the track as being

divided into N equally sized smaller tracks called micro-tracks. When a transition is written, a magnetization flip occurs on each micro-track. Each micro-track has its own transition location and transition length. In addition, it is assumed that the response of the channel to each of the micro-track can be described by a reader response $h(a_i, x-\tau_i)$ that depends on the transition parameter a_i and the relative location of the transition center $x-\tau_i$ for each micro-track. The total response $p(x)$ is the sum of all the $h(x)$ in the cross-track direction limited by the read width.

The functional form of $h(x)$ could be obtained through the deconvolution of experimental data or can be some complicated form as described in the previous sections. But, here we approximated it by the response of a shielded MR reader to an arctangent transition shape for simplicity:

$$h(x) = CM_r\delta(\tan^{-1}\frac{x+g/2}{a+y} - \tan^{-1}\frac{x-g/2}{a+y}). \qquad (7.2)$$

Given the experimental parameters in Section 7.1.2 and the calculated transition parameter variation with experimental results in Fig. 7.5, and after referring to some previous study of the transition contour in cross-track direction [38], we plotted the assumed transition contour and transition parameter variation in the cross-track position in Fig. 7.10 which was utilized in the simulation. With this simulation model, we are able to estimate the experimental result in a fast way.

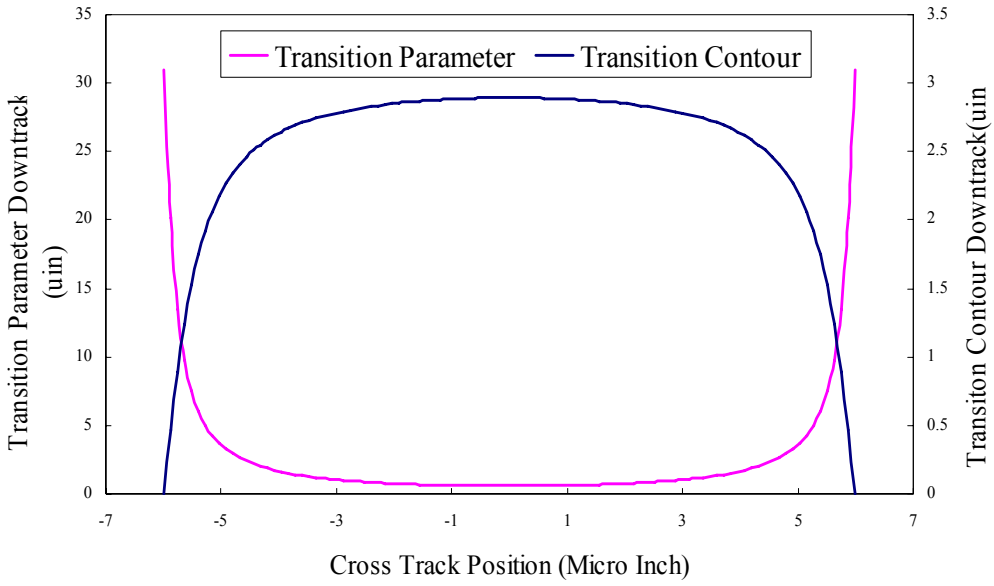

Fig. 7.10. Assumed transition contour and transition parameter variation in the cross-track direction

7.3 Summary

The transition bending effect and transition parameter variation in cross-track direction will lead to fly-height variance when the head is off-track. And study shows the above effect becomes important at track-edge.

Chapter 8

Summary and Future Work

The aggressive areal density growth in disk drives requires all the parameters in head disk systems to be scaled downwards progressively. The smaller system dimension inevitably introduces tribological and magnetic instabilities, and makes the manufacturing process more difficult to maintain the high standard of reliability and performance for the head disk system. This thesis is dedicated to the investigation of the technology useful for characterizing the critical parameters and system performance of head disk systems at high recording density.

The various fly-height testing methods are reviewed and discussed in terms of working principle, benefits and drawbacks. It is believed that the in-situ head-disk spacing measurement will play more and more important role in head-disk systems at sub-10nm level of head-disk spacing, since this method uses the available magnetoresistive (MR) read sensor as a transducer to measure the magnetic spacing directly on a real-time basis.

A simulation platform has been developed to study the readback signal based head disk system characterization methods with flexibility of theoretical model selection and parameters setup. Accurate mathematical models are used for calculation of the readback signal with MR head as a transducer and unique characteristics of MR signal have been discussed.

Sensitivity and precision are used as the two important criteria in evaluating harmonic based fly-height (*FH*) measurements methods. The factors leading to fly-height variation includes system parameter variation, noise and voltage testing resolution. Triple harmonic method has the advantage of having good accuracy and repeatability within a wide density range, *FH* calculated with the harmonic ratio of triple harmonic method at higher density could achieve higher precision than square wave harmonic method and achieve high testing sensitivity. And averaging of testing results could minimize fly-height variance.

We proposed a novel method to evaluate the gap length variation among a batch of heads at magnetic integration level, knowing the nominal gap length of the reference head and the harmonic ratio of all the testing heads. Triple harmonic pattern makes it possible to estimate gap length variation with combinations of densities that have bigger difference to achieve high gap length estimation sensitivity and accuracy.

Factors that affect triple harmonic fly-height testing method at high density and high data rate recording are studied. Firstly, the channel response limited the achievable working frequency and the testing result should be carefully compensated with the channel response especially in the high frequency region to guarantee high accuracy. Secondly, the nonlinear transition shift affects the testing result in the high-density region and the phenomena will be more evident when hard transition shift enforces NLTS and leads to bigger NLTS oscillation between individual transitions. Thirdly, the NLTS effect will be more evident in high data rate recording because of the finite rising effect of the write field. Furthermore, transition parameter is increased in the high density and high recording frequency region. Fourthly, the transition bending

effect and transition parameter variation in cross-track direction will lead to fly-height variation when the head is off-track. And study shows the above effect becomes important at track-edges.

Future work may include the following items:

a) Explore new pattern for harmonic based fly-height testing method. The current triple harmonic pattern concentrates energy on three harmonics. Because the ratio of two harmonics is used for fly-height testing, a new pattern with energy concentrated on two harmonics is preferred.
b) Study on fly-height testing method for perpendicular recording system. Perpendicular recording technology is becoming the dominant technology since it enables higher areal density than longitudinal system. Studying the feasibility of current FH method on perpendicular recording system, and exploring more suitable methods are necessary.
c) Model the track edge effect with more accurate models.

References

[1] Miura, “Hard Disk Drive Technology: Past, Present and Future”, Digest of the Asia-Pacific Magnetic Recording Conference, August 2002, Singapore, pp. AK1-01 - AK1-02.

[2] B. R. Brown, H. L. Hu, K. B. Klaassen, J. J. Lum, J. van Peppen and W. E. Weresin, “Method and Apparatus for In-Situ Measurement of Head/Recording Medium Clearance”, US Patent 4,777,544.

[3] C. Lin and R. F. Sulliran, “An Application of White Light Interferoemetry in Thin Film Measurement,” IBM Journal of Research and development, Vol. 16, No. 3, pp. 269-276, May 1972.

[4] Y. Li, “Flying Height Measurement Metrology for Ultra-Low Spacing in Rigid Magnetic Recording,” IEEE Trans. Magn., Vol. 32, No.1, pp. 129-134, Jan 1996.

[5] P. de Groot, “Optical Gap Measuring Apparatus and Method,” US patent 5,557,399.

[6] Karlqvist, “Calculation of the Magnetic Field in the Ferromagnetic Layer of A Magnetic Drum”, Trans. Roy. Inst. Technology, Vol. 86, pp 3-27, 1954.

[7] B. Liu and Z. M. Yuan, “In-Situ Characterization of Head Disk Clearance”, in Proc. Symp. Interface Tribology Towards 100 Gb/in^2 and Beyond: ASME, 2000, pp. 51-58.

[8] K. B. Klaassen and J. C. van Peppen, “Method and Circuitry for In-Situ Measurement of Transducer/Recording Media Clearance and Transducer Magnetic Stability”, US Patent 5,130,866.

[9] Z. Yuan, B. Liu, W. Zhang and S. Hu "Engineering Study of Triple-Harmonic Method for In Situ Characterization of Head-Disk Spacing," Journal of Magnetism and Magnetic materials, Vol. 239, pp. 367-370, 2002.

[10] B. Liu and Q. S. Chen, "Carrier Erasure Current Method for In-Situ Monitoring of Head Disk Spacing Variation", IEEE Trans. Magn., Vol. 35, No. 2, pp. 939~944, 1999.

[11] Hegde and Suryanarayan G, "Capacitive Measurement and Control of the Fly Height of A Recording Slider", US Patent 4,931,887.

[12] R. L. Comstock and M. L. Williams, "An Analytical Model of the Write Process in Digital Magnetic Recording," in Proc.17th Annu. AIP Conf., May 1971, pp. 738–742.

[13] X. Xing and H. N. Bertram, "Analysis of Transition Noise in Thin Film Media", IEEE Trans. Magn., Vol. 33, No. 5, pp. 2959-2961, Sept. 1997.

[14] Fung. T, B. K. Middleton, J. J. Miles and M. Aziz, " Transition Shape and Nonlinear Effects in Digital Magnetic Recording on Thin Film Media", J. Appl. Phys., Vol. 30, pp. 1483-1488, May 1997.

[15] N. Smith, "Reciprocity Principles for Magnetoresistive Heads", IEEE Trans. Magn., Vol. 31, No. 6, Nov. 1995

[16] H. N. Bertram, "Linear Signal Analysis of Shielded AMR and Spin Valve Heads", IEEE Trans. Magn., Vol. 31, No. 6, Nov. 1995

[17] H. N. Bertram, Theory of Magnetic Recording, pp. 59-63, Cambridge University Press, 1994.

[18] R. I. Potter, "Digital Magnetic Recording Theory," IEEE Trans. Magn., Vol. 10, no. 3, pp. 502–508, Sept. 1974.

[19] E. J. Champion and H. N. Bertram, "The Effect of MR Head Geometry on Playback Pulse Shape and Spectra," IEEE Trans. Magn., Vol. 31, no. 4, pp. 2461–2470, July 1995.

[20] H. A. Shute, D. T. Wilton, and D. J. Mapps, "A Theoretical Analysis of Shielded Magnetoresistive Heads by Conformal Mapping," IEEE Trans. Magn., Vol. 33, pp. 809–819, Jan. 1997.

[21] Y. Zhang, S. Shtrikman and H. N. Bertram, "Playback Pulse Shape and Spectra for Shielded MR Heads", IEEE Trans. Magn., Vol. 33, No. 2, March 1999.

[22] Aziz, "Signal and Noise Properties of Longitudinal Thin-Film Disk Media" Ph.D. dissertation, University of Manchester, 1999.

[23] Taratorin, "Characterization of Magnetic Recording Systems", Guzik Technical Enterprises, 1996.

[24] D. E. Helm, "Design and Operation of Spin Valve Sensors" IEEE Trans. Magn., Vol . 30, No .2, March 1994.

[25] H. W. Wong-Lam, "A Simple Transition Response Model for Magnetoresistive Heads on Thin-Film Media", IEEE Trans. Magn., Vol . 33, No .1, March 1997.

[26] J. G. Zhu, T. Lam, Y. Luo and X. G. Ye, "Nonlinear Partial Erasure and Its Correlation with Transition Noise in Longitudinal Thin Film Media", J. Appl. Phys., Vol. 79, pp. 4906, 1996.

[27] Y. S. Tang and C. Tsang, "Nonlinear Transition Shifts in Magnetic Recording Due to Interpattern Proximity Effects", J. Appl. Phys., Vol. 75, No. 5, pp. 3546-3550, Sept. 1993.

[28] A. Taratorin, J. Fitzpatrick, S. X. Wang, and B. Wilson, "Non-Linear Interactions in A Series of Transitions", IEEE Trans. Magn., Vo1.33, No. 1, January 1997, pp. 956-6 1.

[29] A. Taratorin, D. Cheng, P. Arnett and R. Olson, “Intra-and Inter-pattern Nonlinearity in High Density Magnetic Recording”, IEEE Trans. Magn., Vo1. 34, No. 1, January 1998.

[30] Y. S. Tang and C. Tsang, “A Technique for Measuring Nonlinear Bit Shift”, IEEE Trans. Magn., Vol. 27, No. 6, pp. 5316-5318, Nov. 1991.

[31] B. Wilson and S. X. Wang, “A Generalized Method for Measuring Readback Nonlinearity Using A Spinstand”, MMM 2006.

[32] P. Thayamballi, “Modeling the Effects of Write Field Rise Time on the Recording Properties in Thin Film Media”, IEEE Trans. Magn., Vol. 32, pp.61-66, 1996.

[33] R. Wood, M. Williams and J. Hong, “ Consideration for High Data Rate Recording with Thin Film Heads”, IEEE Trans. Magn., Vol. 26, pp. 2954-2959, 1990.

[34] X. Xing and H. N. Bertram, “Analysis of the Effect of Write Head Field Rise Time on Signal, Noise, and Nonlinear Transition Shift”, J. Appl. Phys., Vol. 85, No. 8, April 1999.

[35] S. X. Wang and A. Taratorin, “Magnetic Information Storage Technology”.

[36] M. Madison, T. Arnoldussen, T. Chang, R. Wood, and F. Scott II, “Erase Band and Transition Charge Model and MFM,” IEEE Trans. Magn., Vol. 32, No. 5, pp. 3878–3880, Sept. 1996.

[37] T. C. Amoldussen, “ Side Writing/reading in Magnetic Recording”, J. Appl. Phys., Vol. 69, pp 4718-4720, April 1991.

[38] E. Champion, ”Studies of Track Edge Noise Using A 3-D Micro Track Model”, IEEE Trans. Magn., Vol. 36, No 1, Jan. 2000.

[39] D. A. Lindholm, “Magnetic Fields of Finite Track Width Heads”, IEEE Trans. Magn., Vol. 13, pp. 1460-1462, Sept. 1977